“Study of PEDOT:PSS/a-Si:H heterojunction for charge collection in hybrid thin film solar cells”

by

M.Sc. Antonio de Jesús Olivares Vargas

A thesis submitted in partial fulfillment of the requirements for the degree of

Ph. D. in Optics

at

National Institute for Astrophysics, Optics, and Electronics
February 2020
Tonantzintla, Puebla

Advisors:

Dr. Ismael Cosme Bolaños
CONACyT-INAOE

and

Dr. Svetlana Mansurova
CONACyT-INAOE

Acknowledgments

This work would not have been possible without the funding provided by the SENER-CONACyT project No. 152244. And, I acknowledge Consejo Nacional de Ciencia y Tecnología (CONACyT) for the scholarship No. 421632.

I would like to express my sincere gratitude to my advisors Dr. Ismael Cosme Bolaños and Dr. Svetlana Mansurova for the continuous support during my Ph.D. studies, for their patience, motivation, and for sharing their immense knowledge.

Besides my advisors, I would like to thank thesis committee: Dr. Rubén Ramos García, Dr. Mario Moreno Moreno, Dr. Carlos Zúñiga Islas, Dr. Canek Fuentes Hernández and Dr. Hiram Enrique Martínez Mateo, for their insightful comments and encouragement.

I thank the laboratory technical: Adrian Itzmoyotl, for being a mentor in the technical aspects of this research and a friend for me. Also, I thank the laboratory technical: Victor Aca, Armando Hernandez, Juan Álvarez, Ignacio Juarez, Rebeca Lugo, Leticia Tecuapetla and Netzahualcoyotl Carlos.

Last but not the least, I would like to thank my family and friends for supporting me spiritually throughout life and my Ph.D. studies.

Abstract

Silicon/Organic Heterojunctions (SOH) are an alternative to inorganic heterojunctions due to the use of organic materials which present solution-type processing that allows deposition at room temperature and atmospheric pressure. Recently, organic materials have demonstrated to be suitable to replace the common n-type and p-type inorganic materials to simplify the formation of p-i-n-junctions in solar cells. Some preliminary attempts to use organic materials in hybrid n-i and i-p heterojunctions with a-Si:H have been reported in the literature. However, performance characteristics are limited ($J_{sc} < 4$ mA/cm^2) by the characteristics of the polymers and their poor optimization for the use in a hybrid heterojunction interface with a-Si:H.

In this work, we use the poly(3,4-ethylenedioxythiophene)-poly(styrenesulfonate) (PEDOT:PSS) material to form a hybrid heterojunction with a-Si:H for high charge carrier collection at the frontal interface of solar cells. The deposition of a-Si:H films by PECVD at low temperatures and at the low-pressure regime was explored to study the compatibility with organic materials. On the other hand, different post-treatment techniques were proposed to enhance the electrical and morphological properties of PEDOT:PSS films to control and improve their characteristics. These results were used to form a hybrid heterojunction as a frontal interface in hybrid solar cells.

The best performance characteristics (J_{sc}= 17.8 mA/cm^2, V_{oc}= 840 mV, FF= 50.4 % and PCE= 7.5 %) were obtained using a PEDOT:PSS/buffer/a-Si:H heterojunction in the hybrid structure fabricated with a PEDOT:PSS layer treated with the dip technique. This heterojunction demonstrated high transmittance, reduction of electron diffusion, and enhancement of the internal electric field. Although the structure was a planar superstrate-type configuration and the PEDOT:PSS layer was exposed to a glow discharge, the hybrid solar cell reached high efficiency compared to that in similar hybrid solar cells with substrate-type configuration and that in textured well-optimized amorphous silicon solar cells fabricated at low temperature. Thus, we demonstrate that PEDOT:PSS is fully tailored and compatible material with plasma processes and can be a substitute for inorganic p-type layers in inorganic solar cells and related devices with an improvement of performance and simplification of the fabrication process.

Resumen

Las heterouniones silicio/orgánico (SOH) son una alternativa a las heterouniones inorgánicas, debido al uso de materiales orgánicos que presentan un procesamiento de tipo solución que permite su depósito a temperatura ambiente y presión atmosférica. Recientemente, los materiales orgánicos han demostrado ser adecuados para reemplazar los materiales inorgánicos comunes tipo n y tipo p para simplificar la formación de uniones p-i-n en celdas solares. En literatura se han reportado algunos resultados preliminares al usar materiales orgánicos en heterouniones híbridas n-i e i-p con silicio amorfo. Sin embargo, las características de rendimiento están limitadas (Jsc < 4 mA/cm2) por las características de los polímeros y su pobre optimización para el uso en una interfaz de heterounión híbrida con silicio amorfo.

En este trabajo, utilizamos el material poli(3,4-etilendioxitiofeno)-poli(estirenosulfonato) (PEDOT:PSS) para formar una heterounión híbrida con a-Si:H para la colección de portadores de carga en la interfaz frontal de celdas solares. El depósito de películas de a-Si:H por PECVD, a bajas temperaturas y en el régimen de baja presión, se exploró para estudiar la compatibilidad con materiales orgánicos. Por otro lado, se propusieron diferentes técnicas de tratamiento para mejorar las propiedades eléctricas y morfológicas de las películas de PEDOT:PSS. Estos resultados se usaron para formar una heterounión híbrida como interfaz frontal en celdas solares híbridas.

Las mejores características de rendimiento (Jsc= 17.8 mA/cm2, Voc= 840 mV, FF= 50.4 % y PCE= 7.5 %) se obtuvieron usando una heterounión PEDOT:PSS/buffer/a-Si:H en una estructura híbrida fabricada con una película de PEDOT:PSS tratada con la técnica de inmersión en IPA. Esta heterounión demostró una alta transmitancia, reducción de la difusión de electrones y mejora del campo eléctrico interno. Aunque la estructura era una configuración de tipo p-i-n y la película de PEDOT:PSS estuvo expuesta a un plasma, la celda solar híbrida alcanzó una alta eficiencia en comparación con las celdas solares híbridas similares con configuración del mismo tipo y las celdas solares de silicio amorfo fabricadas a baja temperatura, texturizadas y optimizadas. Por lo tanto, demostramos que PEDOT:PSS es un material totalmente compatible con los procesos de plasma y puede ser un sustituto de las capas inorgánicas de tipo p en celdas solares inorgánicas y dispositivos relacionados con la mejora del rendimiento y la simplificación del proceso de fabricación.

INDEX

CHAPTER I

1. INTRODUCTION

1.1 RENEWABLE ENERGY

Nowadays, the offer and demand of the energy sector determine the economic growth of a country, due to the close relationship that exists with the domestic product. The scarcity of natural resources in some cases has forced to look for new alternatives to obtain more energy at a lower production cost. In this context, the use of renewable energies increases the energy stability of a country, as it helps to reduce the dependence of price volatility on conventional energy sources.

The greatest growth in the use of renewable energy has occurred in the electricity sector, compared to the heating, cooling, and transportation sectors. It is estimated that in 2018, around 181 GW of renewable power capacity was added. Overall, renewable energy now accounts for around one-third of the total installed power generation capacity worldwide. Nearly two-thirds (64 %) of net installations in 2018 were from renewable sources of energy, marking the fourth consecutive year that net additions of renewable power were above 50 % (see figure 1.1). The total capacity of electricity through renewable energy grew by 8 % and the total capacity of renewable energy reached approximately 2,378 GW at the end of 2018 [1]. With 181 GW, solar energy was preferred worldwide and the number of countries that use renewable energy is increasing. The addition of photovoltaic energy accounted for 55 % of the new renewable energy capacity, followed by wind power (28 %) and hydroelectric power (11 %).

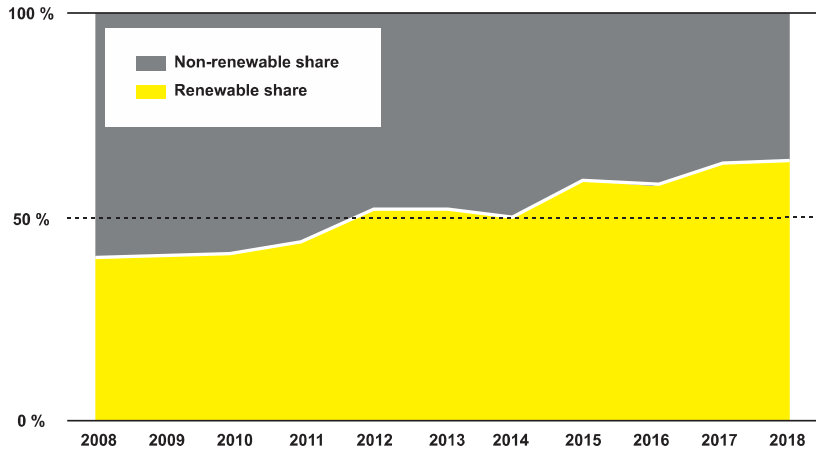

Figure 1.1. Share of Renewables in Net Annual Additions of Power Generating Capacity, 2008-2018 [1].

Thus, research and technological development in the energy sector, specifically photovoltaic technology, is an alternative to try to help solve global energy problems.

1.2 BACKGROUND AND JUSTIFICATION

Solar cells or photovoltaic cells are devices that change the solar energy to electrical energy using the photovoltaic effect. When the light reaches a solar cell, a fraction of it is reflected by the surface and the remaining light is transmitted into the solar cell. The light transmitted into the solar cell is absorbed by a semiconductor material, generating electron-hole pairs. These pairs of holes and electrons are separated by an electric field generated by n-type and p-type semiconductor materials and are collected by metal electrodes.

Currently, 85 % of the solar energy market uses silicon technology (inorganic semiconductor) to manufacture solar cells with conversion efficiencies of approximately 27.6 % [2]. High purity silicon is used due to the excellent charge transport properties and high stability in the environment. However, high costs, high temperature fabrication methods and limited fabrication areas are some of the disadvantages of this technology. There are solar cells based on thin films (hundreds of nanometers) of semiconductor materials that can be fabricated on flexible and cheap substrates. On the other hand, in the last decade with the advance of materials engineering, new materials have emerged, among them are organic semiconductors. Solar cells based on organic semiconductors have important advantages such as flexibility, fabrication in large areas, deposition at room temperature and atmospheric pressure. However, even with the mentioned advantages, these solar cells only have efficiencies of up to 14 % [2].

In recent years, a research field emerged as an alternative to organic solar cells, hybrid solar cells. These devices are formed by heterojunctions of organic and inorganic semiconductors for the fabrication of optoelectronic devices. These devices present advantages as excellent electronic and charge transport properties (inorganic semiconductors properties) and easer fabrication processes (organic semiconductors properties) [3, 4]. Therefore, the study and optimization of this type of structure are important because they have the potential to obtain high efficiency photovoltaic devices at low cost.

At the National Institute for Astrophysics, Optics, and Electronics (INAOE) this type of structure has been studied. Hybrid photovoltaic structures with p-i-n configuration and based on a-Si:H, poly(3-hexythiophene):phenyl-C61-butyric acid methyl ester (P3HT:PCBM) and, poly(3,4-ethylenedioxythiophene):poly(4-styrenesulfonate) (PEDOT:PSS) films have been fabricated (see figure 1.2) [5].

Where the ITO/PEDOT:PSS/(i)a-Si:H/(n)a-Si:H/Ti (H2) structure presented a remarkably high short circuit current density (J_{sc}) as large as 17.74 mA/cm^2, an open circuit voltage (V_{oc}) of 640 mV and, a power conversion efficiency (PCE) of 3.75 %. Demonstrating the compatibility of PECVD processes and

organic materials technology. However, these results also showed current suppression, which led to a low fill factor (FF) and, a relatively low V_{oc}, a high series resistance (R_s) and, a low shunt resistance (R_{sh}).

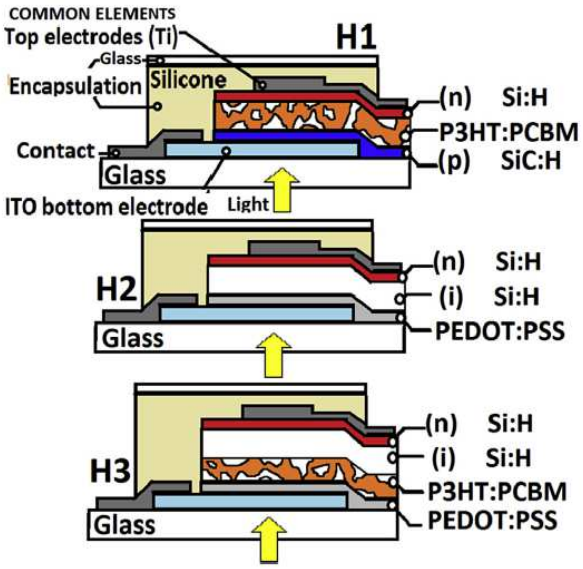

Figure 1.2. Hybrid photovoltaic structures based on a-Si:H, P3HT:PCBM and, PEDOT:PSS films previously fabricated at INAOE.

Therefore, the p-i and n-i interfaces must be optimized for two main reasons: 1) Because the electric field formed by both semiconductors p-type and n-type must be uniformly distributed through the intrinsic semiconductor and avoid the electron-hole recombination in this region and 2) Because the free charge carriers must be easily transported to the conductive electrodes and avoid the electron-hole recombination at the p-i and n-i interfaces, or at the metal electrodes.

The passivation of non-metallic areas with dielectric layers such as SiO_2, SiN_x or Al_2O_3 has been proposed to avoid the recombination at these areas [6]. With the emergence of new structures, the use of “Buffer” layers to fabricate solar cells has increased because they help to couple interfaces between different materials in semiconductor devices. On the other hand, doped films must have a good conductivity to facilitate charge carrier transport to the metal electrodes and they can also be easily modified on a nanometric scale to modify the contact resistance.

1.3 OBJECTIVE

The objective of this work is to investigate the formation of a-Si:H/Organic heterojunction with emphasis in studying the a-Si:H layer deposition by PECVD process and the electrical properties of the organic layer to enhance charge collection in the frontal interface of a-Si:H-based photovoltaic devices.

1.4 THESIS ORGANIZATION

This thesis is generally organized as follows:

- In chapter 2, the analysis of the literature of a-Si:H, organic semiconductors, PEDOT:PSS properties, PEDOT:PSS secondary doping and, hybrid photovoltaic devices are presented.
- In chapter 3, the methodology for the fabrication and characterization of both films and devices is presented. Also, the variations to the fabrication process proposed are presented.
- In chapter 4, the results of the characterization of a-Si:H films deposited by PECVD at different deposition pressures and PEDOT:PSS films are shown. Also, the results of the hybrid photovoltaic devices characterization are presented.
- In chapter 5, the results are discussed and compared between them and with data available in the literature.
- Finally, in chapter 6, the general conclusions are shown.

CHAPTER II

2. ANALYSIS OF LITERATURE

Hybrid photovoltaic devices are made from organic and inorganic materials. Taking advantage of excellent electrical properties of inorganic materials and the simple processing of organic materials, the hybrid solar cells present a large potential to create the next generation of solar cells with low cost and high efficiency. In this chapter, first the main dependence of the electronic properties of a-Si:H films according to the temperatures and pressure deposition is described. Next, a brief introduction to the physics of organic semiconductor is mentioned, focusing on the physical and electrical properties of PEDOT:PSS. Following with a literature review of the techniques, methods, and materials used to modify the properties of the different types of PEDOT:PSS. Since a huge amount of methods and materials have been published to modify the properties of PEDOT:PSS, only the most important ones are mentioned. And finally, in the last section, the state of art of the hybrid organic-inorganic solar cells with a summary of the most important results published are presented.

2.1 AMORPHOUS SILICON

In 1965, H. F. Sterling et al. [7] investigated for the first time the chemical vapor deposition promoted by a radio-frequency (r.f.) discharge to make films of silicon from silane. In this method, the chemical reactions take place in an r.f. discharge instead of being promoted thermally. R. C. Chittick et al. [8] used an r.f. glow discharge to deposit amorphous silicon (a-Si) films from silane gas on to substrates at 25 – 650 °C, obtaining amorphous silicon films with resistivities at 21 °C of up to 10^{14} Ω·cm.

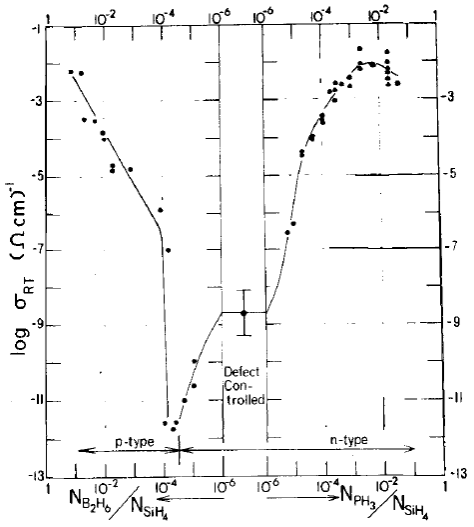

Figure 2.1. Conductivities at room temperature of p-type and n-type a-Si specimens plotted as a function of the PH_3 or B_2H_6 concentration [9].

Shortly after, P. G. Le Comber and W. E. Spear [9] reported that substitutional doping of amorphous silicon (a-Si) and amorphous germanium (a-Ge) is possible adding some phosphine (PH_3) or diborane (B_2H_6) gas to the r.f. glow discharge gas mixture. They demonstrated that both p-type and n-type a-Si can be prepared with conductivities (at room temperature) varying over some ten orders of magnitude (see figure 2.1).

As it can be observed, amorphous silicon doped films are formed from a source gas as an alloy of silicon and hydrogen. In fact, it was not recognized immediately that hydrogen plays an important role in doping the amorphous silicon films. Amorphous silicon films for electronic applications is called hydrogenated amorphous silicon (a-Si:H).

2.1.1 HYDROGENATED AMORPHOUS SILICON

The successful deposition and doping of amorphous silicon films by the PECVD technique created interest in the use of these films in diverse applications for two main reasons. First, for its excellent electric and optoelectronic properties, for example, the high absorption coefficient of a-Si:H in the visible range of the solar spectrum, a 1 µm thick a-Si:H layer is enough to absorb 90 % of the usable solar energy [10]. And second, the a-Si:H deposition by the PECVD technique, allow amorphous silicon films deposition over a large area (larger than 1 m^2) and over low cost substrates of almost any shape or composition (such as glass or flexible substrates or polymers) due to the low processing temperature (from 100 to 400 °C).

To understand the operation a-Si:H-based device structure and some related phenomena that will be discussed later, Briefly the structural and material properties of a-Si:H will be described and will be comparing them to those of single crystal silicon. Figure 2.2 shows the single crystal silicon and a-Si:H atomic structures.

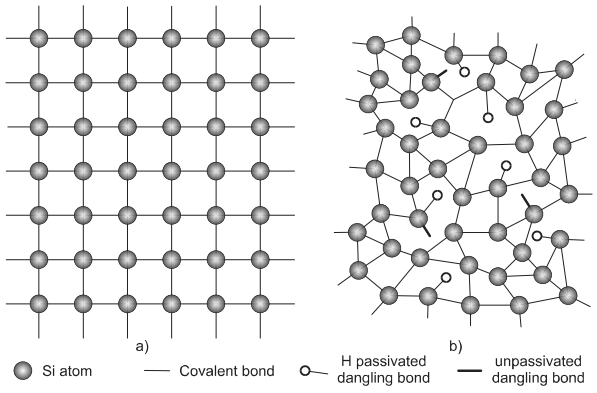

Figure 2.2. Representation of the atomic structure of a) single crystal silicon and b) hydrogenated amorphous silicon.

A silicon atom has four valence electrons, so in a crystalline silicon structure (see figure 2.2-a), each silicon atom is bonded to four neighbor silicon atoms by covalent bonds. All bonds have the same length, and the angles between the bonds are equal. This translates into a perfectly periodical system with long scale order. Figure 2.2-b shows the a-Si:H structure. It can be observed that most silicon atoms of a-Si:H structure also are bonded to four neighbor silicon atoms by covalent bonds, but bond length and angles vary. As a result, the order over the short range is preserved, but over a long range [11] it is not preserved. The larger difference in the bonding angles and the bonding lengths between the neighboring silicon atoms in a-Si:H result in weak or strained bonds. These bonds can break by applying enough energy (for example in the form of heat). This process leads to the formation of defects in the atomic network. In a-Si:H defects are mainly silicon atoms that are covalently bonded to only three silicon atoms and have one unpaired electron, called a dangling bond.

In the a-Si atomic structure (amorphous silicon that contains no other atoms than silicon) there is a concentration of about 10^{21} defects per cm^3. Material with these features cannot be used for electronic applications. Nevertheless, when the a-Si is deposited in such a way that hydrogen can be incorporated in the atomic network (for example by a silane gas source), the hydrogen atoms bond with most of the silicon dangling bonds leading to the formation of a strong silicon-hydrogen bond. Hydrogen passivation of dangling bonds reduces the defect density to 10^{15} - 10^{16} per cm^3. Which makes a-Si:H suitable for electronics applications.

For an ideal intrinsic silicon crystal, the conduction and valence bands are separated forming a well-defined bandgap (E_g). However, in a-Si:H energy states exist inside the bandgap due to the long-range disorder in the atomic structure and associated defects. These states are called band tails. This means that there a continuous distribution of density of states in the a-Si:H structure and there is not a well-defined bandgap.

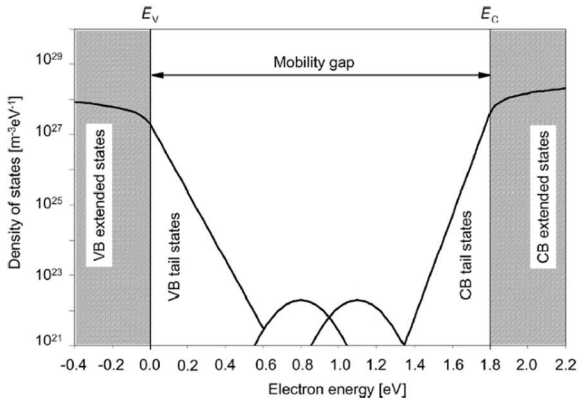

Figure 2.3. The standard model for the density of states in the a-Si:H structure [10].

The energy states in which charge carriers can be considered free carriers are described by nonlocalized wave functions and are called extended states. The disorder in the a-Si:H structure causes the wave functions of the tail and defect states to become localized in the atomic network. These states are called localized states. Whereby the charge carrier mobility in the localized states is reduced or the carrier becomes trapped. To define the bandgap in the a-Si:H structure the energy levels between the extended the states are used, and it is denoted the mobility gap. The mobility gap in the a-Si:H structure is larger than the bandgap of single crystal silicon and it is typically 1.7 – 1.8 eV.

In figure 2.3, a standard model of the state density distribution is presented. Where the valence and conduction band states are represented with gray regions and the defect states are represented by two equal Gaussian distributions. The continuous distribution of the localized states is a superposition of the valence and conduction band tail states and the defect states.

2.1.2 ELECTRICAL PROPERTIES

The electrical properties of a-Si:H films are usually characterized in terms of mobility lifetime product, dark conductivity (σ_d) and AM1.5 conductivity (σ_l) ("AM1.5", corresponds to a solar zenith angle of 48.2. While the summertime AM number for mid-latitudes during the middle parts of the day is less than 1.5, higher figures apply in the morning and evening and at other times of the year. Therefore, AM1.5 is useful to represent the overall yearly average for mid-latitudes). Measuring these properties, information about the quality of a-Si:H material for applications in solar cells can be obtained. For this work, we will focus mainly on the dark conductivity and photoconductivity properties because they are both important and easy to measure.

Typically, the σ_d of device quality intrinsic a-Si without hydrogen passivation should be lower than 10^{-10} S/cm. When the dangling bonds are passivated by hydrogen, the σ_d is reduced up to 10^{-10} – 10^{-11} S/cm. Low values of σ_d of a-Si:H undoped result in low mobility of charge carriers and a high mobility gap of a-Si:H. Intrinsic a-Si:H is characterized by electron mobility values of 10 to 20 $cm^2\ V^{-1}\ s^{-1}$, and the hole mobility is 1 to 5 $cm^2\ V^{-1}\ s^{-1}$. To measure the σ_d, an a-Si:H film is deposited on a glass substrate with two parallel conductive electrodes whereby a voltage is applied, and a current is measured. The dark conductivity is determined as:

$$\sigma_d = \frac{I}{V}\frac{w}{L\,t} \qquad \text{Eq. 2.1}$$

Where V is the voltage applied, I is the current measured, L is the length of the electrodes (typically about 1 to 2 cm), w is the distance between the electrodes (typically about 0.5 to 1 mm) and t is the thickness of the film. The σ_l is determined in the same way that σ_d illuminating the sample with an AM1.5

light spectrum with an incident power of 100 mW/cm^2. The σ_l of device quality intrinsic a-Si:H film should be in the range of 10^{-5} - 10^{-4} S/cm [12].

Property	a-Si:H
Dark conductivity [Ω^{-1} cm^{-1}]	$<5 \times 10^{-10}$
AM1.5 conductivity [Ω^{-1} cm^{-1}]	$>1 \times 10^{-5}$
Urbach energy [meV]	<47
Activation energy [eV]	≈ 0.8
Bandgap, Tauc [eV]	<1.8
Bandgap, cubic [eV]	<1.6
Absorption coefficient (600 nm) [cm^{-1}]	$\geq 3.5 \times 10^4$
Absorption coefficient (400 nm) [cm^{-1}]	$\geq 5 \times 10^5$
Density of defect states	
(CPM, DBP) methods [cm^{-3}]	$\leq 1 \times 10^{16}$
ESR method [cm^{-3}]	$\leq 8 \times 10^{15}$
Mobility-lifetime product (600 nm) [cm^2/V]	$\geq 1 \times 10^{-7}$
H content [at. %]	9–11
Microstructure parameter	<0.1
Ge content [at. %]	

Table 2.1. Typical characteristics of device quality intrinsic a-Si:H [10].

The ratio of the AM1.5 conductivity and dark conductivity is called the photoresponse (σ_l/σ_d). This parameter gives an indication of the suitability of a material for use as a photoactive layer in a solar cell. A good photoresponse value for a-Si:H should be higher than 10^5. In table 2.1, the typical (at room temperature) characteristics of device quality intrinsic a-Si:H film are shown [10].

2.1.3 DEPOSITION PROCESS

The most used method to produce device-quality a-Si:H films is by a plasma enhanced chemical vapor deposition (PECVD). The PECVD technique consists of a plasma that provides a source of energy to dissociate silicon gas (which is usually silane) through electron impact excitation, generating various neutral radicals and molecules, positive and negatives ions, and electrons. The reactions between plasma and ions and radicals result in the formation of reactive species and large silicon-hydrogen clusters (described in the literature as dust and powder particles). While neutral species are diffused to the substrate, positive ions bombard the growing film, and negative ions are trapped within the plasma. This plasma is carried out within a stainless-steel high vacuum reaction chamber with capacitively-coupled parallel electrodes and an r.f. power feedthrough (which generates the plasma), substrates holder, substrates heating assembly and a gas handling system. In figure 2.4, a schematic diagram of a PECVD deposition system is shown.

It should be kept in mind that the deposition process in a PECVD is a complex phenomenon of gas and surface reactions that are controlled by deposition parameters as the gas composition, flows and pressure, power density, and frequency, the substrates temperature, the geometry of the electrode, etc.

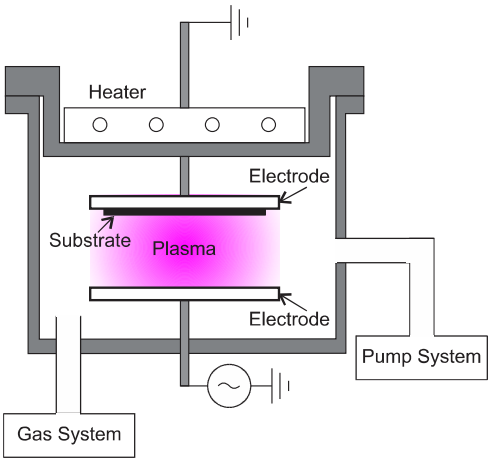

Figure 2.4. Schematic diagram of a PECVD deposition system.

J. Poortmans and V. Arkhipov [10] mentioned that to obtain uniform films of a-Si:H in a PECVD deposition system generally the deposition parameters are: a silane flow of 20 - 50 sccm, a process pressure of 0.5 - 0.7 mbar, a substrate temperature of 200 – 250 °C, an r.f. power density of 20 - 50 mW/cm^2, and an electrode distance of 1 – 3 cm. However, different parameters have been reported in the literature in order to obtained a-Si:H films of device quality.

During the a-Si:H film deposition, the substrate temperature affects the hydrogen elimination and the reconstruction of atoms after the deposition precursors. In the literature the deposition temperature for glow discharge deposition of a-Si:H films is between 200 and 300 °C. The total hydrogen content decrease when the substrate temperature is increased but the dispersed hydrogen content increases [13-14]. F. K. Bhat [15] showed that the deposition rate decreased by -10 % when increased deposition temperature from 150 to 300 °C and the dark conductivity and photoconductivity increased when the deposition temperature is increased. Ueda et al. [16], Nishikawa et al. [17], and Knights et al. [18] described a decrease in the photoresponse when the substrate temperature is increased.

The effect of gas pressure in the deposition rate of a-Si:H films is lineal. In the low-pressure regime, the supply of SiH_3 radicals to reach the film's growing surface and the ion bombardment of the film's growing surface is more severe. For the high-quality film, the high pressure is favored. For pure silane, the gas pressure of the r.f. glow discharge deposition usually is kept below 1 mTorr. Although, the pressure should be below the level that causes gas-phase polymerization, which results in the accumulation of

the powder inside the glow discharge reactor [19]. However, F. K. Bhat [15] reported that an increase in the deposition rate with increasing deposition pressure leads to increase deposition and achieves a maximum, then the deposition rate starts a decrease. On the other hand, Hudgens et al. [20] reported the dark conductivity and the photoconductivity decreased when the gas pressure is increased. However, Ohnishi et al. [21] found a dependence constant between the dark conductivity and the gas pressure deposition and, a small decrease of the photoconductivity when the gas pressure is increased and a small decrease in the photoresponse although is kept in the same magnitude order when the gas pressure is increased.

2.2 ORGANIC SEMICONDUCTORS

An organic semiconductor is a carbon-based material with semiconductor properties. All organic materials are formed mostly of carbon atoms linked by single, double and triple bonds. When the material is formed by many monomers with alternating single and double bonds, the compound is called a conjugated polymer (figure 2.5). The conjugated polymers group is organic semiconductors. In these types of materials, the electronic orbitals of each atom superimpose and form molecular orbitals. The conjugation of the single and double bonds establishes a delocalization so called electrons on z-orbitals located above and under the molecule plane. Thus, two main molecular orbitals (see figure 2.5) of interest are: 1) The Highest Occupied Molecular Orbital (HOMO), which is the molecular orbital of lower energy and is fully filled with non-excited electrons (called π electrons) at 0 K, and, 2) The Lowest Unoccupied Molecular Orbital (LUMO), which is the molecular orbital of greater energy and it is completely empty at 0 K (in this orbital it will be where the excited electrons will jump and they are called π* electrons). The π electrons, which are weakly linked, form a cloud of quasi-free delocalized electrons and they are responsible for the optical and electronic transitions in organic semiconductors. The difference in energy between the HOMO and LUMO orbitals is the so-called HOMO-LUMO bandgap.

However, intermolecular interactions on organic semiconductors are weak and do not lead to extended molecular orbital delocalization. In contrast to inorganic semiconductors, transport states are not generally delocalized.

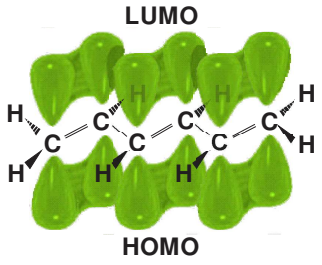

Figure 2.5. Schematic representation of the molecular orbitals in organic semiconductors.

The organic semiconductors were discovered for H. Shirakawa et al. in 1977. They found that when "Polyacetylene" films are exposed to chlorine, bromine, or iodine vapor, the conductivity increases over seven orders of magnitude [22]. As the inorganic semiconductors, organic semiconductors also can be doped, that is, obtaining organic semiconductors with electrons (n-type doping) or holes (p-type doping) excess. In inorganic semiconductors, doping is usually done by doping atoms addition in the semiconductor. The doping for organic semiconductors is frequently done by the technique proposed for H. Shikara et al. [22], exposing the organic semiconductor to the vapor passage of an oxidant or a reducer, which adding molecular dopants that facilitate electron transfer reaction to a from the semiconductor.

The chemical and physical properties of semiconducting polymers are now better understood after rigorous research over the past few years. The most studied semiconducting polymers are listed in figure 2.6, featuring the chemical structure of polyacetylene (PA), polyparaphenyle (PPP), polyparaphenyle vinylene (PPV), polypyrrole (PPy), poly(2,5 dialkoxy)parapheylene vinylene (ME-PPV), polythiophene (PT), poly(3-alkyl)thiophene (P3AT), poly (ethylenedioxythiophene) (PEDOT), and polyaniline (PANI) [24].

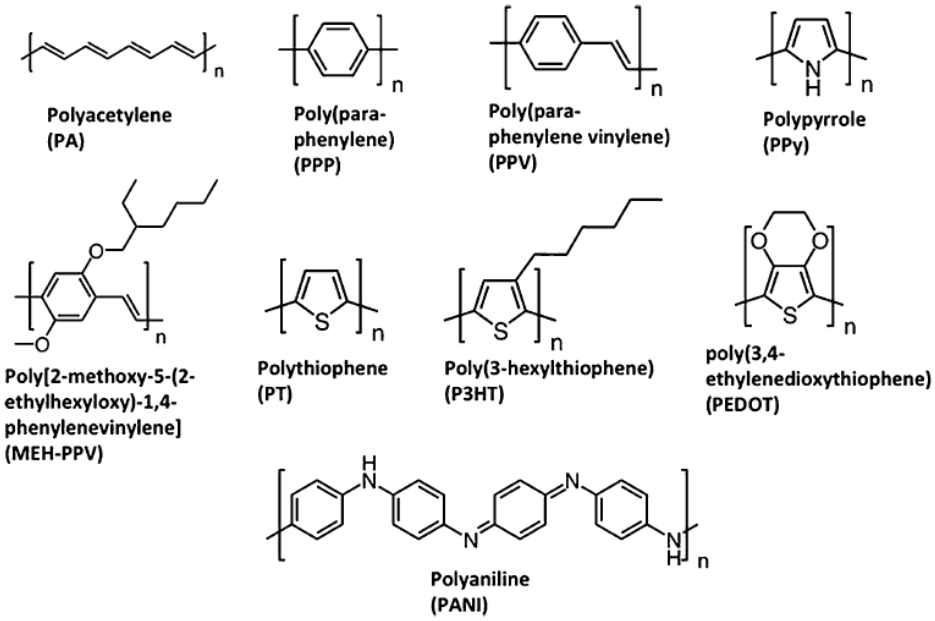

Figure 2.6. Chemical structures of some semiconducting polymers.

Their unique aspects of combining the properties of the semiconductor with their mechanical flexibility and solution processability has enabled an extensive field of research as the flexible supercapacitors, organic field-effect transistors (OFET), organic light emitting diodes (OLED), organic photovoltaic devices (OPV), as a substitute for p-type or n-type film in hybrid photovoltaic devices (HPV) [25].

2.2.1 CONDUCTIVE PEDOT:PSS POLYMER

Poly(3,4-ethylenedioxythiophene):poly(styrenesulfonic acid) (PEDOT:PSS) (figure 2.7-a) is one of the most important and successful conducting polymers.

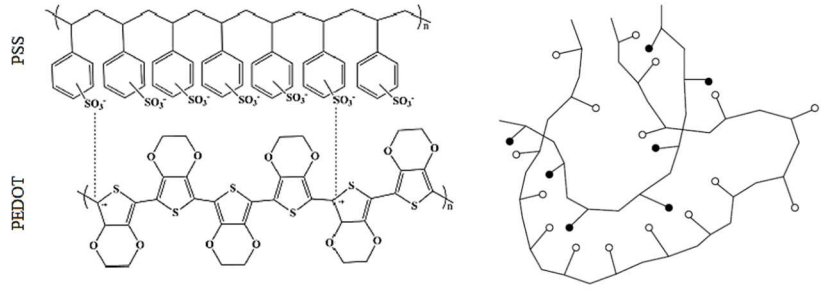

Figure 2.7. a) Chemical structure of PEDOT:PSS. b) Polyelectrolyte complex (PEC) structure scrambled egg type.

Poly(styrenesulfonic axis) (PSS) was the first material used as a polyelectrolyte complex with PEDOT in 1990 [26-27]. PSS is commercially available, soluble in water, forms durable films, and shows no absorption in the visible spectral range [27]. PSS is always used as a host electrolyte (HPE). The molar ratio of thiophene groups to sulfonic acid groups in standard PEDOT:PSS dispersions is in the range of 1:1.9 to 1:15.2, which corresponds to a weight ratio range of 1:2.5 up to 1:20 [28-29]. Due to the delocalization of positive charges in PEDOT, the resulting weak polar groups and the different spacing of charges in PEDOT compared to PSS, it can be assumed that the structure of PEDOT:PSS shows the form of a scrambled egg type (figure 2.7-b). The so-called scrambled egg type structure is based on random interactions between polar groups of one macromolecule and other polar groups of the polymer chains with no order [28]. Like most charged conjugated polymers, the PEDOT is not soluble in any solvent. The solvent of choice for the synthesis of PEDOT:PSS is water due to the fact that water is inert with respect to most oxidation or reducing agents and it is highly polar [26].

Aqueous PEDOT:PSS dispersions are commercially available from H. C. Starck Clevios GmbH. As a reference, table 2.2 summarizes some important properties of some Clevios PEDOT:PSS dispersions.

Commercial name	PEDOT:PSS ratio	Solid content (%)	Particle size d_{50} (nm)	Conductivity (S cm^{-1})
Clevios P CH 8000	1:20	2.5 – 30	25	10^{-5} – 10^{-6}
Clevios Al 4083	1:6	1.3 – 1.7	40	10^{-3} – 10^{-4}
Clevios P	1:2.5	1.2 – 1.4	80	0.2 – 1
Clevios PH 500	1:2.5	1.0 – 1.4	30	0.2 – 1
Clevios PH 510	1:25	1.5 – 1.9	30	0.2 – 1
Clevios PH 1000	1:2.5	1.0 – 1.3	30	0.2 – 1

Table 2.2. Commercial PEDOT:PSS dispersions in water and their properties.

All PEDOT:PSS dispersions showed in table 2.2 were developed as a requirement for different applications. For example, PEDOT:PSS CH 800 and Al 4083 are usually used as a hole injection layer on electronic devices [30-33], and other grades of PEDOT:PSS as PH500, PH510 or PH1000 are utilized as a conductive electrode on electronic devices [34-41].

2.2.2 PEDOT:PSS PROPERTIES

PEDOT:PSS is a conducting polymer with metal properties. The thiophene rings (see figure 2.7-a) form a conjugated π system being heavily p-doped. The PSS does not contribute to charge transport directly but acts as a template to keep PEDOT in the disperse state and provide film forming properties. The dissociated sulfonate groups balance the charges of the cationic PEDOT by forming a stable salt. PEDOT:PSS films can be deposited by common techniques as slit coating, drop casting, bar casting, spin coating, electrospinning, printing, and spraying. The PEDOT:PSS dispersions in water have been adjusted to the requirements of the specific deposition technique in order to obtain uniform films. The most important properties that determine the film quality are the viscosity, the surface tension and the adhesion to the substrate. These parameters can be varied by using different ratios of PEDOT to PSS. Spin coating is an easily accessible technique, which enables one to obtain uniform films of PEDOT:PSS in a thickness range from 15 to 300 nm. Typical curve of the thickness dependent on the spin speed (revolutions per minute) of two commercial grades of PEDOT:PSS (Al 4083 and PH500) are illustrated in figure 2.8 (This data were obtained with a Carl Süss RC8 spin coater with a rotating lid).

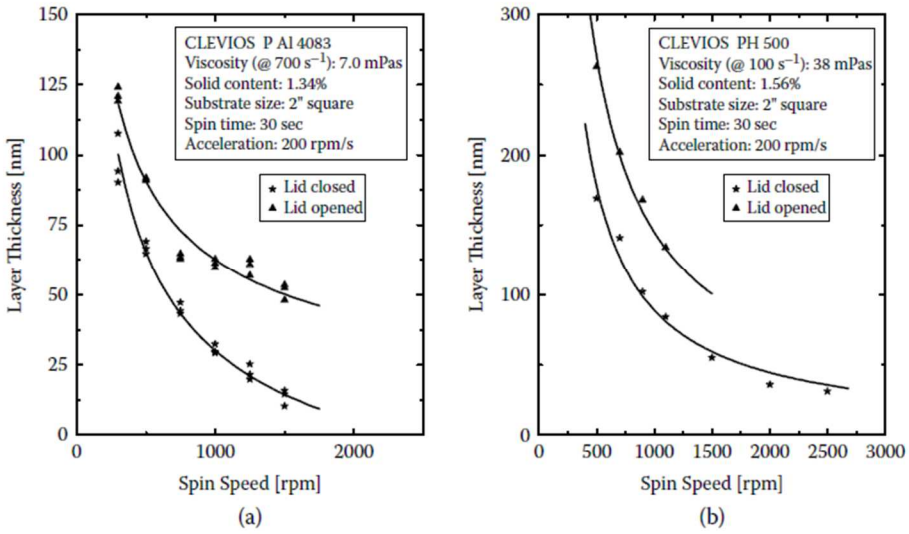

Figure 2.8. The curve of the thickness dependent on the spin speed (rpm) of PEDOT:PSS (a) Al 4083 and b) PH500 [28].

PEDOT:PSS films after deposition and prior to further processing have to be dried. Sometimes the water is removed by baking the layers at elevated temperatures, under infrared (IR) radiation, or by applying a

vacuum. Typically, the PEDOT:PSS films are dried leaving the coated substrates on a hot plate at temperatures above 100 °C for some minutes. But, one of the major advantages of PEDOT:PSS films is their thermal stability. Between 100 - 200 °C, the weight loss is only determined by evaporation water. However, at about 250 °C the sample weight decreases significantly [28].

The conductivity of PEDOT:PSS film is usually determined by depositing uniform thin films onto nonconductive substrates. Typically, the sheet resistance (R_{sq}) is measure via four-point probes. The resistivity (ρ) or it's inverse, the conductivity (σ), can be calculated by multiplying R_{sq} per the thickness film (t) according to:

$$\rho = \sigma^{-1} = R_{sq} \cdot t \qquad \text{Eq. 2.2}$$

The typical values of conductivity of different PEDOT:PSS-type are shown in table 2.2. However, the conductivity can be enhanced by several orders of magnitude with the addition of different additives during post-deposition treatment of the films (will be reviewed in the next subsection).

PEDOT:PSS films deposited on glass substrates present absorption spectra almost identical to the absorption of in situ chemically polymerized PEDOT without PSS. Figure 2.9 shows the relative transmission, absorption and reflection spectra of PEDOT:PSS PH1000 with 5 % DMSO added. The strong absorption at 193 and 225 nm, not shown in figure 2.9, are presented for pure PSS and PEDOT:PSS [42]. This can be attributed to π - π* transitions of the benzene rings in the PSS. The broad absorption band in the visible range and the IR region can be interpreted as the contribution of free carriers to absorption. The addition of additives like high boiling solvents does not affect the optical properties significantly {42}.

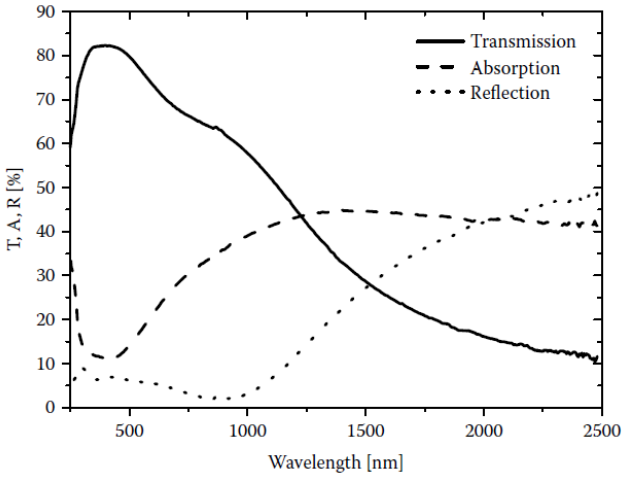

Figure 2.9. Transmission, absorption and, reflection spectra of PEDOT:PSS Clevios PH1000 including 5% DMSO [28].

The high transparency of PEDOT:PSS films in the visible range makes these films highly interesting as candidates for transparent polymeric electrodes. However, one should keep in mind that for high-conductive PEDOT:PSS films the IR reflection can reach 50 %.

The optical properties of PEDOT:PSS films depend on the PEDOT oxidation state and of the PSS composition, and this has motivated many groups to investigate the vibrational spectra by IR and Raman spectroscopy. In figure 2.10a-b several well-defined bands assigned to PEDOT vibrations in the region of 500 to 2000 cm^{-1} can be identified. The form of spectra and the relative intensity of the peaks depends on the oxidation level of PEDOT, especially the shape of the Raman band associated with C=C symmetrical stretching at 1400 to 1500 cm^{-1} has been used to distinguish PEDOT being in its benzenoid and quinoid form [43-46].

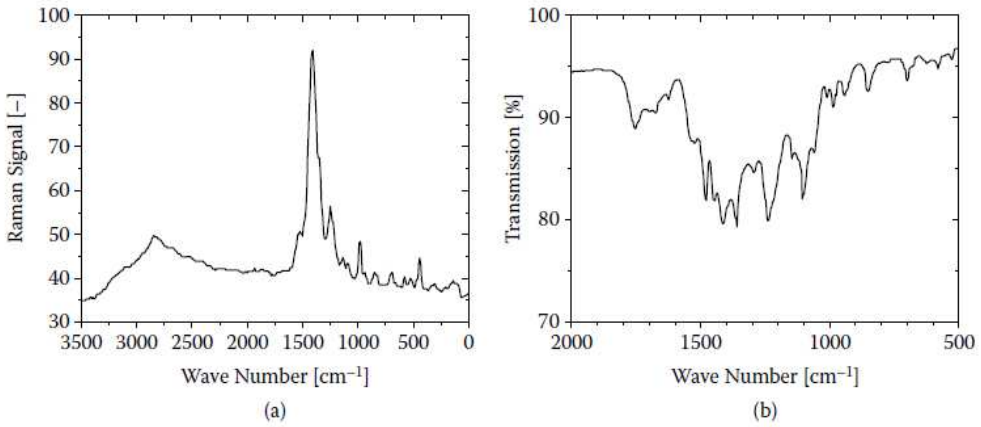

Figure 2.10. a) Raman spectroscopy and b) IR spectra for PEDOT:PSS [28].

PEDOT:PSS films are amorphous in the presence of the PSS properties, as when PEDOT films do not contain PSS exhibit a crystalline order and fibril-like structure [47-48].

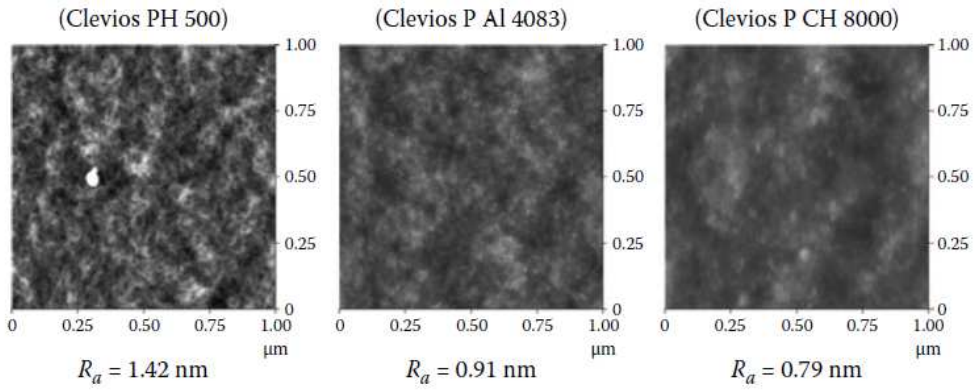

Figure 2.11. Atomic force microscopy images of various PEDOT:PSS-types differing in their ratio of PEDOT to PSS [28].

For the case of uniform thin films of PEDOT:PSS deposited by spin coating on a glass substrate, Greczynski et al. [49] found that PSS segregates in the surface to form a PSS-enriched phase of 30 to 40 Å thickness. It was observed that PEDOT:PSS films present a rather rough surface and a grain-like morphology with a nonuniform distribution of PEDOT and PSS.

Some publications [50-51] analyzed the surface roughness of PEDOT:PSS films with atomic force microscopy (AFM) and, it was conclusive that the surface roughness depends on the weight ratio of PEDOT to PSS and on the specific distribution of particle sizes. For example, PEDOT:PSS designed for hole injection (Clevios P CH 8000) with a weight ratio of PEDOT to PSS of 1:20 by weight and an average particle size of 25 nm forms films with a root-mean-square (RMS) surface roughness of RMS= 0.79 nm (figure 2.11), comparing Clevios PH 500, with a weight ratio of PEDOT to PSS of 1:2.5 and a similar particle size of 30 nm present an RMS= 1.4 nm (Figure 2.11).

2.2.3 SECONDARY DOPING

Since the PEDOT:PSS was developed, it has been one of the most important conducting polymers for its high transmittance in the visible range, good conductivity, excellent chemical and thermal stability and simple processing. Owing to this, it has been very attractive for optoelectronic applications. In polymer solar cells, it is utilized as a transparent electrode, as a hole-transporting layer, and as an anode interfacial layer to enhance the anode contact [52]. In hybrid solar cells, it is used as a smoothing coating layer of rough conducting surfaces and as a transparent p-type layer [53-55]. Specific applications require specific functional characteristics of the PEDOT, such as transparency, work function, and conductivity.

It has been shown in numerous works that the work function, and mainly the conductivity of the PEDOT:PSS can be significantly improved by secondary doping [30, 56-57]. Numerous studies have demonstrated that the conductivity and, in some cases, the work function can be modified by thermal and light treatments, organic solvent, ionic liquids, surfactants or, acid treatments. There is a large number of articles that report on the modification of some propertied of PEDOT:PSS films with various treatments, in the following we will briefly describe the most relevant for the purpose of this thesis work.

Huang et al. [58] reported the study of temperature dependence of the conductivity and the surface roughness of PEDOT:PSS, demonstrating that with a thermal treatment (up to 250 °C) the conductivity of PEDOT:PSS Al 4083 it could be improved as high as one order of magnitude (from 10^{-3} to 10^{-2} S/cm). The surface roughness also increases reaching a maximum at 200 °C. However, when the temperature is raised to 250 °C the roughness is reduced, this could be the evidence of the film degradation.

Moujoud et al. [59] and Lin et al. [60] reported that the work function can be modified through a UV-light treatment. They demonstrated that when a PEDOT:PSS film is irradiated for some minutes by a UV-light source. Moujoud et al. [59] irradiated a PEDOT:PSS film by a UV-light source with an output power density of 4 W/cm^2 with emission centered at 355 nm, the binding energy cutoff of its XPS spectra present a shift of to 0.18 eV. While Lin et al. [60] irradiated a PEDOT:PSS film by a UV-light source with an output power density of 0.46 W/cm^2 with emission centered at 365 nm, the binding energy cutoff of its XPS spectra presents a shift of to 0.25 eV. This means that the work function of PEDOT:PSS films with a UV-light treatment is higher by 0.18 and 0.25 eV respectively than that of PEDOT:PSS films without UV-light treatment. Apparently, the increase in the work function is attributed that coil conformation turns into linear or expanded-coil conformation and the number of the charge trapping related defects is reduced, resulting in an increase in the work function and the conductivity of PEDOT:PSS [60].

In the literature, there are several reports [30] about the significantly enhanced conductivity via treatment with organic solvents, either by the simple addition or by different post-deposition treatments. For addition processes, in particular, when dimethyl sulfoxide (DMSO) or ethylene glycol (EG) is added to the PEDOT:PSS solution, the films present the best conductivity enhancement, reaching values of up to about 700 S/cm. It is suggested, that when the solvents were added to the PEDOT:PSS solution, the PSS is rearranged and this process reduces its surface chain networks to enhance the conductivity [61-62]. Other materials added to PEDOT:PSS solution to enhanced its conductivity are N N-dimethyl formamide (DMF), tetrahydrofuran (THF), glycerol and sorbitol [63-65]. R. Syang-Peng et al. [66] used some treated with a solvent of pure water mixed with acetone, methanol, and ethanol. The screening effect due to the polar solvent, reducing the Coulomb interaction between PEDOT+ and PSS- chains, plays an important role in the conductivity enhancement.

Badre et al. [67] reported that adding 1-ethyl-3-methylimidazolium tetracyanoborate (EMIM TCB) (a commonly used ionic liquid) it is possible achieving a conductivity of up to 2084 S/cm, although the addition of these ionic liquids could be a problem for a good deposition of PEDOT:PSS films by spin coating due to that the viscosity of PEDOT:PSS solution is increased.

It is known that when a common organic solvent as ethanol, acetonitrile, acetone, or nitromethane are used to treat a PEDOT:PSS film its conductivity did not change remarkably [68]. However, Y. Xia et al. [69] found that the conductivity of PEDOT:PSS film was enhanced from 0.2 to 100 S/cm, when the film was treated with aqueous solutions of zwitterions. W. Zhang et al. [70] used isopropyl alcohol (IPA)-treated PEDOT:PSS film as an electron transport layer in a polymer solar cell, reveling the electron transport properties of IPA-treated PEDOT:PSS films in comparison with untreated PEDOT:PSS films.

M. Al-Hashimi et al. [51] focused their investigation in vapor treatments with DMF and ME, achieving conductivities up to about 200 S/cm.

In the acid treatment case, the post-deposition treatments are more commonly used. Cruz-Cruz and co-workers [71] added a small amount of sulfuric acid to PEDOT:PSS and obtained a conductivity of 200 S/cm. However, Xia et al. [72] and Kim et al. [73] reported that PEDOT: PSS films were immersed in a sulfuric acid solution, reaching conductivities of up to 3065 and 4380 S/cm respectively.

Many research groups have focused on improving the conductivity of the PEDOT: PSS. However, it is known that both conductivity and work function are critical to solar cell device performances.

Previously it has reported a universal method to reduce the work function on PEDOT:PSS up to 3.58 eV, using a polyethyleneimine ethoxylated (PEIE) or branched polyethyleneimine (PEI) film over PEDOT:PSS. Also, the conductivity is enhanced up to 500 S/cm [73-74]. On the other hand, in 2018, X. Wang et al. [75] reported a PEDOT thin film deposited by oCVD and hydrobromic acid treatment with a record-high electrical conductivity of 6259 S/cm and a work function of 5.33 eV.

It should be mentioned that most of the articles published about the methods to modify the properties of the PEDOT: PSS films are always focused on only one property either in conductivity or in the work function, and there are very few articles that focus on both properties at the same time.

2.3 HYBRID HETEROJUNCTIONS IN SOLAR CELLS

The operation of all solar cells is based on the photoelectric effect. However, the mechanisms that determine and limit their performance depends on the material properties used and the interfaces that they formed. These interfaces generally are formed by homojunctions and heterojunctions.

The heterojunction is the interface when two different semiconductor materials are juxtaposed. They are usually classified as dependent on doping. They are called “isotype” when both sides have the same doping and “anisotype” when both sides have different doping. The use of materials with different bandgaps, refractive indices, and other properties to form anisotype heterojunctions increases flexibility in the design of semiconductor devices and allows new functionality and higher performance. Also, these heterojunctions exhibit better current rectification and voltage-dependent capacitance. These heterojunctions are used in heterojunction bipolar transistors (HBT), heterostructure field-effect transistor (HFET), double heterojunction (DH), quantum laser diodes, high-performance light-emitting diodes (LED), photodiodes and solar cells [76].

The heterojunctions may abrupt or gradual. To form a gradual heterojunction, it is necessary to use an “alloy” because its properties can be tuned to some degree depending on the composition. The

heterojunctions performance depends mainly on the alignment of the energy bands in the interface. If two materials that form the heterojunction have different bandgaps, a band discontinuity exists at the interface denoted as ΔE_c and ΔE_v. The heterojunctions can be classified according to the magnitude of the band discontinuity. The type "nested" (figure 2.12-a), is the most common and important type, in which both ΔE_c and ΔE_v are positive and both electrons and holes might be confined in the narrower gap material. In type "staggered" (figure 2.12-b), both ΔE_c and ΔE_v have opposite signs and both electrons and holes can be confined in different layers. And, in type "misaligned" (figure 2.12-c), the rarest, both ΔE_c and ΔE_v have opposite signs and the band offset exceeds the bandgap. The spontaneous charge transfer from the valence band of one material to the conduction band of the other leads to the semi-metallic behavior [77].

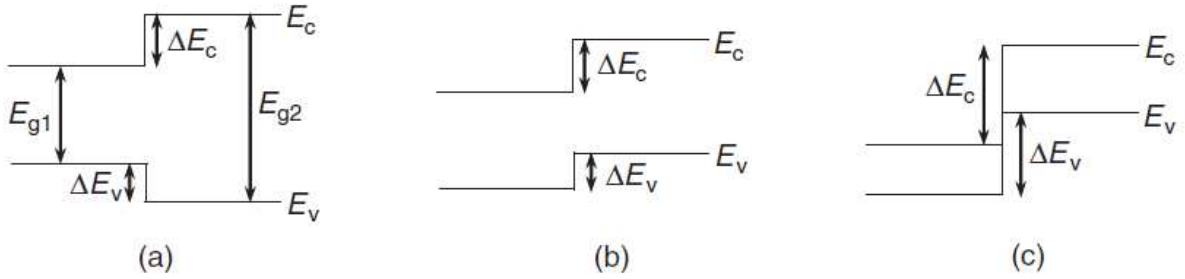

Figure 2.12. Types of semiconductor heterojunction band alignments: a) nested, b) staggered and c) misaligned.

In the case of solar cells, the successful operation of the photovoltaic device requires a staggered-type heterojunction because has cascading energy levels. This is required to allow that the electrons are transported to the cathode and the holes to the anode.

A homojunction formed by silicon films p-type and n-type is used in most of the commercial solar cells and are called solar cells "First generation" [78]. The called solar cells "Second generation" are formed by amorphous silicon thin films and two that are made from non-silicon materials namely cadmium telluride (CdTe), and copper indium gallium diselenide (CIGS). And, the called solar cells "Third generation" are the other photovoltaic devices including the most recent and that are in development as organic photovoltaic devices, hybrid photovoltaic devices, etc.

In the last decade, the organic polymer semiconductors have become an option to replace the p-type and n-type inorganic materials, in order to reduce costs and simplify the fabrication processes of the solar cells. Creating a new field investigation called "Hybrid solar cells", which consists of the investigation of devices formed by heterojunctions between organic and inorganic semiconductors [79-80]. Combining these two types of materials and taking advantage of their properties might offer a potential solution to create the next generation of low cost and efficient solar cells. Numerous hybrid

devices have been demonstrated combining organic materials such as P3HT, PEDOT:PSS, P3HT:PCBM with inorganic material as c-Si, a-Si:H [5, 81]. Diverse articles [82-83] have demonstrated the functionality of the Silicon/Organic Heterojunction (SOH) such as c-Si/PEDOT:PSS and c-Si/P3HT heterojunctions in solar cells (figure 2.13).

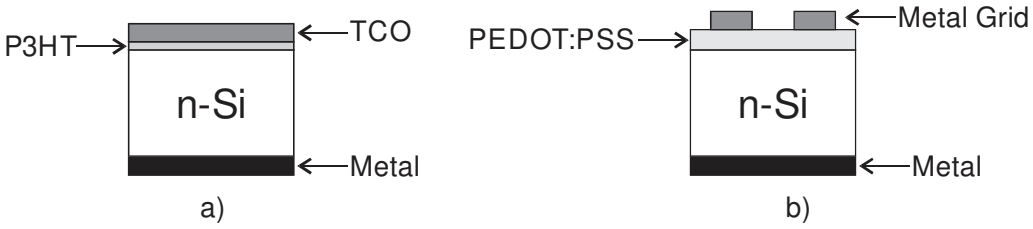

Figure 2.13. Silicon/Organic heterojunctions (SOH): a) c-Si/P3HT [82] and b) c-Si/PEDOT:PSS [83] applicated in solar cells.

In the case of the silicon/P3HT heterojunction (figure 2.13-a), the key band-alignment criteria is satisfied due to the fact that the HOMO and LUMO of P3HT are 5.2 and 3.1 eV respectively, compared to 5.17 and 4.05 eV for E_v and E_c of silicon respectively. Therefore, a large E_c-LUMO barrier of 0.8 eV and a negligible E_v-HOMO barrier at the silicon/P3HT heterojunction are expected [82]. And, in the case of the silicon/PEDOT:PSS heterojunction (figure 2.13-b), the HOMO and LUMO of PEDOT:PSS are 3.6 and 5.2 eV respectively. Thus, the E_c-LUMO barrier of 0.4 eV exist and, an E_v-HOMO barrier is negligible [83]. In these heterojunctions, both P3HT and PEDOT:PSS act as a doped p-type semiconductor, the LUMO levels of P3HT and PEDOT:PSS have an offset with conduction band of silicon, they form a barrier to electron dark current and the HOMO levels are closely aligned with the valence band of silicon, which allow holes in silicon to flow into P3HT or PEDOT:PSS unimpeded.

PEDOT:PSS polymer conductor has been one of the most used materials in hybrid solar cells due to its properties discussed in previous sections. In order to improve the performance of hybrid solar cells, diverse heterojunctions are been proposed. Among them are the heterojunction silicon/SiO_x/PEDOT:PSS, silicon/SiO_2/PEDOT:PSS or silicon/SiN_x/PEDOT:PSS, in which the dielectric layers are used to passivate the c-Si and as an anti-reflective layer, achieving improvements in the V_{oc} of the structure [6, 84-85].

In the case of a-Si:H based solar cells, in order to take the advantage of the excellent properties of intrinsic (undoped) a-Si:H, p-i-n or n-i-p heterojunction cell structures are used rather than the classic p-n structure of c-Si cells. In solar cells with p-i-n structure, the light is mainly absorbed by an intrinsic semiconductor (i), where the electron-hole pairs are generated. Both semiconductors p-type and n-type form an electric field to separate free charge carriers and these are collected by the metal electrodes.

PEDOT:PSS has also shown potential to replace the p-type material in thin film a-Si:H-based solar cells due to its large bandgap (1.6 eV), high work function (5 eV) and, the facility to modify its conductivity. The additional advantage is the possibility to simplify the fabrication processes of the frontal interfaces.

In table 2.3 a summary of some results reported in hybrid solar cells with polymer/a-Si:H interface are presented.

Type	Structure	T_d (°C)	Texturized	J_{sc} (mA/cm^2)	V_{oc} (mV)	FF (%)	PCE (%)	Ref.
p-i-n	ITO/PEDOT:PSS/a-Si:H(i)/µc-Si(i)/ µc-Si(n)/Pd	200	No	4.55	883	51	2.1	[54]
n-i-p	ITO/a-Si:H(n)/a-Si:H(i)/P3HT/Pd/Ag	80	No	4.22	704	60	1.6	[86]
p-i-n	ITO/PEDOT:PSS+Au-NPs/WO_3/ a-Si:H(i)/ a-Si:H(n)/Ag	---	Yes	14.60	560	67	5.49	[87]
p-i-n	ITO/PEDOT:PSS/ a-Si:H(i)/ a-Si:H(n)/Al	---	No	14.08	680	50	4.78	[88]
n-i-p	Ag/TCO/a-Si:H(n)/ a-Si:H(i)/PEDOT:PSS/TCO/Metal	---	No	19.1	800	48	7.40	[55]

Table 2.3. Summary of results reported in hybrid solar cells with a polymer/a-Si:H heterojunction.

In 2005, E. L. Williams et al. [54] introduced the concept of the a-Si:H/PEDOT:PSS heterojunction in a hybrid solar cell, achieving a power conversion efficiency (PCE) of 2.1 %. In 2007, P. J. Alet et al. [86] presented the a-Si:H/P3HT heterojunction in a hybrid solar cell, showing a PCE of 1.6 %. Then, eight years later, H. H. Jung et al. [87] improved the PCE of hybrid solar cell with the a-Si:H/PEDOT:PSS heterojunction to values of 5.49 %, using a texturized fluorine-tin-oxide (FTO) glass, an amorphous tungsten oxide (WO_3) layer and gold nanoparticles (Au-NPs) to prevent the degradation and to increase the short circuit current (J_{sc}) by plasmonic effects. In 2014, Y. Peng et al. [88] investigated different hybrid structures using the a-Si:H/PEDOT:PSS heterojunction, achieving a PCE of 4.78 % using a p-i-n structure.

It is commonly assumed that the performance parameters of the hybrid solar cells with the p-i-n structure are limited by the degradation of PEDOT:PSS due to exposure to high temperature (>200 °C) and ion bombardment during the plasma deposition subsequent layer (a-Si:H). For these reasons, in 2018, Y. J. Lee et al. [55] fabricated an n-i-p hybrid structure in order to avoid exposure of the PEDOT:PSS to high temperatures and ion bombardment. Finally, Y. J. Lee et al. improved the wettability of PEDOT:PSS on a-Si:H film and adding a p-type buffer layer achieved a PCE of 7.40 %.

CHAPTER III

3. EXPERIMENTAL METHODOLOGY

In this chapter, it is described in detail the fabrication and characterization processes of organics and inorganics films and hybrid photovoltaic devices studied in this work. In the first section, the materials, equipment, and process used for the organic and inorganic films and hybrid photovoltaic devices fabrication are described. In the second section, the equipment and techniques used for the organic and inorganic films and hybrid photovoltaic devices characterization are shown. Finally, in the last section, the variations of different processes in order to improve the performance characteristics of hybrid photovoltaic devices studied in this work are presented.

3.1 FABRICATION PROCESS

This work was mainly focused in two hybrid photovoltaic structures. These structures are shown in figure 3.1.

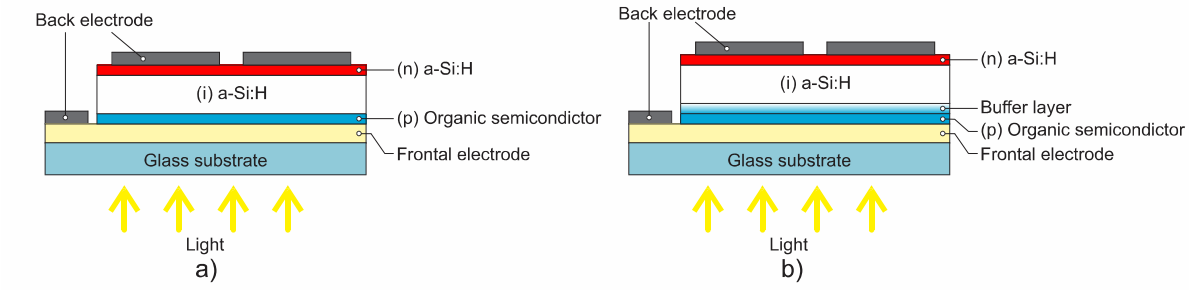

Figure 3.1. Structure configurations for hybrid photovoltaic devices a) p-i-n structure and b) p-i-n structure with a buffer layer.

Generally, the fabrication process of a hybrid photovoltaic devices consists of the following stages: 1) Frontal contact definition, 2) Substrate preparation, 3) Organic films deposition, 4) Inorganic films deposition, and 5) Back electrodes deposition. Each of these processes and, the main materials used for the fabrication of the films and the photovoltaic devices studied in this work are described in detail below.

3.1.1 FRONTAL CONTACT DEFINITION

The glass substrates used in this work have dimensions of 355.6 for 355.6 mm and 1.10 mm thick and coated with a 160 nm thick indium-tin-oxide film (ITO) with a sheet resistance of 14 Ω/sq purchased from Precision Glass & Optics (PG&O) (Santa Ana, CA, USA).

The configuration selected in this work required defining the active area. The active area of the devices is limited with a central circle of ITO defined by lithography using a mixture of hydrochloric acid and deionized water in 1:1 concentration. With this, four devices of an area of 0.154 cm^2 for each sample are obtained.

3.1.2 SUBSTRATE PREPARATION

For the deposition of the inorganic and organic films (a-Si:H, P3HT, etc.), a substrate with a hydrophobic surface is necessary. The substrates are cleaned as follows: 1) 10 minutes in trichloroethylene (TCE), 2) 10 minutes in acetone, and 3) 10 minutes in isopropyl alcohol (IPA), in an ultrasonic bath at room temperature. After this, the substrates are rinsed with deionized water three times and dried by centrifugation and/or with nitrogen flow.

However, for the deposition of organic films from aqueous solutions (PEDOT:PSS Al 4083, PEDOT:PSS PH1000, etc.), the cleaning process described above is not suitable, since a hydrophilic surface is needed [89]. Thus, the substrates are cleaned as following: 1) 20 minutes in a mixture of mucasol and deionized water in concentration 0.03:1, 2) 20 minutes in acetone, and 3) 20 minutes in isopropyl alcohol (IPA), in an ultrasonic bath at room temperature. After that, the substrates are rinsed with deionized water three times and dried by centrifugation and/or with nitrogen flow. With this cleaning process a hydrophilic surface is obtained and the deposition of PEDOT:PSS Al 4083 or PEDOT:PSS PH1000 on glass and glass/ITO substrates can be accomplished.

The laboratory equipment and organic solvents used for cleaning processes were purchased from the J.T Baker and Sigma-Aldrich companies.

3.1.3 ORGANIC FILMS DEPOSITION

Spin coating deposition is a solution-based technique for deposition of thin films developed for low-cost, room-temperature and atmospheric pressure deposition. The materials are ranging from polymer (as organic photoresist) to functional inorganic films including amorphous and crystalline chalcogenides [90-91].

Spin coating is performed in mainly three steps, deposition, spin-off, and evaporation, as shown in figure 3.2. In the first stage, the material is deposited on the turntable and then spin up occurs while the evaporation stage occurs throughout the process. The solution applied on the turntable is distributed via centrifugal force. High spinning speed results in the thinning of the layer. High volatile materials are removed from the substrate because of the evaporation or simply drying and the low volatile materials

of the solution remain on the surface of the substrate. The thickness of the deposited layer depends mainly on the viscosity of the coating solution and the speed of rotation [92].

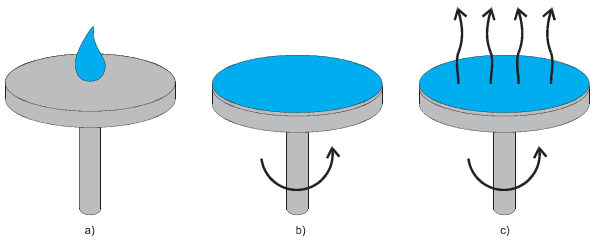

Figure 3.2. Stages of spin coating on a substrate a) Deposition, b) Spin-off and c) Evaporation.

For the deposition of water-no-based films (as P3HT purchased from Ossila Ltd. (Sheffield, UK)), a G3 Spin Coater Series model G3P-8 is used. This spin coater has a speed of rotation range from 0 to 9999 RPM and an acceleration from 1 to 25.5 rps. The process of spin coating is performed within a glovebox model LC-150 (from LC Technology Solution Inc., (Massachusetts, USA)) in a Nitrogen atmosphere. On the other hand, for the deposition of water-based films (as PEDOT:PSS Al 4083 and PEDOT:PSS PH1000 purchased from Ossila Ltd. (Sheffield, UK)), a spin coating Laurell model WS-650SZ-6NPP/A1/AR1 is used. This spin coater has a speed of rotation range from 50 to 3000 RPM and an acceleration from 1 to 500 rps. And, it requires a vacuum system with a pressure of at least 16 pa and nitrogen flow of at least 60 psi. The deposition of water-based films is performed at normal environmental conditions (in the air).

For both water-based and no-water-based films, the amount of solution and the speed of rotation depends on the required thickness.

3.1.4 INORGANIC FILMS DEPOSITION

Plasma Enhanced Chemical Vapor Deposition (PECVD) is a technique that by means of a plasma generated by an electric field, the ionization of process gases is enhanced, replacing the temperature as the main activation process of the deposition. The capability to perform low-temperature deposition of high-quality films is the advantage feature which makes it compatible with organic materials and flexible substrates.

For the deposition of the inorganic films (as silicon, silicon carbide, etc.), a cluster system purchased from MVSystem Inc. (Colorado, USA) is used. As shown in figure 3.3, the cluster system has the following four deposition chambers: PL2, chamber for p-type films (Gases: silane (SiH_4), germane (GeH_4), Methane (CH_4), Hydrogen (H_2), Diborane (B_2H_6) and, Argon (Ar)), PL3, sputtering chamber for

electrode deposition (Gas: Ar; silver (Ag) and Aluminum-Doped Zinc Oxide (AZO) targets), PL7, chamber for intrinsic films (Gases: SiH_4, GeH_4, H_2 and, Ar) and PL7, chamber for n-type films (Gases: SiH_4, GeH_4, H_2, phosphine (PH_3) and, Ar). Also, to avoid ambiental contamination in multi-layer thin film structures has an isolation transportation zone (ITZ) and a load lock (LL) chamber to provide isolation from the exterior.

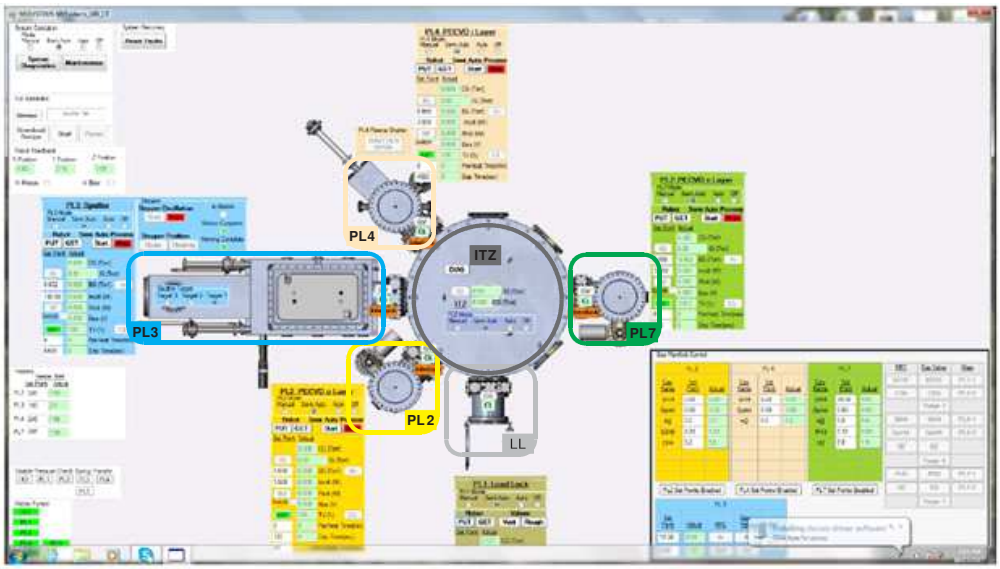

Figure 3.3. MVSystem cluster tool schematic.

In this work, various precursors and inert gases were used (which are listed in table 3.1) because the purest form of semiconductor material available is in the gas phase which provides enough quality to make possible the doping process.

Reactive gas	Balance	Purity	Manufacturer
SiH_4	10 % in H_2	SG	Mathelson, Inc.
H_2	--	SG	Mathelson, Inc.
CH_4	--	99.999 %	Infra
B_2H_6	10 % in H_2	SG	Mathelson, Inc.
PH_3	10 % in H_2	SG	Mathelson, Inc.
Ar	--	--	Infra
Nitrogen	--	--	Infra

Table 3.1. Properties of the gases used in the fabrication process.

The inorganic films to fabricate films and photovoltaic devices are deposited by this technique. Following the deposition parameters used for each film are presented.

For the deposition of intrinsic a-Si:H films, the PL4 chamber is used. These films are used in the two hybrid photovoltaic structures shown in figure 3.1 a-b. The deposition parameters, set by the user through a Human Machin Interface (HMI), which are shown in table 3.2.

Parameter	Range (Units)
Deposition time	From 0 (s)
Deposition pressure	0.3 – 1 (Torr)
Gas flow	0 - 100 (sccm)
Deposition power	0 - 100 (W)
Holder/Substrates temperature	From room temperature up to 325 °C / 220 °C

Table 3.2. Deposition parameters in PL4 (MVSystem) for intrinsic a-Si:H.

For the deposition of n-type a-Si:H films ((n)-a-Si:H), the PL7 chamber is used. These films are used in the two hybrid photovoltaic structures shown in figure 3.1 a-b. The deposition parameters, set by the user through an HMI, which are shown in table 3.3.

Parameter	Range (Units)
Deposition time	From 0 (s)
Deposition pressure	0.3 – 1 (Torr)
Gas flow	0 - 100 (sccm), 0 – 20 (sccm for dopant gases)
Deposition power	0 - 100 (W)
Holder/Substrates temperature	From room temperature up to 325 °C / 220 °C

Table 3.3. Deposition parameters in PL7 (MVSystem) for (n)-a-Si:H films.

For the deposition of carbon graded to silicon films (a-Si:C:H), the PL2 chamber is used. These films only are used in the hybrid photovoltaic structure shown in figure 3.1-b. The deposition parameters, set by the user through an HMI, which are shown in table 3.4.

Parameter	Range (Units)
Deposition time	From 0 (s)
Deposition pressure	0.3 – 1 (Torr)
Gas flow	0 - 100 (sccm), 0 – 20 (sccm for dopant gases)
Deposition power	0 - 100 (W)
Holder/Substrates temperature	From Room temperature up to 325 °C / 220 °C

Table 3.4. Deposition parameters in PL2 (MVSystem) for a-Si:C:H films.

3.1.5 ELECTRODES DEPOSITION

Electrodes for the photovoltaic devices studied in this work can be opaque/highly reflective or transparent conductors depending on the configuration structure. In the frontal contact, high transmittance and low resistance are the main features required. In the back contact, high reflectivity and low resistance is the required feature.

For the back-metal electrodes, a sputtering deposition system from “AJA International, Inc.” for the deposition of titanium (Ti) films is used. Ti electrodes are growing at 3-4 Å/s rate in a vacuum level of about 5 x 10^{-5} Torr in the Balzers metal evaporator. Typically, Ti electrodes thickness is about 150 nm. Meanwhile, an r.f. sputtering from the “MVSystem Inc.” cluster for the deposition of Ag films is used.

Typically, Ag electrodes thickness is about 180 nm. Deposition parameters for both Ti and Ag electrodes are summarized in table 3.5.

Material	System	Power (W)	Pressure (mTorrs)	Flow (Ar)	Thickness (nm)
Ti	"AJA International, Inc."	200	3	12 sccm	150
Ag	"MVSystem, Inc."	75	2	10 sccm	180
AZO	"MVSystem, Inc."	100	2	12 sccm	255

Table 3.5. Deposition parameters for back metal electrodes by sputtering.

For the transparent electrodes (e.g. ITO films), a sputtering system from "AJA International, Inc." for the deposit of ITO films is used. Typically, ITO electrodes thickness is about 160 nm. Also, an r.f. sputtering from the "MVSystem Inc." cluster for the deposition of AZO films is used. Typically, AZO electrodes thickness is about 250 nm.

3.2 FILMS CHARACTERIZATION

3.2.1 THICKNESS AND DEPOSITION RATE

Film thickness is obtained by step measurements on the films with a "Dektak XT" profilometer from "Bruker Corporation" with a vertical resolution of 0.5 nm. The thickness value is calculated from the average of five measurements done at different points of the samples.

In the case of inorganic films, the deposition rate (r_d) is determined from the average thickness and deposition time (t_d). This value es calculated under the assumption that r_d is a linear as a function of the time and is established as:

$$r_d = \frac{t\,[m]}{t_d\,[sec]} \qquad \text{Eq. 3.1}$$

where t is the film thickness and t_d is the deposition time.

In the case of organic films, the most important factor that defines the organic film thickness deposited by spin coating is the spin speed. The first description of the flow of a viscous liquid on a rotating disk was given by Emslie et al. [93], who solved the hydrodynamic equations to obtain an equation that predicts the thickness in a case of a Newtonian fluid. However, this model does not consider the spatial and temporal variations, gradients, viscosity and solvent evaporation [94]. Afterward, with subsequent studies, the experimental data have been fitted empirically [94-95]. For the case of polymeric organic materials, the simplified functional dependence was obtained through the adjustment of experimental results, which can be fitted to the following equation [96]:

$$h = k\omega^{\alpha} \qquad \text{Eq. 3.2}$$

where h is the film thickness, ω is the angular speed and k and α are constants. The constants k and α depend on the physical properties of the material, solvent, and substrate, as well as on the interactions between material/solvent and solution/substrate.

3.2.2 DARK CONDUCTIVITY AND PHOTOCONDUCTIVITY

Both dark conductivity (σ_d) and AM1.5 conductivity (σ_l) are important to know because they define the quality of device films. A pair of Ti electrodes in the form of two parallel strips on top of a glass substrate was deposited to get contact with the studied films for electrical measurements. The schematic of the configuration for dark conductivity and photoconductivity measurements is shown in figure 3.4 below:

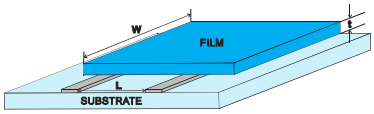

Figure 3.4. Schematic of the configuration for dark conductivity and photoconductivity measurements.

The I-V curves were obtained under dark and illumination conditions. In all cases, the current was a linear function of the voltage. For the analysis, the Ohm's law (V= IR) was applied, and the resistance was calculated. Using the I-V curves under dark the resistance value and the dark conductivity can be obtained with the relationship below:

$$\sigma_d = \frac{L}{RWt} \qquad \text{Eq. 3.3}$$

where R is the resistance calculated, t is the film thickness and L and W are the geometric parameters showed in figure 3.4. Photoconductivity of films is calculated from the conductivity under illumination (σ_l) and dark conductivity (σ_d) as follow:

$$\sigma_{ph} = \sigma_l - \sigma_d \qquad \text{Eq. 3.4}$$

where σ_{ph} is the photoconductivity, σ_d is the dark conductivity and σ_l is the AM1.5 conductivity. To calculate the AM1.5 conductivity, the steps followed for dark conductivity calculus were used. The AM1.5 conductivity under illumination with a power of 100 mW/cm^2 was measured with an "Oriel 2A" solar simulation from "Newport Corporation".

3.2.3 ELECTRICAL CONDUCTIVITY AND WORK FUNCTION

Electrical conductivity is the measure of the material's ability to conduct an electric current. Conductivity (σ) is the inverse of resistivity (ρ). The ρ is commonly defined as the sheet resistance (R_{sq}) of a material by its thickness (t) (see eq. 2.2).

So, the ρ and σ can be calculated, if the sheet resistance and the material thickness are known. This allows for the materials to be electrically characterized, only by measuring their sheet resistance. The main technique for measuring the sheet resistance is the four-probe method, which is performed using a four-point probe. In figure 3.5, a four-point probe setup is shown, which consists of four electrical probes in a line with equal spacing between each of the probes.

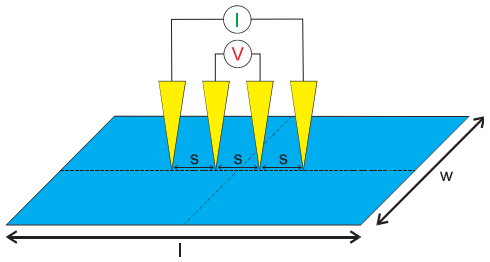

Figure 3.5. A schematic diagram of a four-point probe setup.

The four-point probe works by applying a current (I) on the outer two probes and measuring the resultant voltage between the inner two probes. The sheet resistance can then be calculated using the equation below:

$$R_{sq} = \frac{\pi}{\ln(2)} \frac{\Delta V}{I} = 4.53236 \frac{\Delta V}{I} \qquad \text{Eq. 3.5}$$

The equation 3.5 is only valid if: 1) the material tested is no thicker than 40 % of the spacing distance between the probes, and 2) the distance between the probes and the border of the sample is sufficiently large (typically 40 times greater than the spacing between the probes). If this is not the case, the possible current paths between the probes are limited by the proximity to the borders of the sample, resulting in an overestimation of the sheet resistance. Then, geometric correction factors are needed to account for the size, shape, and thickness of the sample. For different sample shapes and for measurements not performed at the center of the sample, alternative correction factors are required, which can be found in the article "*Geometric Factors in Four Point Resistivity Measurement"* [97].

In the case of a rectangular sample, to determinate the geometrical correction factor a table of empirically determined correction factors (consulted in "*Measurement of Sheet Resistivities with the Four-Point Probe"* [97-98]) was used. To calculate the geometric correction factor, the lateral dimensions of the sample ($L\ and\ W$) and the spacing distance between probes (s) must be known. Then, the values resulting of divisions $\frac{L}{W}$ and $\frac{W}{s}$ can be obtained. Once they are known, the corresponding factor in the before mentioned table [97-98] can be found. The measured sheet resistance is multiplied by this value to get the correct value for the sample. Obviously, not every sample will fall neatly into these categories.

If this is the case, it is recommended to use cubic spline interpolation to estimate the appropriate correction factor for the sample.

In this work, sheet resistance was measured by the four-point probe method using a Keithley 6517A electrometer. The 6517A Electrometer/High Resistance Meter offers reading rates of up to 125 readings/second and, an easy, quick way to measure low-level currents

Another important parameter is the work function (WF), which is the minimum energy (measured in eV) necessary to move an electron from the conduction band to the vacuum in the case of metals and semiconductors. The WF is a fundamental property of any solid with a band-like electronic structure (both empty and partially filled). The easiest technique for measuring the WF is the Kelvin probe method, which is performed using a Kelvin probe experimental setup (showed in figure 3.6). The determination of the WF is based on the measurement of the electrostatic forces between the Kelvin probe and the sample when an AC voltage ($V_{AC}\, sin(\omega t)$ at the frequency ω) and a DC voltage (V_{DC}) are applied to the sample. The Kelvin probe and the sample are characterized (in general) by different work functions. When both elements are brought in contact, a net electric current would flow between them until the Fermi levels are aligned.

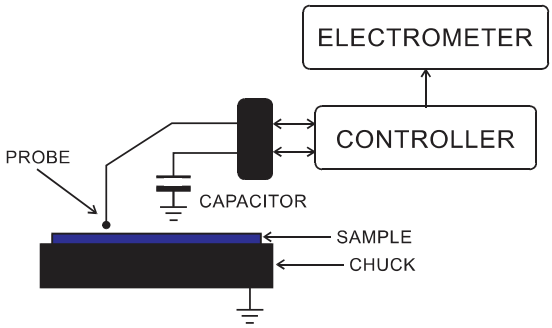

Figure 3.6. A schematic diagram of a Kelvin probe experimental setup.

The difference between the work functions is called the contact potential difference and it is denoted generally as V_{CPD} due to this potential, an electrostatic force exists between the probe and the sample. This electrostatic force can be expressed as:

$$F = F_{DC} + F_{\omega} + F_{2\omega} \qquad \text{Ec. 3.6}$$

where the component F_{DC} can contribute to the topographical signal, the term $F_{2\omega}$ can be used for capacitance microscopy and the term F_{ω} at the characteristic frequency ω, is used to measure the contact potential. F_{ω} can be expressed as:

$$F_\omega = \frac{dC}{dz}(V_{DC} - V_{CPD}) \cdot V_{AC}\, sin(\omega t) \qquad \text{Ec. 3.7}$$

where V_{DC} and $V_{AC}\, sin(\omega t)$ are voltages applied between the probe and the sample For the contact potential measurements, a lock-in amplifier is used to detect the oscillation at ω. During the measurement the V_{DC} has to be adjusted so that the electrostatic forces between the probe and the sample become zero and thus the $V_{AC}\, sin(\omega t)$ at the frequency ω, becomes zero. In equation 3.7, it can be seen that the electrostatic force at ω depends on $V_{DC} - V_{CPD}$, the value of V_{DC} that minimizes the term $V_{AC}\, sin(\omega t)$ corresponds to the contact potential difference (V_{CPD}).

For this thesis, the work function was measured using an experimental setup with a Kelvin probe from Besoke Delta Phi (Julich, Germany) with a probe diameter of 3 mm in the air at room temperature. Before obtaining the absolute values of WF of our samples, first, the Kelvin probe setup was calibrated against a reference sample of an ambiently stable and known WF (in this case a HOPG sample was used).

3.2.4 OPTICAL TRANSMITTANCE

Optical transmission spectra was measured in order to know the spectral range of optical transparency. With optical transmission spectra, the refraction index, the absorption coefficient as a function of wavelength can be predicted, and then estimate the optical bandgap.

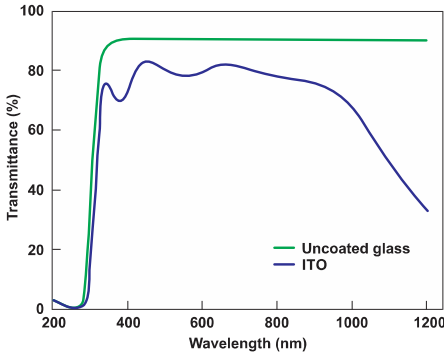

Figure 3.7. Optical transmission spectra of ITO film and uncoated glass substrate.

The optical transmission spectra can be divided into four regions. In the transparent region (where the absorption is zero) the transmission is mainly determined by the refraction index. In the weak absorption region, the absorption coefficient is small but starts to reduce the transmission. In the region of medium absorption, the absorption coefficient is large and in the region of strong absorption the absorption coefficient is very large, and the transmission decreases drastically.

Optical transmission measurements were performed using an MProbe 20 UV-Vis spectrometer from SemicondSoft Inc (Southborough, MA, USA). In figure 3.7, an optical transmission spectrum is shown.

3.2.5 RAMAN SPECTROSCOPY

Raman spectroscopy is a characterization method used to determine the vibrational modes of molecules, although rotational and other low-frequency modes of materials may also be observed. Raman spectroscopy is based on the inelastic scattering of photons, which it is known as Raman scattering. A source of monochromatic light (usually a laser) is used to interact with the molecular vibrations, photons or other excitations in the material, resulting in the energy of the laser photons being shifted up or down. The shift in energy gives information about the vibrational modes in the material.

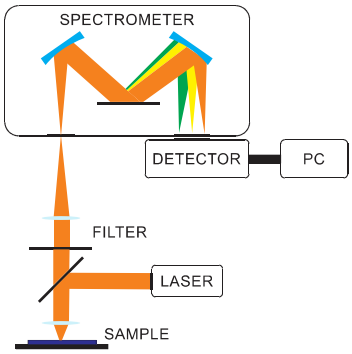

Figure 3.8. Schematic of one Raman spectroscopy setup

Typically, a sample is illuminated with a laser beam. Electromagnetic radiation from the illuminated spot is collected with a lens and sent through a monochromator. Elastically scattered radiation at the wavelength corresponding to the Rayleigh scattering is filtered out by a filter, while the rest of the collected light is dispersed onto a detector.

For this work, Raman spectra were measured using an AFM-Raman of Ntegra Spectra systems from NT-MDT Inc with a wavelength of the excitation laser of 532 nm.

3.2.6 FOURIER-TRANSFORM INFRARED SPECTROSCOPY (FTIR)

Fourier transform infrared spectroscopy (FTIR) is a technique used to obtain an infrared spectrum of absorption or emission of material. When a sample is exposed to infrared radiation, sample molecules selectively absorb radiation of specific wavelengths which causes the change of dipole moment of sample molecules. Consequently, the vibrational energy levels of sample molecules transfer from ground state to excited state. The frequency of the absorption peak is determined by the vibrational energy gap. The number of absorption peaks is related to the number of vibrational freedoms of the molecule. The intensity of absorption peaks is related to the change of dipole moment and the possibility of the transition

of energy levels. Therefore, by analyzing the infrared spectrum, one can readily obtain abundant structural information.

The commonly used region for infrared absorption spectroscopy is from 4000 to 400 cm^{-1} because the absorption radiation of most organic compounds and inorganic ions is within this region. Computer processing is required to turn the raw data (light absorption for each mirror position) into the desired result (light absorption for each wavelength). The processing required is a common algorithm called the Fourier transform. The Fourier transform converts one domain (in this case displacement of the mirror in cm) into its inverse domain (wavenumbers in cm^{-1}). The raw data is called an "interferogram".

A common FTIR spectrometer consists of a source, interferometer, sample compartment, detector, amplifier, A/D converter, and a computer. The source generates radiation which passes the sample through the interferometer and reaches the detector. Then the signal is amplified and converted to a digital signal by the amplifier and analog-to-digital converter, respectively. Eventually, the signal is transferred to a computer in which Fourier transform is carried out. Figure 3.9 is a block diagram of an FTIR spectrometer.

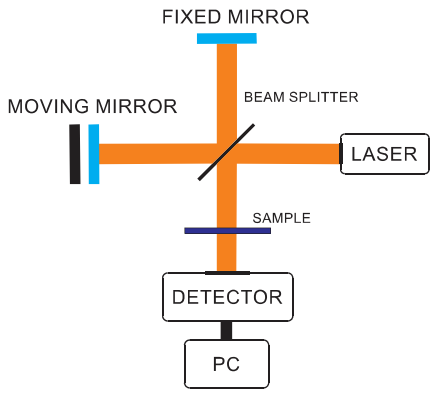

Figure 3.9 Block diagram of an FTIR spectrometer.

FTIR analysis was carried out in PEDOT:PSS PH1000 films on silicon wafers using a Nicolet iS5-FT spectrometer from Thermo Scientific Nicolet Inc.

3.2.7 ATOMIC FORCE MICROSCOPY (AFM)

Atomic force microscopy (AFM) technique is used for the morphology film characterization. The AFM is a technique for quantitative nanometer-scale surface roughness. The AFM generally works with a laser beam focused on the cantilever which is reflected onto a four-quadrant photodetector. The data collected by the photodetector are the variations of the z-position of the sample (figure 3.10). Morphology

measurements are performed by an NTEGRA platform from NT-MDT Inc (Liestal, Switzerland). Statistical analysis of surface morphology was applied to AFM images by computer software and roughness morphological parameters were obtained.

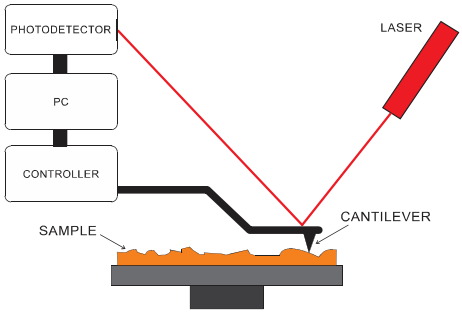

Figure 3.10. Schematic illustration of the main components in an AFM.

In the morphology analysis, three main parameters were determined. 1) The root mean square roughness (RMS) represents the standard deviation of the distribution of surface heights. 2) Skewness is used to measure the symmetry of the profile about the mean line and 3) Kurtosis which is used to measure the peakness of the profile [99].

3.2.8 SCANNING ELECTRON MICROSCOPY (SEM)

Scanning electron microscopy (SEM) is a technique capable of producing high-resolution images of the surface of a sample using electron-materia interactions. It uses an electron beam to form an image.

In the SEM microscope (see figure 3.11) it is necessary to accelerate the electrons in an electric field, to approach their wave behavior, which takes place in the microscope column, where it is accelerated by a potential difference that can range from 50 to 30,000 V. The electrons accelerated to leave the source and are focused by the condenser and objective lenses, whose function is to reduce the image of the filament so that the smallest possible beam of electrons affects the sample (in order to have a better resolution). With this fine electron beam, the sample is swept, point by point and line by line.

Electrons accelerated by a small voltage are used for very sensitive samples, such as biological samples without additional preparation or very insulating samples. High voltages can be used for metallic samples since they are generally successful without damages and in this way the shorter wavelength is used to have a better resolution.

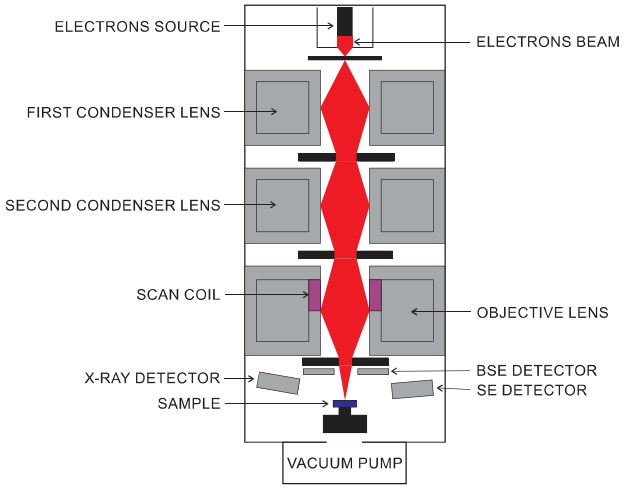

Figure 3.11. Schematic illustration of the main components in a scanning electron microscope (SEM).

When the beam impinges the sample, many interactions occur between the beam electrons and the atoms of the sample. On the other hand, the energy that electrons lose when they collide against the sample can cause that other electrons are expelled (secondary electrons) or X-rays, Auger electrons, etc. Also, with the secondary electrons rejected from the sample a spectrographic analysis of the sample composition can be obtained. The organic film nanostructure was characterized using an FEI Scios Dual-Beam scanning electron microscope (SEM) (Oregon, USA).

3.3 HYBRID PHOTOVOLTAIC DEVICES CHARACTERIZATION

The technique most used to evaluate photovoltaic device performance is the measurements of the current-voltage (I-V) curve under AM1.5 illumination conditions. The performance parameters as open circuit voltage (V_{oc}), short circuit current density (J_{sc}), fill factor (FF), power conversion efficiency (PCE), series resistance (R_s) and shunt resistance (R_{sh}) are used to compare the results with data from literature and also to analyze the effect of the variation of materials, structures and fabrication parameters on the photovoltaic device performance. These parameters are obtained through the analysis of the I-V curve under AM1.5 illumination conditions.

The current-voltage curves under AM1.5 illumination conditions were measured using a 6517A electrometer from “Keithley Instruments Inc” (which presents a digit resolution of 100 nA and a accuracy of 0.1 in the range of mA), a solar simulator Oriel Sol2A from “Newport Corp” (power density of 100 mW/cm^2), a GPIB interface and microprobes to mechanically contact the samples. In figure 3.12-a, the

experimental setup used to perform the current-voltage measurements, under AM1.5 illumination conditions, is shown.

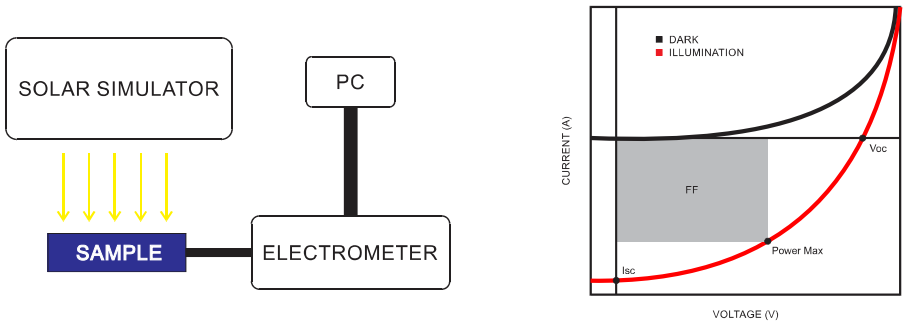

Figure 3.12. a) Schematic diagram of the experimental setup for measurements of current-voltage characteristics of a PV device under AM1.5 illumination and b) Typical current-voltage curve for a PV device under AM1.5 illumination and dark conditions.

A typical I-V curve under AM1.5 illumination conditions is shown in figure 3.12-b. From the I(V) curve the following parameters are obtained as is below shown.

1) Open Circuit Voltage (V_{oc}) is the voltage when the current is equal to zero.

2) Short circuit current density (J_{sc}) is the current density when the voltage is equal to zero.

3) Fill Factor (FF) is defined as the ratio the maximum power from the solar cell to the product of V_{oc} and J_{sc} parameters and it is expressed by:

$$FF = \frac{V_{max}\, J_{max}}{V_{oc}\, J_{sc}} \qquad \text{Eq. 3.8}$$

Where V_{max} and J_{max} belong to the point of the I-V curve where maximum power is produced. This point is the one that delimits the area of the rectangle that defines the FF.

4) Power conversion efficiency (PCE) represents the ratio of the maximum power obtained from the photovoltaic device to the total input power (100 mW/cm^2) and it is calculated by:

$$PCE = \frac{V_{max}\, J_{max}}{P_{in}} = \frac{V_{oc}\, J_{sc}}{P_{in}} \cdot FF \qquad \text{Eq. 3.9}$$

5) “Parasitic” resistances in a solar cell are R_s and R_{sh}. The effect of “parasitic” resistances is mainly reflected in the fill factor. Rs in a solar cell has three main causes: First, the internal resistance of the material to the flow of the current; secondly, the contact resistance between the electrodes and the semiconductors; and, finally, the net resistance of the topper and lower metal contacts [100]. R_{sh} in a solar cell brings significant energy losses typically caused due to fabrication defects. Low R_{sh} causes

power losses, providing an alternative current path (bypass leakage current or current suppression) for the generated photocurrent [100].

In figure 3.13, an equivalent circuit model is presented. The main elements of the equivalent circuit for I(V) characteristics under illumination are a current source (I_L) shunted by an ideal diode (I_D), together with a series resistance (Rs) and, a shunt resistance (Rsh) which are considered as "parasitic" circuit elements.

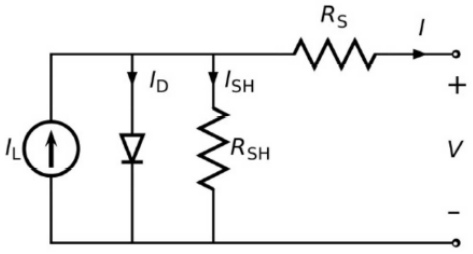

Figure 3.13. Equivalent circuit of a photovoltaic device.

Using the model of an equivalent circuit (shown in figure 3.13) the R_s can be determined as:

$$R_s \approx -\frac{dV}{dI} \quad When\ I = 0 \qquad \text{Eq. 3.10}$$

In the same way, as the R_s was obtained, R_{sh} can be obtained as:

$$R_{sh} \approx -\frac{dV}{dI} \quad When\ V = 0 \qquad \text{Eq. 3.11}$$

3.4 STUDIES OF THE FABRICATION OF THE POLYMER/A-SI:H HETEROJUNCTION IN HYBRID PHOTOVOLTAIC DEVICES

In the previous sections, we described the basic fabrication process and the characterization methods of organic and inorganic films and hybrid photovoltaic devices. In this work, we proposed some experiments that consisted of the variation of some fabrication parameters or fabrication processes and observing its effects in hybrid photovoltaic device's performance. In the following sections, the variations in the process parameters or fabrication processes are briefly described.

3.4.1 STUDY OF THE BACK INTERFACE IN HYBRID PHOTOVOLTAIC DEVICES

Study of different back electrodes in hybrid photovoltaics devices

The back-metal electrodes play a very important role in hybrid photovoltaic devices because highly reflective films are preferred to collect the optimum amount of light within a finite intrinsic layer thickness.

So, hybrid photovoltaic devices with different back electrodes were fabricated to observe its effect on the performance characteristics of hybrid photovoltaic devices. In table 3.6, the nomenclature used to the fabrication of hybrid photovoltaic devices with different back electrodes is presented.

Sample	Electrode
H36	Ti
H37	Ag

Table 3.6. Nomenclature for hybrid photovoltaic devices with different back electrodes

Study of AZO/Ag interface in hybrid photovoltaics devices

In order to improve the back interface, hybrid photovoltaic devices with an AZO film of different thicknesses between the n-type layer and the metal electrode were fabricated to observe its effect on the performance characteristics of hybrid photovoltaic devices. In table 3.7, the nomenclature used to the fabrication of these hybrid photovoltaic devices is presented.

Sample	Electrode	AZO (nm)
H316-A	Ag	0
H316-B	AZO/Ag	10
H316-C	AZO/Ag	100
H316-D	AZO/Ag	250

Table 3.7. Nomenclature for hybrid photovoltaic devices with different thicknesses of AZO film.

3.4.2 STUDY OF THE DEPOSITION TEMPERATURE AND PRESSURE OF A-SI:H FILMS BY PECVD

As previously mentioned, the device-quality silicon films can be evaluated through the dark conductivity and AM1.5 conductivity. In order to obtain a-Si:H films optimized, a-Si:H films with different deposition pressures at 220 °C and 175 °C were fabricated. In the tables below (table 3.8 and 3.9) the nomenclatures for these two experiments mentioned are shown.

Sample	Deposition pressure (Torrs)
M1	430
M2	530
M3	630
M4	730
M5	830

Table 3.8. Nomenclature for a-Si:H films at different deposition pressure at 220°C.

Sample	Deposition pressure (Torrs)
M6	430
M7	530
M8	630
M9	730
M10	830

Table 3.9 Nomenclature for a-Si:H films at different deposition pressure at 175°C.

Afterward, due to that the pairs electrons-holes photogenerated in a photovoltaic device mainly depends on dark conductivity and AM1.5 conductivity of a-Si:H films. Hybrid photovoltaic devices with a-Si:H films deposited to different deposition pressures were fabricated to observing the effect of the dark conductivity and AM1.5 conductivity of a-Si:H films on performance characteristics of hybrid photovoltaic devices. The nomenclature used to the fabrication of hybrid photovoltaic devices with a-Si:H films deposited to different deposition pressures at 220°C (see table 3.10) and 175°C (see table 3.11) are presented.

Sample	Deposition pressure (Torrs)
H151	730
H153	630
H156	550
H161	430

Table 3.10. The nomenclature used to hybrid photovoltaic devices with a-Si:H films deposited to different pressures at 220°C.

Sample	Deposition pressure (Torrs)
H190	730
H197	630
H200	550
H188	430

Table 3.11. The nomenclature used to hybrid photovoltaic devices with a-Si:H films deposited to different pressures at 175°C.

3.4.3 STUDY OF THE FRONTAL INTERFACE IN HYBRID PHOTOVOLTAIC DEVICES

Comparison between different organic materials as a p-type layer in hybrid photovoltaic devices

As was previously mentioned, the hybrid heterojunction with organic and inorganic materials requires optimization. In order to improve the frontal interface of hybrid photovoltaic devices studied in this work, three different materials (P3HT, PEDOT:PSS Al4083 and, PEDOT:PSS PH1000) were used as a p-type layer on hybrid photovoltaic devices. Thus, three different hybrid photovoltaic structures with a different varied p-type layer were fabricated.

The nomenclature used to the three hybrid solar cells with a different p-type layer is shown in table 3.12.

Sample	p-type layer
H28	P3HT
H103	PEDOT:PSS Al 4083
H106	PEDOT:PSS PH1000

Table 3.12. Nomenclature for hybrid solar cells with a different p-type layer.

Study of buffer layers in hybrid photovoltaic devices

Furthermore, the hybrid photovoltaic devices require optimization via a buffer layer and post-deposition treatments of organic films for application in organic-inorganic heterojunctions. Therefore, for this study, four hybrid photovoltaic devices with different configurations (using buffer layers) were fabricated. In figure 3.14 the four configurations are shown.

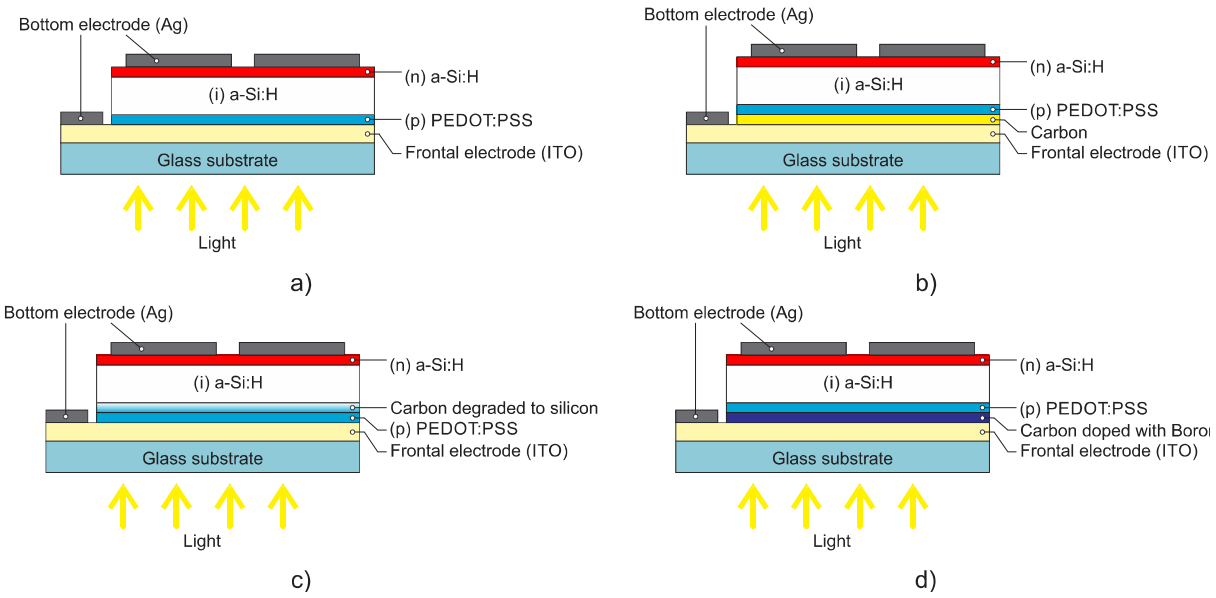

Figure 3.14. Hybrid solar cells with different configurations using a buffer layer.

The nomenclature used for the four hybrid solar cells with different configurations using a buffer layer is shown in table 3.13.

Sample	Configuration	Buffer layer
H206	Figure 3.14 a)	Without
H207	Figure 3.14 b)	Carbon
H208	Figure 3.14 c)	Carbon graded to silicon
H209	Figure 3.14 d)	Carbon doped with Boron

Table 3.13. Nomenclature for hybrid solar cells with different configurations using a buffer layer.

Study of PEDOT:PSS PH1000 films dipped in IPA in hybrid photovoltaic devices

In order to increase the fill factor of hybrid photovoltaic devices, the electrical and morphological characteristics of PEDOT:PSS PH1000 are modified via isopropyl alcohol (IPA) treatments. Therefore,

the effect of the dipping time of PEDOT:PSS PH1000 films in IPA on optoelectronic properties was studied.

Consequently, four hybrid solar cells with a p-type layer (PEDOT:PSS PH1000) modified via different dipping times in IPA were fabricated. The nomenclature used to the four different hybrid solar cells mentioned is shown in table 3.14.

Sample	Immersion time in IPA (min)
H167	0
H168	15
H169	30
H170	45

Figure 3.14. Nomenclature for hybrid solar cells with a p-type layer (PEDOT:PSS PH1000) modified via different dipping times in IPA.

Study of PEDOT:PSS PH1000 films with different post-treatment techniques via IPA in hybrid photovoltaic devices

As a complement to the previous study, the optoelectronic and morphological properties of PEDOT:PSS PH1000 films with different technique treatments via IPA were studied. Consequently, four hybrid solar cells with a p-type layer (PEDOT:PSS PH1000) modified using three different technique treatments via IPA were fabricated. The three technique treatments used and compared in this work are shown in figure 3.15 and which are: a) Vapor treatment, b) Drop technique treatment and, 3) Dip technique treatment.

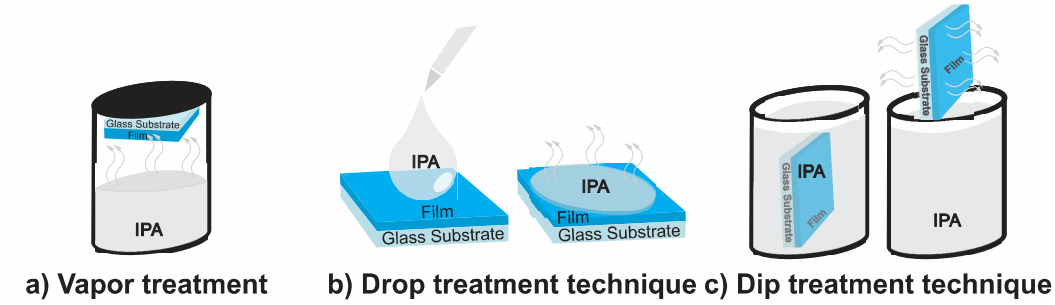

Figure 3.15. Schematic illustration of different post-treatment techniques used in this work.

The vapor treatment (figure 3.15-a) consists of putting the sample in an airtight container to expose the PEDOT:PSS PH1000 film to the IPA steam for 15 minutes. The drop technique treatment (figure 3.15-b) consists of dropping a drop of approximately 500 µl of IPA on the PEDOT:PSS PH1000 film and let stand for 2 minutes, then the excess of IPA is removed. And, the dip technique treatment (figure 3.15-c) consists of completely dipping the PEDOT:PSS PH1000 film in IPA for a certain time, then the excess

of IPA is removed. The nomenclature used to the four different hybrid solar cells mentioned is shown in table 3.14.

Sample	Post-treatment technique
H256	Pristine
H257	Drop of IPA
H258	Immersion in IPA
H259	Vapor of IPA

Table 3.15. Nomenclature for hybrid solar cells with PEDOT:PSS PH1000 treated with different solvent treatments.

3.4.4 STUDY OF SEM MEASUREMENTS FOR ORGANIC FILMS

It is well known the SEM technique is an ultra-high-resolution analytical system that provides outstanding sample preparation and 3D characterization performance for the widest range of samples. However, SEM is a technique that uses the interactions between electron-matter using an electron beam for images in ultra-high-resolution. Due to this, it is complicated to apply the SEM technique on organic materials because they are not good conductors and consequently, they are electrically charged during the measurement process and the organic samples are burned before obtaining a clear image.

In order to obtain SEM images of the organic films studied in this work (PEDOT:PSS PH1000) for morphological analysis, four different configurations were proposed to optimize the measuring process of SEM images of organic materials. The four configurations are shown in figure 3.16.

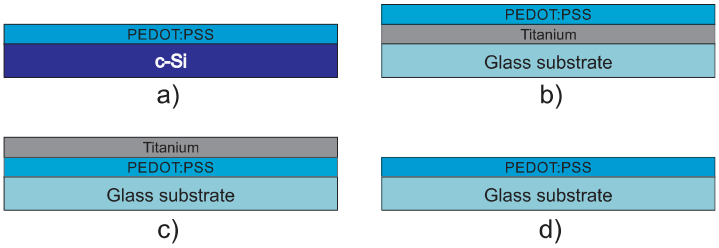

Figure 3.16. Configurations for SEM measurements of organic films

The four different configurations proposed in this work to develop the SEM measurements of organic materials consist in a) PEDOT:PSS PH1000 film deposition on c-Si substrate, b) PEDOT:PSS PH1000 deposition on a 150 nm-Ti film, c) cover the PEDOT:PSS PH1000 with a 25 nm-Ti film and, d) PEDOT:PSS PH1000 film deposition on a glass substrate.

CHAPTER IV

4. EXPERIMENTAL RESULTS

In this chapter, the experimental results about characterization of intrinsic a-Si:H and PEDOT:PSS PH100 films for application in a hybrid heterojunction and the study of its use in hybrid photovoltaics devices are presented. This chapter is focused in a) the description of the fabrication and electronic characterization of the intrinsic a-Si:H films at different deposition pressures, b) the description of solvent post-treatments and c) characterization of PEDOT:PSS PH1000 films. The experimental results of the back interface (i-n) study through the special configuration of electrodes and its effect on device performance are presented. Also, the results on the study of frontal interface (p-i) optimization a) with and without a buffer layer and b) the optical, morphological and electronic modification of PEDOT:PSS PH1000 films, as well as its impact on performance characteristics of hybrid photovoltaics device are shown. Finally, the results of the fabrication and characterization of some complex hybrid structures are presented. It should be mentioned that the results in devices are not presented chronologically, the order in which they are presented is according to their function in the structure.

4.1 RESULTS OF THE FABRICATION AND CHARACTERIZATION OF THIN FILMS FOR HYBRID PHOTOVOLTAIC DEVICES

As mentioned previously, optical and electronic characteristics of a-Si:H films depend on fabrication parameters and there are several different techniques to modify the properties of PEDOT:PSS PH1000 films. For this reason, in this section, the results of the study of the impact of deposition parameters (mainly temperature and pressure) on the properties of intrinsic a-Si:H films deposited by PECVD are presented. On the other hand, the results of the morphological and optoelectronic characterization of PEDOT:PSS PH1000 films pristine and treated by different post-treatmentt techniques using IPA are briefly described.

4.1.1 RESULTS OF THE STUDY OF THE DEPOSITION OF A-SI:H FILMS BY PECVD

Results of the study of different deposition pressure of intrinsic a-Si:H films deposited at 220 °C

As described in subsection 3.4.2, five samples of intrinsic a-Si:H films (about 120 nm) with different deposition pressure from 430 to 830 mTorrs at T_d= 220 °C on glass substrates with stripes were fabricated to measure their dark and AM1.5 conductivities at room temperature. The thickness and dark and AM1.5 conductivities were measured for these five samples according to subsections 3.2.1 and 3.2.2 respectively. The intrinsic a-Si:H films at different deposition pressures were deposited with the following parameters (Table 4.1):

Pressure (mTorrs)	Power (W)	Temperature Display/Substrate	Time (s)	Rate of Flow (SiH_4)
430	3	335°C / 220°C	1500	6 sccm
530	3	335°C / 220°C	1500	6 sccm
630	3	335°C / 220°C	1500	6 sccm
730	3	335°C / 220°C	1500	6 sccm
830	3	335°C / 220°C	1500	6 sccm

Table 4.1. Deposition parameters for intrinsic a-Si:H films at different deposition pressure at T_d= 220 °C.

First, the film thickness was measured to calculate the deposition rate. In table 4.2, the deposition rate of intrinsic a-Si:H films at different deposition pressures at T_d=220 °C is showed. The film thickness and deposition rate can be useful for some characterization methods and fabrication processes.

Pressure (mTorrs)	Thickness (nm)	Deposition rate (Å/s)
430	77	0.51
530	80	0.53
630	83	0.55
730	91	0.60
830	98	0.65

Table 4.2. Thickness and deposition rate of intrinsic a-Si:H films at different deposition pressures at T_d=220 °C.

The I-V curves of all samples at dark and AM1.5 illumination conditions (as described in section 3.2.2) were obtained. Using these curves and the film thickness values, the dark conductivity and photoconductivity were calculated. Observing the figure 4.1-a, it can be seen that the intrinsic a-Si:H films deposited at pressures of 430 and 830 mTorrs present a dark conductivity of 3.3 x 10^{-6} and 2.0 x 10^{-6} S/cm respectively. On the other hand, the a-Si:H films deposited at pressures of 530, 630 and, 730 mTorrs present a dark conductivity of 5.3 x 10^{-9}, 4.5 x 10^{-8} and 3.6 x 10^{-9} S/cm respectively.

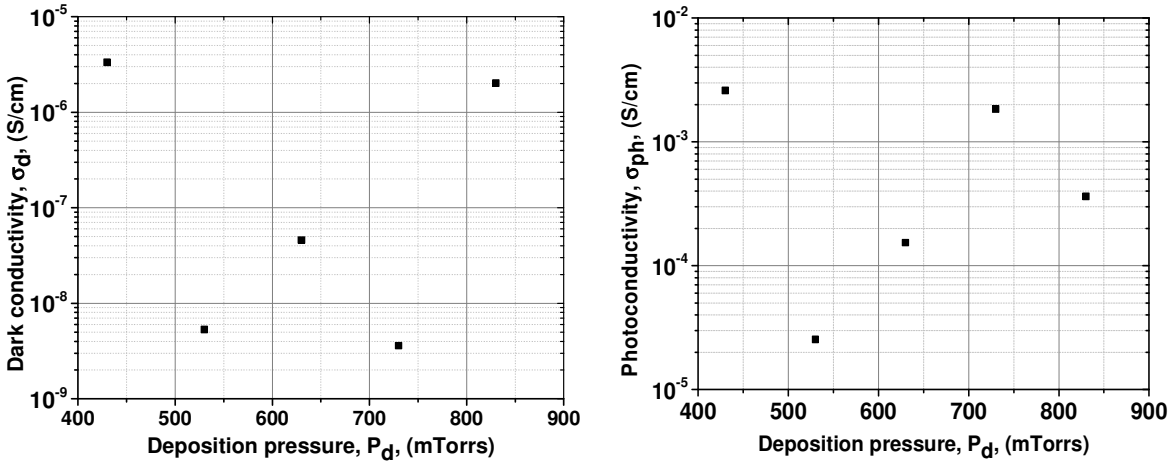

Figure 4.1. Dark conductivity and photoconductivity of intrinsic a-Si:H films deposited at different pressures and at T_d= 220 °C.

In addition, in figure 4.1-b, see that the intrinsic a-Si:H films deposited at pressures of 430 and 730 mTorrs present a photoconductivity of 2.6 x 10^{-3} and 1.8 x 10^{-3} S/cm respectively. On the other hand, the films deposited at pressures of 530, 630 and 830 mTorrs present a photoconductivity of 2.5 x 10^{-5}, 1.5 x 10^{-4} and 3.6 x 10^{-4} S/cm respectively.

Results of the study of different deposition pressure of intrinsic a-Si:H films deposited at 175 °C

Next, five samples of intrinsic a-Si:H films (about 120 nm) deposited at different deposition pressure from 430 to 830 mTorrs at T_d= 175 °C on glass substrates with stripes were fabricated to measure the dark and AM1.5 conductivity at room temperature. Thickness and dark and AM1.5 conductivities were measured for these five samples according to sections 3.2.1 and 3.2.2 respectively. The intrinsic a-Si:H films at different deposition pressures were deposited at the following parameters (Table 4.3):

Pressure (mTorss)	Power (W)	Temperature Display/Substrate	Time (s)	Rate of Flow (SiH_4)
430	3	283°C / 175°C	1800	10 sccm
550	3	265°C / 160°C	1800	10 sccm
630	3	283°C / 175°C	1800	10 sccm
730	3	283°C / 175°C	1800	10 sccm
830	3	283°C / 175°C	1800	10 sccm

Table 4.3. Deposition parameters for intrinsic a-Si:H films at different deposition pressure at T_d=175 °C.

First, we measured the thickness to calculate the deposition rate. The deposition rates of intrinsic a-Si:H films at different deposition pressures are shown in table 4.4.

Pressure (mTorrs)	Thickness (nm)	Deposition rate (Å/s)
430	132	0.73
530	252	0.84
630	137	0.76
730	142	0.79
830	143	0.796

Table 4.4 Thickness and deposition rate of intrinsic a-Si:H films at different deposition pressures at T_d= 175 °C.

As described in section 3.2.2, the I-V curves for all samples under dark and AM1.5 illumination conditions were obtained. Using these curves and the film thickness values, the dark conductivity and photoconductivity were calculated. In the figure 4.2-a, one can see that the intrinsic a-Si:H films deposited at pressures of 550 and 730 mTorrs present a dark conductivity of 5.1 x 10^{-9} and 3.2 x 10^{-9} S/cm respectively. On the other hand, the a-SI:H films deposited at pressures of 430, 630 and 830 mTorrs present a dark conductivity values of 1.4 x 10^{-10}, 2.2 x 10^{-10} and 3.1 x 10^{-10} S/cm respectively.

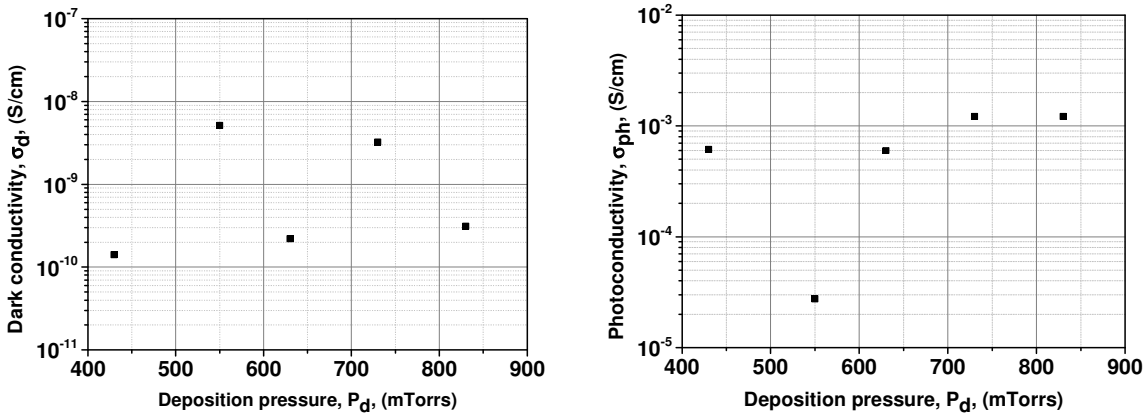

Figure 4.2. Dark conductivity and photoconductivity of intrinsic a-Si:H films deposited at different pressures and at T_d= 175 °C.

Also, in figure 4.2-b one can see that intrinsic a-Si:H films deposited at pressures of 730 and 830 mTorrs present photoconductivity values of 1.2 x 10^{-3} and 1.2 x 10^{-3} S/cm respectively. On the other hand, the films deposited at pressures of 430, 550 and 630 mTorrs present photoconductivity values of 6.1 x 10^{-4}, 2.7 x 10^{-4} and 6.0 x 10^{-4} S/cm respectively.

4.1.2 RESULTS OF SECONDARY DOPING IN PEDOT:PSS FILMS

For the complete study of the a-Si:H/PEDOT:PSS heterojunction, the characterization of the PEDOT:PSS PH1000 films is necessary. As mentioned previously, in this work, different post-treatment techniques to the modification of the optical, electronic and morphological characteristics of PEDOT:PSS PH1000 films were proposed. In this section, the characterization of PEDOT:PSS PH1000 films pristine and treated with all the technique treatments is presented.

Results of the thickness characterization

PEDOT:PSS PH1000 films were fabricated by spin coating using only 250 µL of PEDOT:PSS PH1000 solution at different spin speeds (revolution per minute, RPM) for 30 seconds. Before depositing the PEDOT:PSS PH1000 films on glass or glass/ITO substrates, the substrates were prepared by a cleaning process (as described in section 3.1.2). Once the PEDOT:PSS PH1000 films were deposited, a step was created to measure the difference of level between the film surface and substrate surface by a profilometer (technique mentioned in section 3.2.1). Obtaining the depth profile of the sample relative to the substrate. In figure 4.3, the thickness dependence as a function of the spin speed (RPM) for PEDOT:PSS PH1000 films is presented.

The results show that in a range of spin speed from 400 to 4000 RPM, thicknesses from 40 to 250 nm for PEDOT:PSS PH1000 films can be obtained.

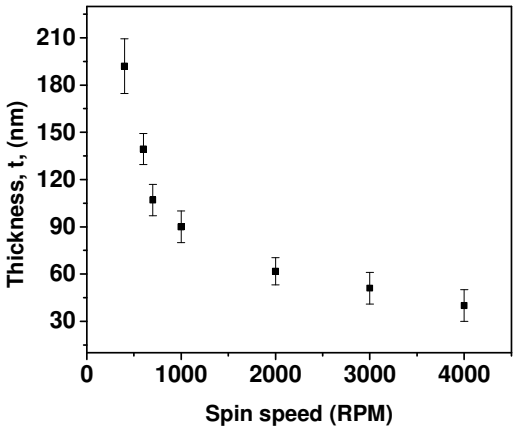

Figure 4.3. Thickness dependence as a function of the spin speed (RPM) for PEDOT:PSS PH1000 films.

One can see that after 3000 RPM the thickness of PEDOT:PSS PH1000 films stay in the range of 40 - 50 nm. The multiple deposition and thickness characterization of these thin films have demonstrated the reproducibility of these results.

Once the thickness characterization of PEDOT:PSS PH1000 films was done, PEDOT:PSS PH1000 films with constant thickness can be fabricated and the films can be treated and characterized. PEDOT:PSS PH1000 films (deposited at 2000 RPM) were post-treated with vapor, drop and dip IPA treatment techniques. It is worth to mention, that the thickness of PEDOT:PSS PH1000 films after any treatment technique did not present significant changes.

Results of the electrical conductivity and work function characterization

PEDOT:PSS PH1000 films (deposited at 2000 RPM) on glass substrates were fabricated to measure the electrical conductivity at room temperature. The electrical conductivity of PEDOT:PSS PH1000 films was measured by the method described in section 3.2.3. First, the electrical conductivity of PEDOT:PSS PH1000 films pristine and treated with a dip in IPA treatment technique at different dipping times from 0 to 45 min (see figure 4.4) were studied. One can see that the PEDOT:PSS PH1000 film pristine presents an electrical conductivity of 0.41 S/cm, which increases to 0.58, 4.83 and 48.5 S/cm with 15 min, 30 min and 45 min of dipping time in IPA respectively.

In the following, the treatment of 45 min of dipping in IPA was used to compare it with other technique treatments. The figure 4.5-a shows the electrical conductivity of PEDOT:PSS PH1000 films pristine and treated via vapor, drop and dip IPA treatment techniques (as described in section 3.4.3).

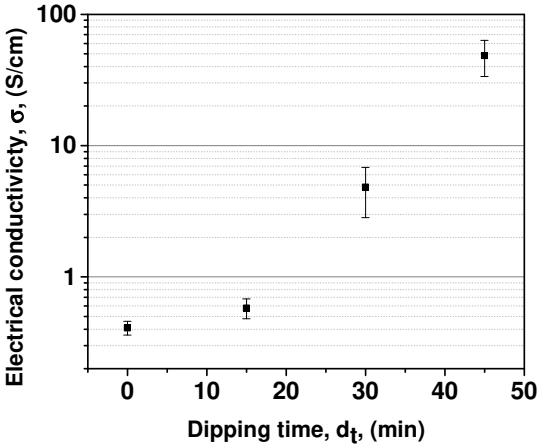

Figure 4.4. The electrical conductivity of PEDOT:PSS PH1000 film pristine and treated with dip in IPA treatment technique at different times.

The PEDOT:PSS PH1000 film pristine presents an electrical conductivity of 0.48 S/cm and it increases to 1.7, 20.7 and 48.5 S/cm with the vapor of IPA, drop of IPA and dip in IPA respectively. PEDOT:PSS PH1000 films with the same parameters on glass/ITO substrates were fabricated to measure the work function.

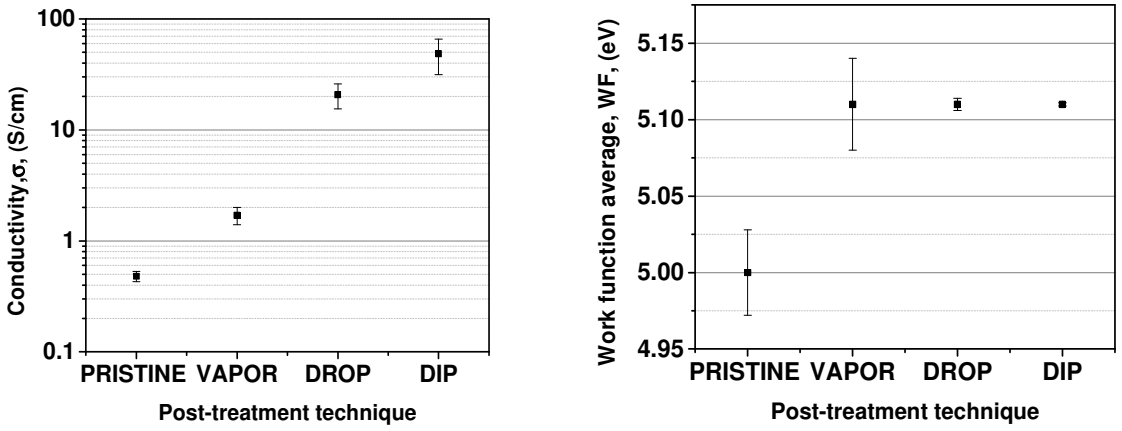

Figure 4.5. a) The electrical conductivity and b) work function of PEDOT:PSS PH1000 films pristine and treated with different treatment techniques using IPA.

The same fabrication process used to the electrical conductivity characterization was used to fabricate PEDOT:PSS PH1000 samples on glass/ITO substrates. The work function of PEDOT:PSS PH1000 films was measured by the method described in section 3.2.3. The results are shown in figure 4.5-b. The

PEDOT:PSS PH1000 film pristine presents a work function of 5.0 eV and the all IPA post-treated PEDOT:PSS PH1000 films present a work function of 5.11 eV.

Results of the optical transmittance characterization

PEDOT:PSS PH1000 films (deposited at 2000 RPM) on glass substrates were used to measure the transmittance spectra. The optical characterization of PEDOT:PSS PH1000 films was done by the method described in section 3.2.4. In figure 4.6, the optical transmittance spectra of PEDOT:PSS PH1000 films pristine and treated with different post-treatment techniques are shown.

The PEDOT:PSS PH1000 film pristine on glass substrate shows a high transmittance with an average value of 85.9 % in the wavelength range from 300 to 750 nm. And, one can see that the PEDOT:PSS PH1000 films dipped during 15, 30 and 45 min in IPA present average value of 85.9, 85.7 and, 85.4 % respectively. Also, one can observe also that the PEDOT:PSS PH1000 film treated with vapor of IPA and drop technique of IPA presented values of transmittance in the same range of 85.2 and 85.4 % respectively.

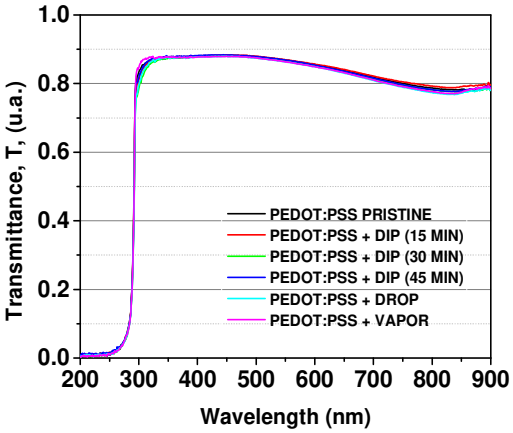

Figure 4.6. The optical spectrum of PEDOT:PSS PH1000 films pristine and treated post-deposition with different techniques treatments using IPA.

Results of the Raman characterization

Moreover, using the same samples for optical transmittance characterization, the Raman spectra were measured. The Raman spectra were obtained as described in section 3.2.5 and in figure 4.7 the Raman spectra results are presented, where one can see some defined peaks at 436, 700, 990, 1256, 1367, 1432, and 1537 cm^{-1}.

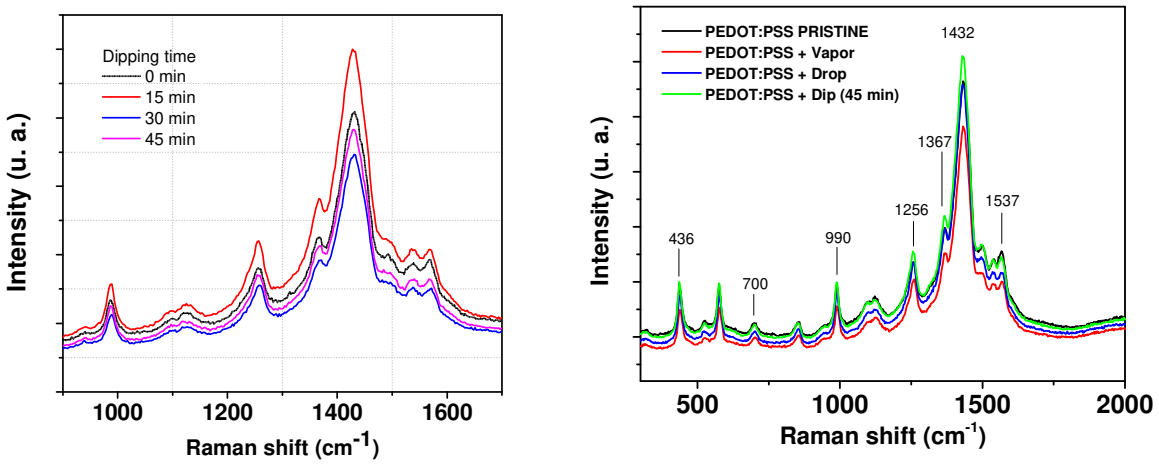

Figure 4.7. Raman spectra of PEDOT:PSS PH1000 films pristine and treated post-deposition a) with dip technique in IPA at different times and b) with different techniques treatments using IPA.

Results of the FTIR characterization

PEDOT:PSS PH1000 films (deposited at 2000 RPM) on c-Si substrates were used to measure the transmittance spectra. The FTIR spectra were obtained as is described in section 3.2.6. In figure 4.8, one can see the typical bands in PEDOT:PSS for the PEDOT:PSS PH1000 films pristine and treated post-deposition, such as 1515, 1292, 1173, 1133, 1073, 1051, 966, 920, 825 and, 685 cm^{-1}. And, also one can identify the band near to 1190, 1003, and 803 cm^{-1}.

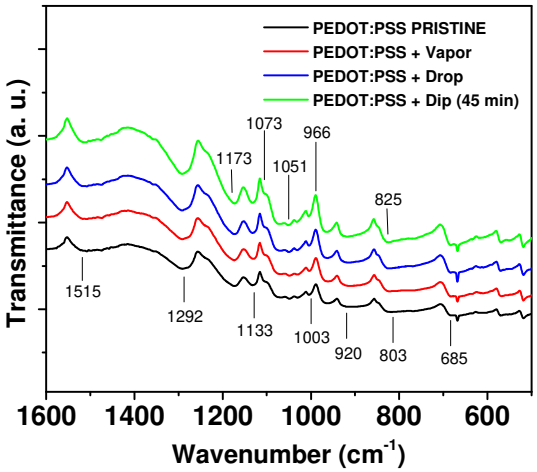

Figure 4.8. FTIR spectra of PEDOT:PSS PH1000 films pristine and treated post-deposition with different techniques treatments using IPA.

Results of the morphological characterization by AFM

Moreover, using the same samples for optical transmittance and Raman characterization, the morphological characteristics (AFM images) were measured. The morphological characterization was done according to section 3.2.7. In figure 4.9 and table 4.5, the AFM images and morphological analysis

of the surfaces of the PEDOT:PSS PH1000 films pristine and treated are presented. The surface of the PEDOT:PSS PH1000 film pristine shows a value of RMS of 1.57 nm, and the PEDOT:PSS PH1000 films post-treated via vapor of IPA, drop technique of IPA and dip technique in IPA present a RMS of 1.80, 1.65, and 1.93 nm respectively. The PEDOT:PSS PH1000 film pristine shows values of skewness and kurtosis of 0.551 and 7.7, and the PEDOT:PSS PH1000 films treated via vapor of IPA, drop technique of IPA and dip technique in IPA present 0.246 and 4.9, 0.004 and 3.3 and 0.056 and 3.2 respectively.

	PEDOT:PSS PH1000			
Treatment	**Pristine**	**Vapor**	**Drop**	**Dip**
RMS Roughness (nm)	1.57	1.80	1.65	1.93
Surface Skewness (Sk)	0.551	0.246	0.004	0.056
Surface Kurtosis (Ku)	7.7	4.9	3.3	3.2

Table 4.5. Morphological characteristics of PEDOT:PSS PH1000 films pristine and treated post-deposition with different technique treatments.

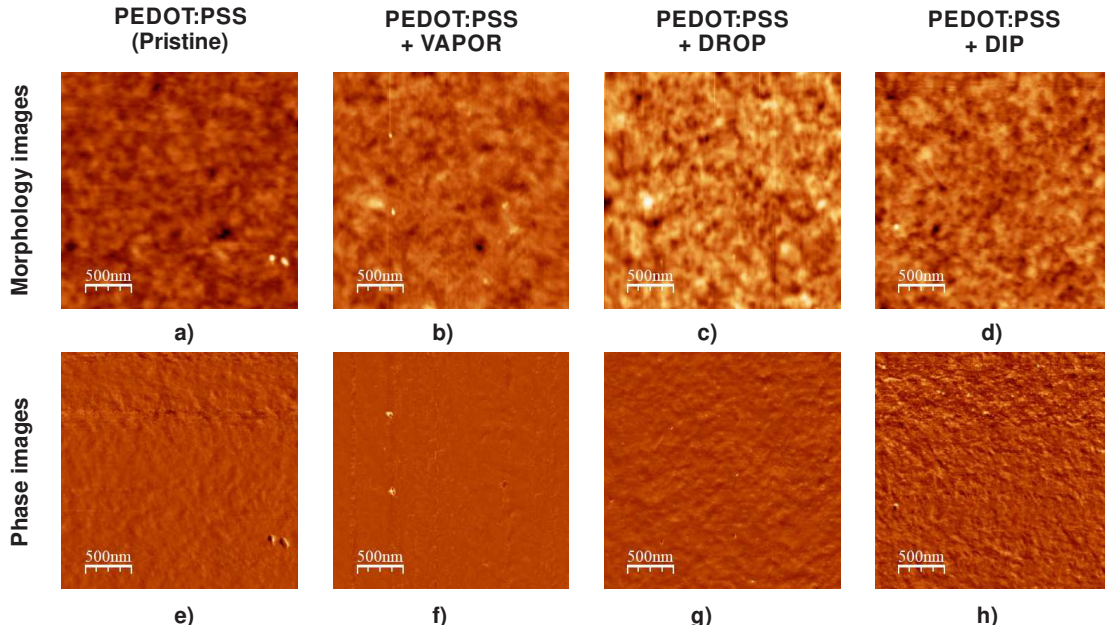

Figure 4.9. AFM (height (a-d) distribution and phase (e-h)) images of PEDOT:PSS PH1000 films pristine and post-treated.

Results of the morphological characterization by SEM

First, PEDOT:PSS PH1000 films were deposited with four different configurations (described in section 3.4.4) to obtain SEM images. In figure 4.10, the SEM images of PEDOT:PSS PH1000 films with the four different configurations previously mentioned are shown.

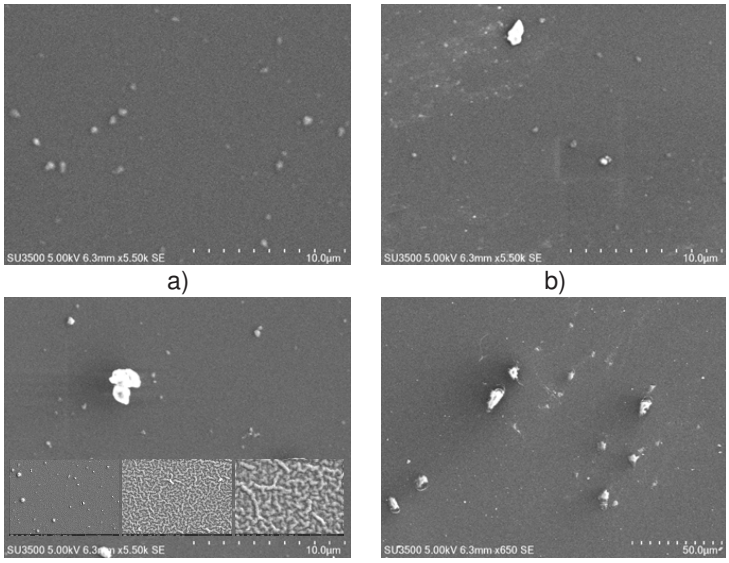

Figure 4.10. SEM images of PEDOT: PSS PH1000 films deposited a) on a c-Si substrate, b) on a Ti film, c) under a Ti film and, d) on a glass substrate.

In figure 4.10, one can see that the low magnification SEM micrographs of the PEDOT: PSS PH1000 films in different configurations are similar. In the configurations a), b) and d), the samples were highly charged and then burned when the magnification was increased to 2000x to get more detailed images. However, with the configuration c) occurred otherwise, the magnification could be increased without the sample being burned and more detailed images (see inserted images in figure 4.10-c) were obtained. In order to optimize the SEM measurements for organic materials, decreasing the Ti film thickness used in the configuration c) and change the Ti film for a gold (Au) film in the next experiment was proposed.

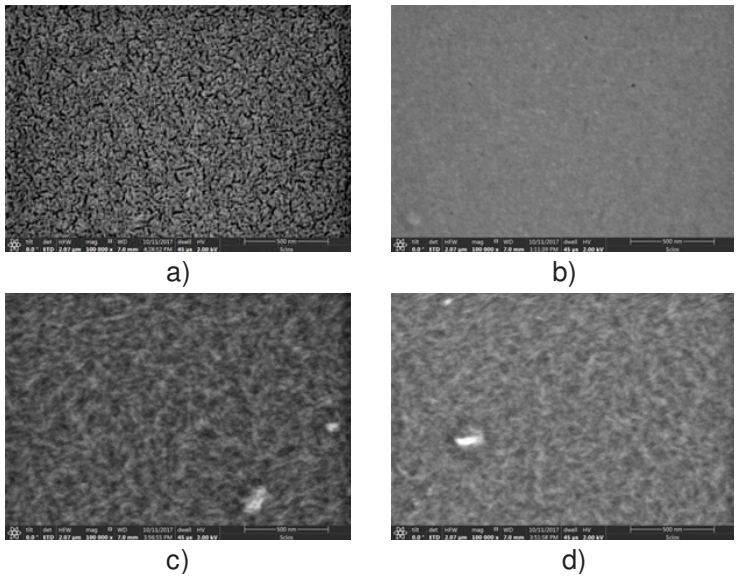

Figure 4.11. SEM images of PEDOT: PSS PH1000 films covered with a) a 4 nm-Au film, b) an 8 nm-Au film, c) a 4 nm-Ti film and d) an 8 nm-Ti film.

The PEDOT:PSS PH1000 films were covered with 4 and 8 nm Ti thin films and 4 and 8 nm gold thin films. In figure 4.11, the SEM images for PEDOT:PSS PH1000 films covered with Ti and Au thin films are shown.

When the PEDOT:PSS PH1000 film was covered with an 8 nm-Au thin film (figures 4.11-b), SEM images with a flattened surface of the PEDOT:PSS PH1000 film is observed. When a 4 nm-Au thin film was used (figure 4.11-a), a high-resolution SEM image with a better contrast is obtained. However, it can be seen that the PEDOT:PSS PH1000 morphology is flattened. On the other hand, when an 8 nm-Ti thin film (see figure 4.11-d) was used, a high-resolution SEM image is obtained, but the contrast is low. Finally, when a 4 nm-Ti thin film was used, the PEDOT:PSS PH1000 morphology can be observed and the image contrast level is high.

Once the methodology for SEM measurements for organic materials has been cleared, PEDOT:PSS PH1000 films pristine and treated with different techniques treatments via IPA were fabricated using the c) configuration. The results are shown in figure 4.12.

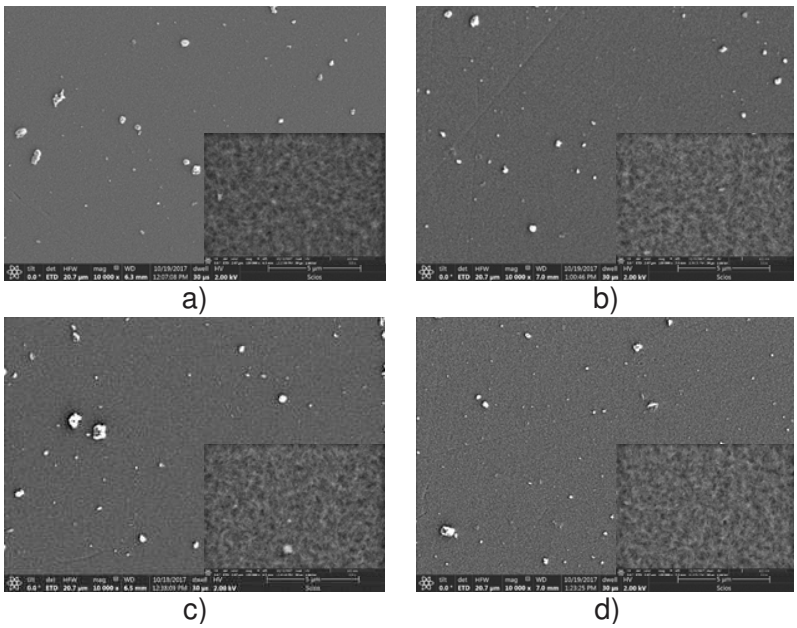

Figure 4.12. SEM images of PEDOT: PSS PH1000 films a) pristine and treated post-deposition with b) vapor of IPA, c) Dip technique of IPA and, d) Dip technique in IPA.

Although the PEDOT:PSS PH1000 morphology can be observed in all samples. Morphological changes dependent on the different techniques treatments via IPA cannot be seen with the simple view.

Once the different properties and the way to modify them have been identified, hybrid photovoltaic devices were fabricated to observe the impact of the modified films on the performance characteristics.

4.2 RESULTS OF FABRICATION AND CHARACTERIZATION OF HYBRID PHOTOVOLTAIC DEVICES

In this section, the results of the fabrication and characterization of hybrid photovoltaic devices based on the a-SI:H/PEDOT:PSS heterojunction are presented. It is important to mention that the results of the hybrid photovoltaic devices presented in this section are arranged according to their function in the structure and they are not presented chronologically. The studies shown in this section were proposed from the final structure (H2) based on the a-SI:H/PEDOT:PSS heterojunction [5] and the final results reported in [101] presented in previous works at National Institute for Astrophysics, Optics and Electronics (INAOE). The results of the hybrid photovoltaic devices presented in this section mainly are divided in three parts: 1) Results about the back interface (interface between intrinsic part and n-type part), 2) Results about the intrinsic part (i) and, 3) Results about the frontal interface (interface between p-type part and intrinsic part).

4.2.1 RESULTS OF THE STUDY OF THE BACK INTERFACE IN HYBRID PHOTOVOLTAIC DEVICES

In this subsection, the results of the study of the back interface i-n (between the intrinsic part and the n-type part) of hybrid photovoltaic devices studied in this work are presented.

Results of the effect of different back electrodes on hybrid photovoltaic devices

About 190 nm of Titanium (Ti) and silver (Ag) layers were used as the back electrode in hybrid photovoltaic devices. So that, hybrid photovoltaic devices with the structure presented in figure 3.1-a were fabricated in accordance with the fabrication process described in section 3.1. These devices were fabricated under the following parameters: glass / ITO (160 nm) / PEDOT:PSS Al 4083 (40 nm) / (i) a-Si:H (320 nm) / (n) a-Si:H (20 nm) / Back electrode. The electrodes were deposited under the following conditions:

Film	Pressure (mTorrs)	Power (W)	Temperature	Flow (Ar)
Titanium	3.8	200	Room	12 sccm
Silver	2	75	Room	10 sccm

Table 4.6. Deposition conditions for back metal electrodes.

In the subsection 3.1.5 of the fabrication process, the back-metal electrode was changed according to the nomenclature shown in the table 3.4.1. For the first sample, a Ti film was deposited as the back electrode, for the second sample, an Ag film was deposited as the back electrode.

Once that fabrication process was ended, the samples were labeled and characterized according to section 3.3. In figure 4.13, the curves J-V for the five samples are shown.

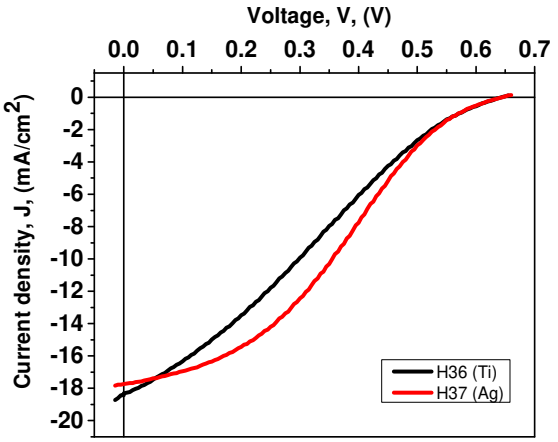

Figure 4.13. J-V curves of hybrid photovoltaic devices with different back metal electrodes.

In figure 4.13, one can see that the J-V curves for the H36 and H37 samples with Ti and Ag films (as the back electrode respectively) present similar performance characteristics. H36 sample presents a short circuit density of J_{sc}= 18.4 mA/cm^2, an open circuit voltage of V_{oc}= 640 mV, a fill factor of FF= 25.6 % and a power conversion efficiency of PCE= 3.0 %. Meanwhile, the H37 sample presents the following parameters: J_{sc}= 17.7 mA/cm^2, V_{oc}= 645 mV, FF= 36.6 % and PCE= 3.7 %. A summary of the results of this study is presented in table 4.7.

Sample	Electrode	J_{sc} (mA/cm^2)	V_{oc} (mV)	FF (%)	PCE (%)	R_s (Ω)	R_{sh} (Ω)
H36	Ti	18.4	640	25.6	3.0	1.1 k	0.7 k
H37	Ag	17.7	645	36.6	3.7	1.2 k	3.0 k

Table 4.7. Performance characteristics for hybrid photovoltaic devices with different back electrodes.

Another study was implemented about an AZO/Ag interface as the back electrode. For this study, hybrid photovoltaic devices were fabricated with the structure presented in figure 3.1-b and according to the fabrication process described in section 3.1. These devices were fabricated under the following parameters: glass / ITO (160 nm) / PEDOT:PSS PH1000 (40 nm) / a-Si:H:C (5 nm) / (i) a-Si:H (320 nm) / (n) a-Si:H (20 nm) / AZO film / Ag (190 nm). The AZO films were deposited with the below conditions:

Film	Pressure (mTorrs)	Power (W)	Temperature	Flow (Ar)
Silver	2	75	Room	10 sccm
Aluminium-doped Zinc Oxide	2	100	150°C	12 sccm

Table 4.8. Deposition conditions for metal electrodes.

In the back-electrode stage of the fabrication process (subsection 3.1.5), the back electrode was changed according to the nomenclature shown in table 3.7. For the first sample, an Ag film was deposited

as the back electrode as a reference sample and for the other samples, AZO films with different thicknesses (see table 4.9) were deposited before the Ag film to form the back electrode.

		Thickness (nm)	
Sample	**Electrode**	**AZO**	**Ag**
H316-A	Ag	0	150
H316-B	AZO/Ag	10	150
H316-C	AZO/Ag	100	150
H316-D	AZO/Ag	250	150

Table 4.9. AZO film thickness for AZO/Ag as the back electrode in hybrid photovoltaic devices.

Once that fabrication process was ended, the samples were labeled and characterized according to section 3.3. In figure 4.14, the curves J-V for four samples are shown.

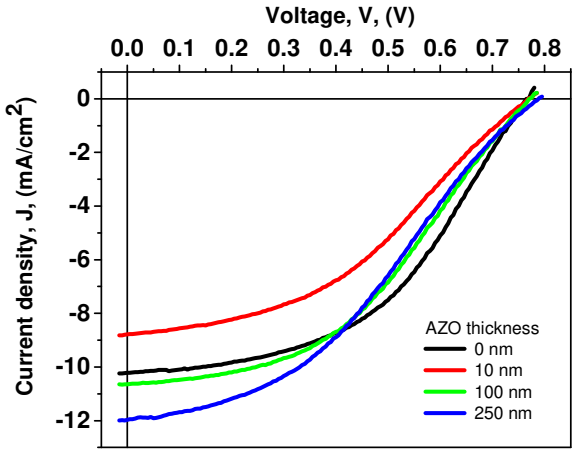

Figure 4.14. J-V curves of hybrid photovoltaic devices with different AZO thicknesses before the Ag film as back electrodes.

In figure 4.14, one can see that the hybrid photovoltaic devices fabricated with an AZO film before the Ag film (H316-B, H316-C, and H316-D samples) as back electrode present a current suppression close to open circuit voltage. Do not exist significant changes (within 20 mV) in the V_{oc} values, with a maximum V_{oc} of V_{oc}= 785 mV (sample H316-D) and with a minimum of V_{oc}= 765 mV (samples H316-A and H316-B). Meanwhile, the sample H316-D shows the maximum J_{sc} value of up to J_{sc}= 11.9 mA/cm^2, and the sample H316-B a minimum J_{sc} value of 8.7 mA/cm^2. In the summary of the results of this study (presented in table 4.10), one can see that although the sample H316-A do not present neither the better J_{sc} nor V_{oc}, this sample shows the best power conversion efficiency of PCE= 3.7 %. Performance characteristics for the best structure are a J_{sc}= 10.2 mA/cm^2, a V_{oc}= 765 mV, and an FF= 48.1 % and PCE=3.7 %.

Sample	Electrode	J_{sc} (mA/cm^2)	V_{oc} (mV)	FF (%)	PCE (%)	R_s (Ω)	R_{sh} (Ω)
H316-A	Ag	10.2	765	48.1	3.7	0.21 K	3.0 K
H316-B	AZO (10 nm)/Ag	8.7	765	41.0	2.7	0.45 K	3.0 K
H316-C	AZO (100 nm)/Ag	10.6	770	43.5	3.5	0.30 K	3.0 K
H316-D	AZO (250 nm)/Ag	11.9	785	38.0	3.5	0.40 K	3.0 K

Table 4.10. Performance characteristics for hybrid photovoltaic devices with different back electrodes

In the following subsections, the results of other interface modifications of the hybrid photovoltaic devices will be presented.

4.2.2 RESULTS OF THE STUDY OF THE DEPOSITION OF THE A-SI:H FILM IN HYBRID PHOTOVOLTAIC DEVICES

In this subsection, the results of the study of the effects of the intrinsic a-Si:H films deposition parameters on the performance characteristics of the hybrid photovoltaic devices are presented.

Different deposition pressures at 220 °C

As described in subsection 3.4.2, hybrid photovoltaic devices with intrinsic a-Si:H films deposited at different pressures and fixed deposition temperature at 220 °C were fabricated. Hybrid photovoltaic devices were fabricated with the structure presented in figure 3.1-a according to the fabrication process described in section 3.1. These devices were fabricated under the following parameters: glass / ITO (160 nm) / PEDOT:PSS PH1000 (40 nm) / Active layer / (n) a-Si:H (20 nm) / Ag (190 nm). In the active layer (inorganic films) stage the intrinsic a-Si:H films were deposited with the conditions below:

Sample	Thickness (nm)	Pressure (mTorrs)	Power (W)	Temperature Display/Substrate	Flow (SiH_4)
H161	327	430	3	335°C / 220°C	6 sccm
H156	328	530	3	335°C / 220°C	6 sccm
H153	328	630	3	335°C / 220°C	6 sccm
H151	328	730	3	335°C / 220°C	6 sccm

Table 4.11. Deposition conditions for intrinsic a-Si:H films

Once that fabrication process was ended, the samples were labeled and characterized according to section 3.3.

In figure 4.15, one can see the J-V curves for the hybrid photovoltaic devices with different intrinsic a-Si:H films deposited at different pressures at T_d= 220 °C. Note, that the H151, H153, and H161 samples present a current suppression close to V_{oc}. The variations of the performance characteristics are following. There is a difference of J_{sc} of up to 1.3 mA/cm^2, with a maximum of 12.8 mA/cm^2 (sample H151) and a minimum of 11.5 mA/cm^2 (sample H156). On the other hand, these devices present a difference in V_{oc} of up to 125 mV, with a maximum of 665 mV (sample H156) and a minimum of 540 mV (sample H161).

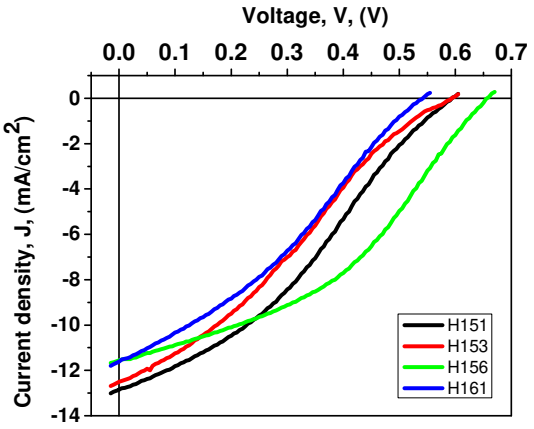

Figure 4.15. J-V curves of hybrid photovoltaic devices with intrinsic a-Si:H films deposited at different pressure at T_d= 220 °C.

The sample H156 presents the best performance characteristics because of the highest FF. The improvement of FF probably comes from lower Rs (up to an order of magnitude) as compared to the other devices. A summary of the performance characteristics of the hybrid photovoltaic devices fabricated in this experiment is presented in the following table (Table 4.12):

Sample	Description	J_{sc} (mA/cm^2)	V_{oc} (mV)	FF (%)	PCE (%)	R_s (Ω)	R_{sh} (Ω)
H161	430 mTorrs	11.6	540	32.4	2.0	0.67 k	1.0 k
H156	530 mTorrs	11.5	665	40.7	3.0	0.45 k	2.1 k
H153	630 mTorrs	12.5	590	28.6	2.1	1.0 k	1.2 k
H151	730 mTorrs	12.8	590	33.7	2.5	0.68 k	1.3 k

Table 4.12. Performance characteristics for hybrid photovoltaic devices with intrinsic a-Si:H films deposited at different deposition pressure at T_d= 220 °C.

Different deposition pressures at 175 °C

As described in section 3.4.2, intrinsic a-Si:H films were deposited at different pressures and at the temperature fixed at 160°C. Hybrid photovoltaic devices were fabricated with the structure presented in figure 3.1-a according to the fabrication process described in section 3.1. These devices were fabricated under the following parameters: glass / ITO (160 nm) / PEDOT:PSS PH1000 (40 nm) / Active layer / (n) a-Si:H (20 nm) / Ag (190 nm). In subsection 3.1.4 the deposition conditions were different. The intrinsic a-Si:H films were deposited under the following conditions:

Sample	Thickness (nm)	Pressure (mTorrs)	Power (W)	Temperature Display/Substrate	Flow (SiH_4)
H190	328	460	3	283°C / 175°C	10 sccm
H182	328	530	3	283°C / 175°C	10 sccm
H197	328	630	3	283°C / 175°C	10 sccm
H200	328	730	3	283°C / 175°C	10 sccm
H188	328	830	3	283°C / 175°C	10 sccm

Table 4.13. Deposition conditions for intrinsic a-Si:H films.

Once that fabrication process ended, the samples were labeled and characterized according to the process described in section 3.3. In figure 4.16, the curves J-V for the four samples are shown.

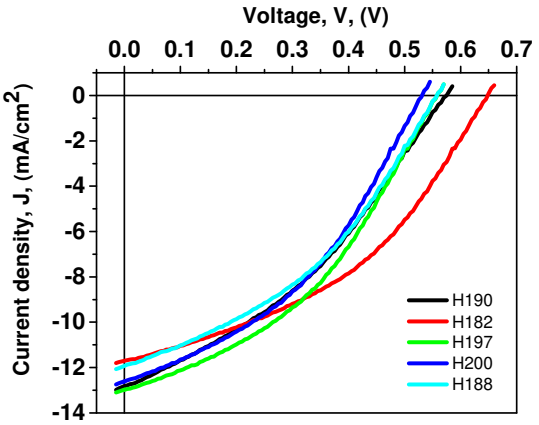

Figure 4.16. J-V curves of hybrid photovoltaic devices with intrinsic a-Si:H films deposited at different pressure at 175 °C.

In figure 4.16, there are no notable changes in their performance characteristics. There is a difference of J_{sc} of up to 1.2 mA/cm^2 with a maximum of 12.9 mA/cm^2 (sample H197) and a minimum of 11.7 mA/cm^2 (sample H182). These devices present a difference of V_{oc} of up to 115 mV with a maximum of 645 mV (sample H182) and a minimum of 530 mV (sample H200). The sample H182 present the highest efficiency because it presents a higher voltage. A summary of the performance characteristics of the hybrid photovoltaic devices fabricated in this experiment is presented in the following table:

Sample	Description	J_{sc} (mA/cm^2)	V_{oc} (mV)	FF (%)	PCE (%)	R_s (Ω)	R_{sh} (Ω)
H190	430 mTorrs	12.8	570	36.2	2.6	0.35 k	1.4 k
H182	530 mTorrs	11.7	645	41.8	3.1	0.33 k	2.1 k
H197	630 mTorrs	12.9	555	40.3	2.9	0.31 k	1.6 k
H200	730 mTorrs	12.6	530	39.6	2.6	0.30 k	1.5 k
H188	830 mTorrs	11.9	555	39.0	2.5	0.33 k	1.5 k

Table 4.14. Performance characteristics for hybrid photovoltaic devices with intrinsic a-Si:H films deposited at different deposition pressure at T_d= 175 °C.

4.2.3 RESULTS OF THE FABRICATION OF THE POLYMER/A-SI:H HETEROJUNCTION IN HYBRID PHOTOVOLTAIC DEVICES

In this subsection, the results obtained during the study of the interface between the p-type part and the intrinsic part (p-i interface) are presented.

Comparison between different organic materials as a p-type layer in hybrid photovoltaic devices

PEDOT:PSS Al4083, PEDOT:PSS PH1000 and P3HT films were used as a p-type layer to fabricate hybrid photovoltaic devices with a p-i-n structure and observe its effect on performance characteristics.

Hybrid photovoltaic devices were fabricated with the structure presented in figure 3.1-a and according to the fabrication process described in section 3.1. These devices were fabricated under the following parameters: glass / ITO (160 nm) / p-type layer / (i) a-Si:H (320 nm) / (n) a-Si:H (20 nm) / Ag (190 nm). PEDOT:PSS Al4083, PEDOT:PSS PH1000 and, P3HT films were deposited as p-type layer according to the following deposition conditions:

Sample	p-type layer	Thickness (nm)
H28	P3HT	~40
H103	Al 4083	~40
H106	PH1000	~40

Table 4.15. Deposition conditions for p-type organic layers.

Once that fabrication process ended, the samples were labeled and characterized according to section 3.3. In figure 4.17, the curves J-V for the three samples are shown.

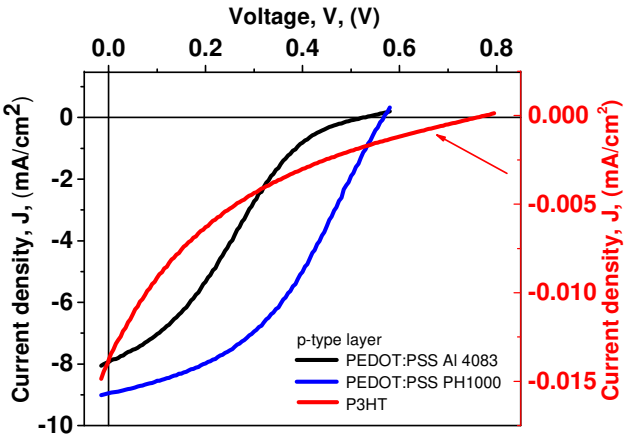

Figure 4.17. J-V curves of hybrid photovoltaic devices with different p-type films.

In figure 4.17, one can note that when the PEDOT:PSS Al4083 was used the J-V curve presents a current suppression while when the PEDOT:PSS PH1000 material was used this current suppression is eliminated. These hybrid photovoltaic devices present similar V_{oc} values: the sample H106 presents a V_{oc} value of 565 mV and the sample H103 of 520 mV. The sample H106 presents a J_{sc} of 8.9 mA/cm^2 and the sample H103 of 7.9 mA/cm^2. The most noticeable difference between these devices was the fill factor, 42.0 % of the FF for the sample H106 and 26.0 % for the sample H103 are obtained. With these values, a power conversion efficiency of 2.1 % for the sample H106 and 1.0 % for the sample H103 are achieved. On the other hand, when the P3HT film was used, the hybrid device presents a high current suppression. The V_{oc} obtained is the highest as 775 mV. However, the J_{sc} is the smallest obtained as 0.01 mA/cm^2. The J_{sc} and the current suppression obtained are translated as small FF and a small PCE (12.5 % and 0.001 % respectively).

A summary of the performance characteristics of the hybrid photovoltaic devices fabricated in this experiment is presented in the table below:

Sample	p-type film	J_{sc} (mA/cm^2)	V_{oc} (mV)	FF (%)	PCE (%)	R_s (Ω)	R_{sh} (Ω)
H28	P3HT	0.01 ± 0.02	775 ± 7	12.5	0.001	2.0 M	192 k
H103	Al4083	7.9 ± 0.6	520 ± 38	26.0	1.0	3.4 k	1.7 k
H106	PH1000	8.9 ± 0.4	565 ± 1	42.0	2.1	0.4 k	1.6 k

Table 4.16. Performance characteristics for hybrid photovoltaic devices with a different p-type layer.

Results of the study of buffer layers in hybrid photovoltaic devices

Four different configurations of hybrid solar cells with a p-i-n structure were fabricated according to the nomenclature described in table 3.4.3 and according to the fabrication process described in section 3.1.

These all structures were fabricated on a glass substrate with the following parameters: ITO film (160 nm) / PEDOT:PSS PH1000 film (40 nm) / (i) a-Si:H (320 nm) / (n) a-Si:H (20 nm) / Ag (190 nm). The specific conditions for each of the four samples are described below:

The sample H206 was fabricated according to the structure showed in figure 3.14-a and with the parameters previously mentioned, this sample is the reference.

The sample H207 was fabricated according to the structure showed in figure 3.14-b. A carbon film (10 nm) between the ITO film and the PEDOT:PSS PH1000 film was deposited via PECVD technique with the following conditions: a pressure of 690 mTorrs, a power of 3 W, a substrate temperature of 160˚C and a flow of methane (CH_4) of 4.5 sccm.

The sample H208 was fabricated according to the structure showed in figure 3.14-c. A carbon graded to silicon film (a-SiC:H) (5 nm) between the PEDOT:PSS PH1000 film and the intrinsic a-Si:H film was deposited via PECVD technique with the following conditions: a pressure of 690 mTorrs, a power of 3 W, a substrate temperature of 160˚C, a constant flow of silane (SiH_4) of 30 sccm, a flow only before the deposit of diborane (B_2H_6) of 3 sccm and an initial flow of methane (CH_4) of 12 sccm (this flow has decrease linearly until reaching the value of 0 at the end of the deposit time).

The sample H209 was fabricated according to the structure showed in figure 3.14-d. A carbon film doped with boron (10 nm) between the ITO film and the PEDOT:PSS PH1000 film was deposited via PECVD technique with the following conditions: a pressure of 690 mTorrs, a power of 3 W, a substrate temperature of 160˚C, a flow of methane (CH_4) of 4.5 sccm and a flow of diborane (B_2H_6) of 0.5 sccm.

Once that fabrication process was ended, the samples were labeled and characterized according to section 3.3. In figure 4.18, the curves J-V for the four samples are shown.

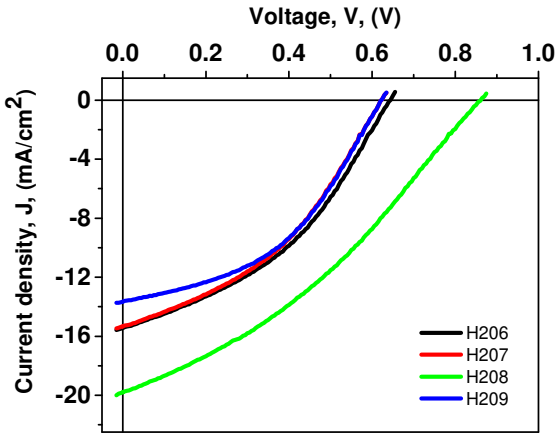

Figure 4.18. J-V curves of hybrid photovoltaic devices with different buffer layers.

In figure 4.18, J-V curves for hybrid photovoltaic devices with different configurations using a buffer layer are shown. One can see that when the devices without a buffer layer (sample H206), using a carbon film (sample H207) or carbon film doped with boron (sample H209) as a buffer layer were fabricated, these devices present similar performance characteristics. The V_{oc} value is from 620 to 640 mV, a J_{sc} from 13.6 to 15.4 mA/cm^2, an FF from 37.5 to 44.0 % and a PCE from 3.7 to 3.9 %. However, when a carbon graded to silicon film (a-SiC:H) as a buffer layer was used (sample H208) between p-type (PEDOT:PSS PH1000) film and a-Si:H film (active layer), the performance characteristics are improved. Presenting a V_{oc} of up to 860 mV, a J_{sc} of 19.8 mA/cm^2, an FF of 34.0 % and a PCE is improved of up to 5.7 %.

A summary of the performance characteristics of the hybrid photovoltaic devices fabricated in this experiment is presented in the below table:

Sample	Buffer layer	J_{sc} (mA/cm^2)	V_{oc} (mV)	FF (%)	PCE (%)	R_s (Ω)	R_{sh} (Ω)
H206	Without	15.4	640	40.0	3.9	0.2 k	1.3 k
H207	Carbon	15.3	620	37.5	3.7	0.2 k	1.6 k
H208	Carbon graded to silicon	19.8	860	34.0	5.7	0.4 k	1.1 k
H209	Carbon doped with boron	13.6	620	44.4	3.7	0.2 k	2.4 k

Table 4.17. Performance characteristics for hybrid photovoltaic devices with different buffer layers.

Results of the study of PEDOT:PSS PH1000 film dipped in IPA in hybrid photovoltaic devices

As described in section 3.4.3, PEDOT:PSS PH1000 films were dipped in IPA at different times to fabricate hybrid photovoltaic devices with a p-i-n structure and observing its effect on performance characteristics. So that what, four hybrid photovoltaic devices were fabricated with the structure presented in the figure 3.1-b and according to the fabrication process described in section 3.1. These devices were fabricated under the following parameters: glass / ITO (160 nm) / p-type layer / (i) a-Si:H

(320 nm) / (n) a-Si:H (20 nm) / Ag (190 nm). PEDOT:PSS PH1000 films were modified according to the deposition conditions following:

Sample	PEDOT:PSS PH1000 thickness (nm)	Dipping time in IPA (min)
H167	~40	0
H168	~40	15
H169	~40	30
H170	~40	45

Table 4.18. Deposition conditions for PEDOT:PSS PH1000 film in hybrid photovoltaic devices.

Once that fabrication process was ended, the samples were labeled and characterized according to section 3.3. In figure 4.19, the curves J-V for the four samples are shown.

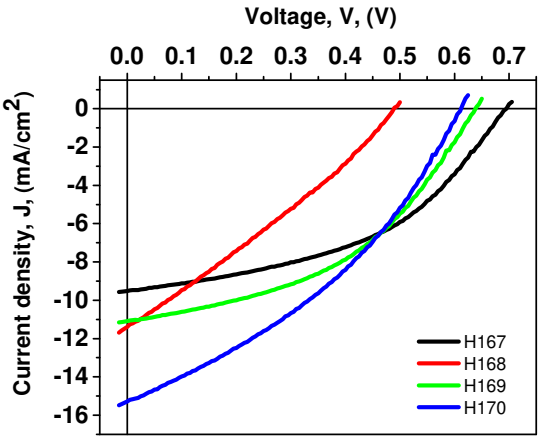

Figure 4.19. J-V curves of hybrid photovoltaic devices with different buffer layers.

In figure 4.19, J-V curves for the hybrid photovoltaic devices with a PEDOT:PSS PH1000 films dipped in IPA at different times are shown. When the device without dipping time of the PEDOT:PSS PH1000 film in IPA (sample H167) was fabricated, a J_{sc} of 9.5 mA/cm^2, a V_{oc} of 690 mV, a FF of 46.0 % and a PCE of 3.0 % are obtained. However, when the PEDOT:PSS PH1000 film was dipped in IPA for 15 min the characteristics parameters decrease as a J_{sc} of 11.3 mA/cm^2, a V_{oc} of 485 mV, a FF of 29.0 % and a PCE of 1.6 %. And, when PEDOT:PSS PH1000 films were dipped in IPA for 30 min and 45 min the characteristics parameters increase as a J_{sc} of 11.6 and 15.2 mA/cm^2, a V_{oc} of 635 and 610 mV, a FF of 31.6 and 3.0 % and a PCE of 3.1 and 3.4 % respectively.

A summary of the performance characteristics of the hybrid photovoltaic devices fabricated in this experiment is presented in the below table:

Sample	Immersion time in IPA (min)	J_{sc} (mA/cm^2)	V_{oc} (mV)	FF (%)	PCE (%)	R_s (Ω)	R_{sh} (Ω)
H167	0	9.5	690	46.0	3.0	0.3 k	3.9 k
H168	15	11.3	485	29.0	1.6	0.3 k	0.6 k
H169	30	11.6	635	31.6	3.1	0.2 k	3.0 k
H170	45	15.2	610	34.0	3.4	0.2 k	1.0 k

Table 4.19. Performance characteristics for hybrid photovoltaic devices with different PEDOT:PSS PH1000 films dipped in IPA at different times.

Results of the study of PEDOT:PSS PH1000 films with different post-treatments techniques via IPA in hybrid photovoltaic devices

On the other hand, as described in section 3.4.3, PEDOT:PSS PH1000 films were treated post-deposition with three different techniques treatments using IPA to fabricate hybrid photovoltaic devices and observing its effect on performance characteristics. Thus, four hybrid photovoltaic devices were fabricated with the structure presented in figure 3.1-b and according to the fabrication process described in section 3.1. These devices were fabricated under the following parameters: glass / ITO (160 nm) / p-type layer / a-SiC:H (5 nm) / (i) a-Si:H (320 nm) / (n) a-Si:H (20 nm) / Ag (190 nm). Deposition parameters of PEDOT:PSS PH1000 films are shown in table 4.20.

Sample	PH1000 thickness (nm)	Post-treatment technique
H256	~40	Pristine
H257	~40	Drop technique of IPA
H258	~40	Dip technique in IPA
H259	~40	Vapor of IPA

Table 4.20. Deposition conditions for PEDOT:PSS PH1000 films pristine and treated with different IPA treatment techniques.

Once that fabrication process was ended, the samples were labeled and characterized according to section 3.3. In figure 4.20, the curves J-V for the four samples are shown.

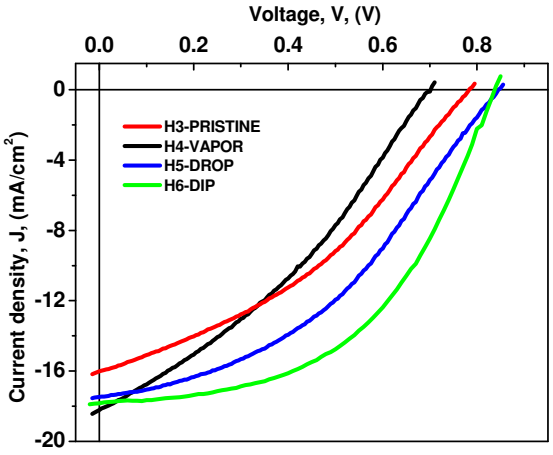

Figure 4.20. J-V curves of hybrid photovoltaic with PEDOT:PSS PH1000 film pristine and treated with IPA different treatment techniques.

In figure 4.20, one can see that when a PEDOT:PSS PH1000 film without post-treatment (sample H256) was used in hybrid photovoltaic devices, a J_{sc} of 16.0 mA/cm^2, a V_{oc} of 780 mV, a FF of 36.9 % and a PCE of 4.6 % are obtained. When the PEDOT:PSS PH1000 film was treated with the vapor of IPA (sample H257), the hybrid photovoltaic device presents a J_{sc} of 18.2 mA/cm^2, a V_{oc} 695 mV, a FF of 34.0 % and a PCE of 4.3 %. When the hybrid photovoltaic device was fabricated with a PEDOT:PSS PH1000 treated with a drop technique of IPA (sample 258), a J_{sc} of 17.4 mA/cm^2, a V_{oc} of 840 mV, a FF of 40.9 % and a PCE of 6.0 % are obtained. Finally, when a PEDOT:PSS PH1000 film was treated with dip technique in IPA for 45 min (sample 259), a J_{sc} of 17.8 mA/cm^2, a V_{oc} of 840 mV, a FF of 50.4 % and a PCE of 7.5 % are obtained. A summary of the performance characteristics of the hybrid photovoltaic devices fabricated in this experiment is presented in the below table:

Sample	Post-treatment technique	J_{sc} (mA/cm^2)	V_{oc} (mV)	FF (%)	PCE (%)	R_s (Ω)	R_{sh} (Ω)
H256	Pristine	16.0	780	36.9	4.6	0.4 k	1.3 k
H257	Vapor of IPA	18.2	695	34.0	4.3	0.3 k	1.0 k
H258	Drop technique of IPA	17.4	840	40.9	6.0	0.4 k	3.0 k
H259	Dip technique in IPA	17.8	840	50.4	7.5	0.2 k	3.0 k

Table 4.21. Performance characteristics for hybrid photovoltaic devices with PEDOT:PSS PH1000 films pristine and treated with IPA different technique treatments.

4.3 RESULTS ABOUT COMPLEX HYBRID PHOTOVOLTAIC STRUCTURES

In the first part of this section, some results to prove the compatibility of the hybrid photovoltaic technology with the flexible plastic substrates (PEN and Kapton) are presented. On the other hand, a-Si:H films used in this work presents an absorption limited to the visible range (from 380 to 750 nm). Therefore, novel materials and structures with specific properties can be applied to improve the so-called simple p-i-n configuration to overcome its weaknesses and absorbing a larger part of the solar irradiance spectrum on Earth. Thus, in the second part of this section, the concept of texturing is introduced in hybrid photovoltaic devices to lengthen the optical path of the light that radiates the solar cell and thus improves the energy collection.

4.3.1 RESULTS OF HYBRID PHOTOVOLTAIC DEVICES ON FLEXIBLE SUBSTRATES

An advantage of a-Si:H films deposition at low temperatures is the compatibility with organic materials and plastics substrates like PEN, “Kapton” and “Teflon”. But there are complex issues in transferring any technology to flexible substrates. Transmittance, mechanical stability, adhesion, changes in the film properties are some of these issues.

Some hybrid photovoltaic devices have been fabricated on PEN and Kapton substrates (figure 4.21-b) to prove the technological compatibility of hybrid solar cells with flexible substrates.

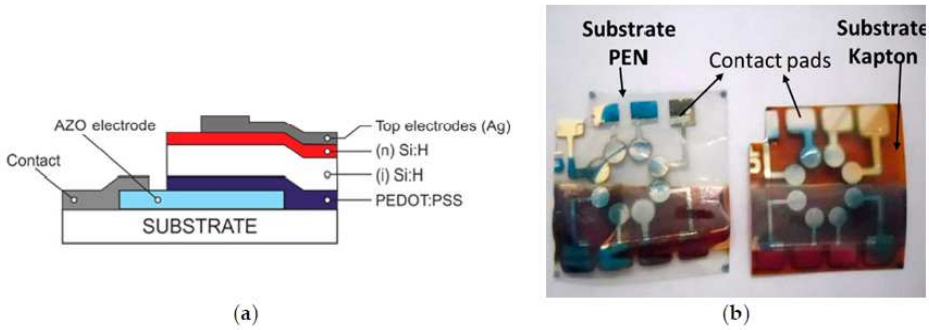

Figure 4.21. a) Hybrid photovoltaic structure based on a-Si:H/PEDOT:PSS heterojunction and (b) photo of the fabricated structures on both polyethylene naphthalate (PEN) and Kapton substrates.

A hybrid photovoltaic device with a structure shown in figure 4.21-a on glass substrate was fabricated as reference according to the fabrication process described in section 3.1. This device from process H41-1 has the following parameters: Glass / AZO(255 nm) / PEDOT:PSS Al4083 (250 nm) / (i) a-Si:H (350 nm) / (n) a-Si:H (20 nm) and Ag electrodes (190 nm). While four hybrid photovoltaic devices are been fabricated on PEN and Kapton flexible substrates. For each substrate type, two hybrid devices have been fabricated: a) PEN / AZO(255 nm) / PEDOT:PSS Al4083 / (i) a-Si:H / (n) a-Si:H / Ag labeled as H42-2, b) PEN/AZO(510 nm) / PEDOT:PSS Al4083 / (i) a-Si:H / (n) a-Si:H / Ag labeled as H43-2, c) Kapton / AZO(255 nm) / PEDOT:PSS Al4083 / (i) a-Si:H / (n) a-Si:H / Ag labeled as H44-2 and, d) Kapton / AZO(510 nm) / PEDOT:PSS Al4083 / (i) a-Si:H / (n) a-Si:H / Ag labeled as H45-2. The film thicknesses of devices fabricated on flexible substrates are the same that in the reference sample except for the AZO film. Once that fabrication process was ended, the samples were labeled and characterized according to section 3.3. In figure 4.22, the curves J-V for the five samples are shown.

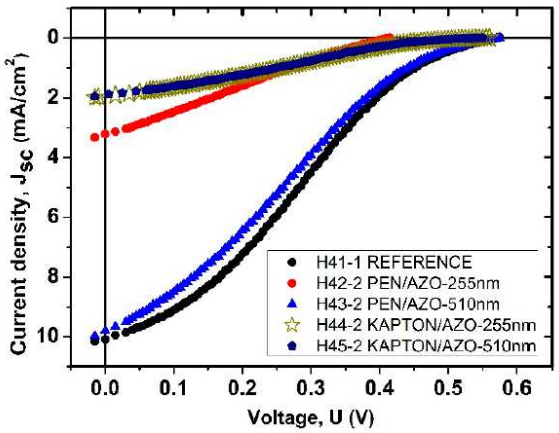

Figure 4.22. J-V curves of hybrid photovoltaic devices fabricated on flexible substrates.

In figure 4.22, it can be seen that J_{sc} of the fabricated devices shows a limitation of current in the range of V= 0.3 – Voc. Therefore, low FF values (from 23 to 26 %) are observed in all structures resulting from

losses of current. All structures have close V_{oc} values from V_{oc}= 550 to 565 mV, except for sample H42-2 with V_{oc}= 405 mV. On the other hand, the reference sample (H41-1) presents the highest current value (10.04 mA/cm^2). And, in the samples deposited on PEN substrates, a dependence of J_{sc} on the thickness of the AZO film is observed. When the thickness of the AZO film is increased two times, the J_{sc} increases from 3.21 to 9.79 mA/cm^2. Also, it can be observed the J_{sc} of samples deposited on Kapton substrates are independent of the thickness of the AZO film with a J_{sc}= 1.9 mA/cm^2. A summary of the performance characteristics of the hybrid photovoltaic devices fabricated in this experiment is presented in the below table:

Sample	Frontal interface	J_{sc} (mA/cm^2)	V_{oc} (mV)	FF (%)	PCE (%)
H41-1	Reference	10.04	565	26.0	1.4
H42-2	PEN / AZO (255 nm)	3.21	405	23.9	0.3
H43-2	PEN / AZO (510 nm)	9.79	565	23.6	1.3
H44-2	Kapton / AZO (255 nm)	1.95	550	23.4	0.2
H45-2	Kapton / AZO (510 nm)	1.90	550	23.0	0.2

Table 4.22. Performance characteristics for hybrid photovoltaic devices on flexible substrates.

On the other hand, in order to observe the structural composition of films on hybrid photovoltaic devices on flexible, a cross-section SEM image of the hybrid photovoltaic structure H44 is presented in figure 4.23.

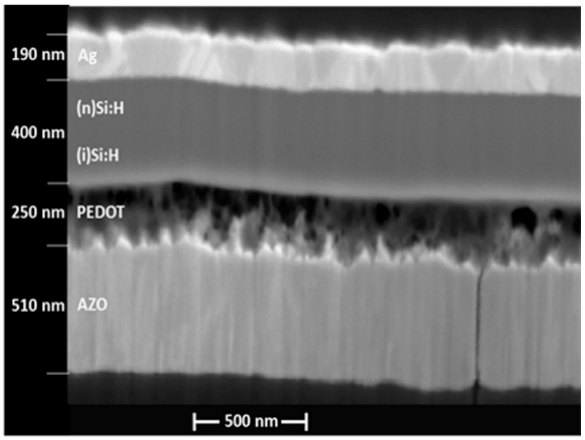

Figure 4.23. A cross-section SEM image of a hybrid photovoltaic device fabricated on a substrate flexible.

In figure 4.23, it is seen that films composing the hybrid photovoltaic device exhibit a rather different structure. AZO layer has a well-defined columnar structure. PEDOT:PSS Al 4083 layer, deposited on AZO is rather inhomogeneous showing spherical inclusions, mainly at the PEDOT:PSS Al 4083/a-Si boundary. And, the Ag layer, demonstrates a well-defined grain structure (with inverted pyramid form).

4.3.2 AZO FILMS TEXTURIZED IN HYBRID PHOTOVOLTAIC DEVICES

The light-trapping properties of textured films have attracted interest because of their potential in reducing the thickness of films that conform to the solar cells. And, therefore, reducing unit costs. As well as reduce bulk recombination, thus raising the open-circuit voltage. This strategy can be applied to any system with limited absorbance. Owing to this, AZO-texturized films are used in a-Si:H-based photovoltaic devices and hybrid photovoltaic devices.

AZO film surface texturization was made using a mixture of deionized water (DI W) and hydrochloric acid (HCl) (at different concentrations) as an etchant solution. Five different concentration of DI W and HCl was studied (shown in table 4.23).

Sample	HCl concentration (%)
1	0
2	0.2
3	0.5
4	0.8
5	1
6	2

Table 4.23. Nomenclature for AZO films texturized with different HCl concentrations in the etchant solution.

AZO-900 nm films were deposited according to section 3.1.5 and after texturized with DI W:HCl etchant solution (at different HCl concentrations) for 30 seconds. The thickness, sheet resistance (see table 4.24) and SEM images (see figure 4.24) were measured after texturized.

Sample	HCl concentration (%)	Thickness (nm)	Sheet resistance (Ω/□)
1	0	900	4.84
2	0.2	780	6.51
3	0.5	638	9.0
4	0.8	561	13.1
5	1	538	13.5
6	2	458	22.7

Table 4.24. The thickness and sheet resistance of AZO films texturized with different concentrations of the DI W and HCl etchant solution.

In table 4.24, it can be seen that AZO thickness and sheet resistance after texturized depend on solution concentration. When the HCl concentration is increased in the etchant solution the thickness decreases from 900 to 458 nm, while the sheet resistance increases from 4.84 to 22.7 Ω/□. In figure 4.24, it can be observed that when the AZO films are etched with DI W:HCl solution small craters are formed. The diameter of these craters depends on the concentration of HCl. One can realize that when an etchant solution with HCl concentration of 2 % is used, craters of more than 1 µm in diameter can be obtained.

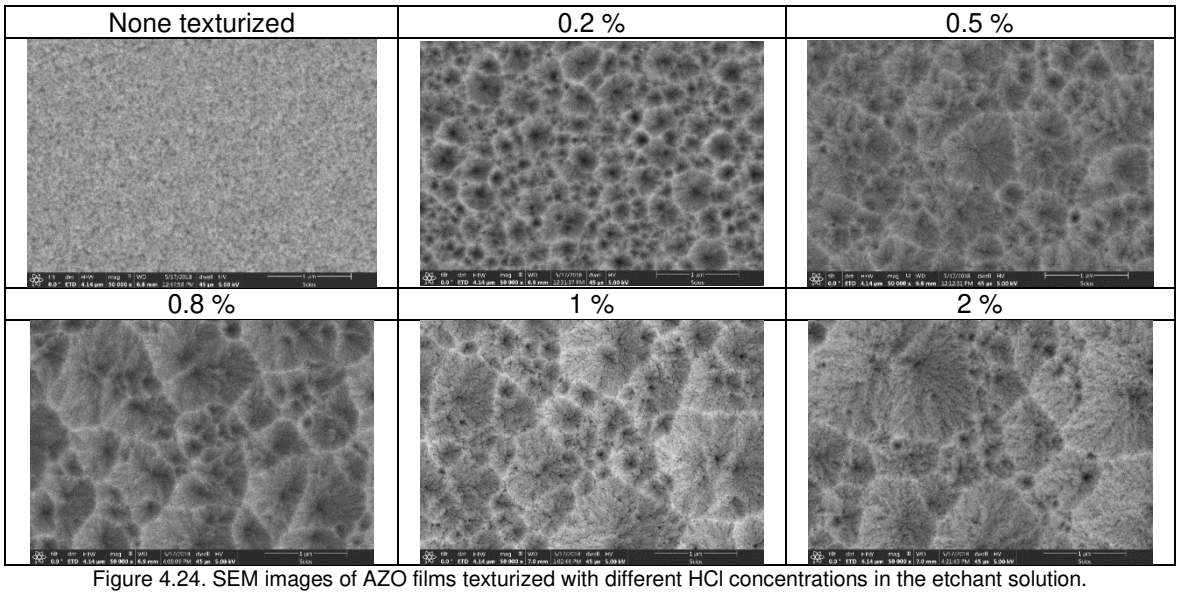

Figure 4.24. SEM images of AZO films texturized with different HCl concentrations in the etchant solution.

Once the AZO films texturized were studied, an AZO film untextured (as reference), an AZO film texturized with an etchant solution with HCl concentration as 0.2, 0.5 and 1 % were chosen to fabricate a-Si:H-based and hybrid photovoltaic devices to observe its effect on performance characteristics.

The devices were fabricated according to the fabrication process described in section 3.1. The a-Si:H-based photovoltaic devices are fabricated with the follow structure: glass / AZO / (p) a-Si:H / a-Si:H:C / (i) a-Si:H / (n) a-Si:H / Ti and the hybrid devices: glass / AZO / PEDOT:PSS PH1000 / a-Si:H:C /(i) a-Si:H / (n) a-Si:H / Ag. The thickness of all AZO films was adjusted to 450 nm after texturized. Once that the fabrication process was ended, the samples were labeled and characterized according to section 3.3. In figure 4.25, the curves J-V for all samples are shown.

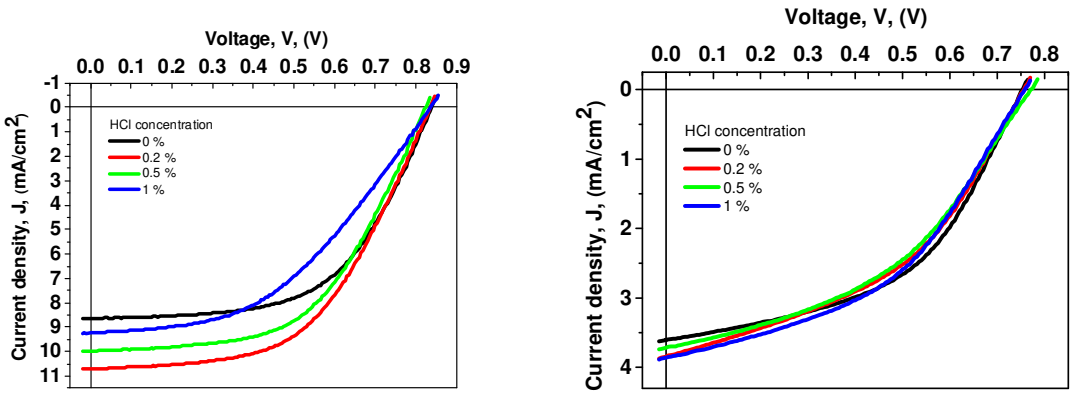

Figure 4.25. Comparison of J-V curves of a) a-Si:H-based and b) hybrid photovoltaic devices fabricated with an AZO film texturized with an etchant solution with different HCl concentrations.

In figure 4.25-a, J-V curves of the a-Si:H-based photovoltaic devices with an AZO film texturized as a frontal electrode are shown. In these curves, one can see that do not exist significant changes (within 15 mV) in the V_{oc} values, with a maximum of V_{oc}= 835 mV and with a minimum of V_{oc}= 820 mV. The sample with texturized with 0.2 % HCl concentration shows the maximum J_{sc} value of up to J_{sc}= 10.7 mA/cm^2, and the sample with 0.5 and 1 % HCl concentration shows a J_{sc} of 9.9 and 9.2 mA/cm^2 respectively. While the sample untextured presents a minimum J_{sc} value of 8.6 mA/cm^2. In the summary of the results of this study (presented in the table 4.25), one can see that the FF depends on HCl concentration (with which the AZO film was texturized), as when the HCl concentration is increased the FF is decreased. The best power conversion efficiency is achieved for the sample texturized with 0.2 % HCl concentration of PCE= 4.7 %. The performance characteristics for the best structure are a J_{sc}= 10.7 mA/cm^2, a V_{oc}= 835 mV, and an FF= 53 % and PCE= 4.7 %. The summary of the performance characteristics of the a-Si:H-based photovoltaic devices with an AZO texturized with different HCl concentrations is presented in the below table:

HCl concentration (%)	J_{sc} (mA/cm^2)	V_{oc} (mV)	FF (%)	PCE (%)
0	8.6	835	57	4.1
0.2	10.7	835	53	4.7
0.5	9.9	820	54	4.4
1	9.2	835	45	3.4

Table 4.25. Performance characteristics for a-Si:H-based photovoltaic devices with an AZO film texturized with different HCl concentrations as the frontal electrode.

In figure 4.25-b, the J-V curves of the hybrid photovoltaic devices with an AZO film texturized as a frontal electrode are shown. In these curves, one can see that do not exist significant changes in J_{sc} and V_{oc} values. The J_{sc} values obtained are in the range from 3.3 to 3.8 mA/cm^2, and the V_{oc} values are in the range from 750 to 770 mA/cm^2.

HCl concentration (%)	J_{sc} (mA/cm^2)	V_{oc} (mV)	FF (%)	PCE (%)
0	3.36	750	53.2	1.3
0.2	3.85	755	43.4	1.2
0.5	3.72	770	43.0	1.2
1	3.86	755	44.7	1.3

Table 4.26. Performance characteristics for hybrid photovoltaic devices with an AZO film texturized with different HCl concentrations as the frontal electrode.

In the summary of the results of this study (presented in the table 4.26) one can see that, the sample untextured presents the best FF value of 53.2 % while the samples texturized with HCl concentrations of 0.2, 0.5 and 1 % present a FF of 43.4, 43.0 and 44.7 % respectively. On the other hand, the PCE of these devices is in the range of 1.2 – 1.3 %.

CHAPTER V

5. DISCUSSION OF RESULTS

In this chapter, the results presented in chapter 4 are analyzed and discussed. Section 5.1 presents the discussion about the studies of the intrinsic (i) a-Si:H and PEDOT:PSS layers as independent films of the PEDOT:PSS/a-Si:H heterojunction. The influence of the deposition pressure and temperature on the photoresponse of the (i) a-Si:H film is discussed. Then, the discussion focuses on the PEDOT:PSS layer and the effects of secondary doping via different post-treatments. In section 5.2, the results about the fabrication of the hybrid structure and different approaches of hybrid heterojunction are discussed. In section 5.3, the results of prelaminar results in complex hybrid devices as hybrid devices on flexible substrates and hybrid devices on AZO texturized as TCO are discussed. Finally, section 5.4 focuses on the detailed development of the PEDOT:PSS/a-Si:H heterojunction and the performance of the hybrid structures fabricated during this thesis work. By comparing our results with other structures reported in the literature, we summarize our findings and discuss the technological potential of the PEDOT:PSS/a-Si:H heterojunction to improve charge collection in hybrid silicon/PEDOT:PSS solar cells.

5.1 STUDY OF INORGANIC (A-SI:H) AND ORGANIC (PEDOT:PSS) LAYERS DEPOSITION

Silicon is the principal and most successful material for device applications in modern solid-state electronics. Moreover, silicon-based devices represent the dominant technologies in the three generations of solar cells: 1st crystalline silicon, 2nd amorphous silicon thin films and 3rd crystalline/amorphous silicon heterojunction (HIT solar cells). In the case of amorphous silicon, its structure, properties, and deposition process have been extensively studied for the last decades (see section 2.1), however, these studies have been focused in old approaches (second generation of PV devices) and are not completed suitable for new and advanced PV structures and technologies. On the other hand, organic semiconductors (see section 2.2) have attracted attention due to their solution-type deposition process that allows the simplification of device fabrication. The conductive polymer PEDOT:PSS has proved to be an innovative material from a new perspective for application in silicon devices [54] but some issues related to compatibility with silicon technology need to be solved. For example, low conductivity and degradation of PEDOT:PSS thin films by the inorganic film deposition processes reduce the performance characteristics comparable to that in pure inorganic devices [5]. Then, the studies discussed in this section are focused on the investigation of the deposition processes of amorphous silicon and PEDOT:PSS thin films to obtain layers suitable for the fabrication of a functional hybrid PEDOT:PSS/a-Si:H heterojunction. It is important to note that the initial conditions of the

deposition process for both, a-Si:H and PEDOT:PSS films, have been taken from the previous works developed at the INAOE, [101] and [5], respectively.

5.1.1 STUDY OF THE DEPOSITION PROCESS OF THE A-SI:H LAYER BY PECVD

The major issues of the construction of complex hybrid structures using organic semiconductors and inorganic materials are the compatibility between their deposition processes. Devices based on organic semiconductors require process under specific conditions to avoid the degradation of the polymers during the fabrication. Following this, in the PECVD process, two conditions should be considered: 1) deposition temperature and 2) ion bombardment. The effect of deposition temperature on the a-Si:H films properties and on the final performance characteristic of the devices can be directly observed by varying this parameter in the deposition process. On the other hand, ion bombardment is a complex process and has interdependence from parameters such as power density, pressure, resident time, gas source, the geometry of the electrode system, etc. [102]. However, the effect of ion bombardment can be indirectly explored by modifying one of these parameters in other conditions fixed. Figure 5.1 shows the deposition rate, r_d, of a-Si:H films deposited in the range of pressure between 430 and 830 mTorrs at different deposition temperatures (T_d= 160, 175 and 200 °C).

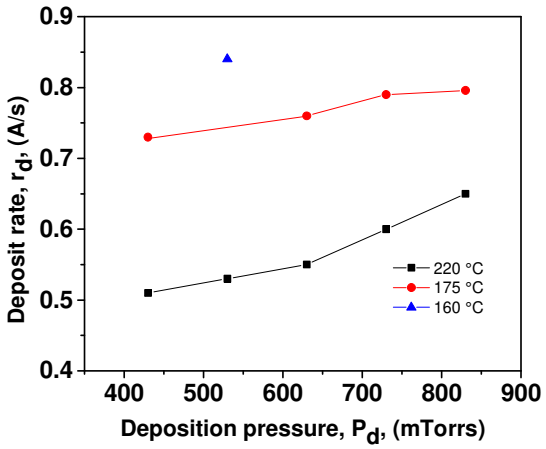

Figure 5.1 Deposition rate for a-Si:H films deposited at different working pressure and deposition temperatures (160 °C, 175 °C and 220 °C).

The effect of pressure on the deposition rate of amorphous silicon has been studied widely in literature [103-104]. At low-pressure regimen, it is expected an increase of deposition rate with an increase of pressure, then a maximal point of deposition rate is found (700 mTorrs [103] and 400 mTorrs [104]), and the deposition rate starts to decrease with the increase of pressure (high-pressure regimen). In comparison with our results, Figure 5.1 shows only an increase of deposition rate with an increase of pressure at temperatures of T_d= 220 and 175 °C, indicating that our experiments are carried out at low-

pressure regimen and the maximum point of the deposition rate has not yet been reached under our deposition conditions. In this low-pressure regimen, the increase of pressure means an increase in the amount of neutral and energetic species in the plasma increasing the number of radicals activated and available for the growth of the films. It is important to note that the increase of these species can also increase the ion bombardment on the surface of the films. Thus, low-pressure regimens are more suitable to avoid degradation of PEDOT:PSS layer in the case that this layer is exposed to plasma during initial deposition of the (i) a-Si:H layer (for example p-i-n configurations). In the PECVD process, the deposition rate is expected to be independent of the deposition temperature [105], this because the species are activated by glow discharge and not by the thermal energy, however, some exceptions have been reported [105-106]. Our results show a decrease in deposition rate with an increase in the deposition temperature (figure 5.1). Similar results are reported in [106], where the deposition rate decreases from r_d = 1.3 to 0.6 A/s with an increase of deposition temperature from T_d = 200 to 320 °C. The reduction of the deposition rate with an increase of T_d in a-Si:H films deposition process via PECVD has not been interpreted. However, the results suggest that under certain conditions, the increase of temperature affects the adhesion coefficient of radicals reducing the deposition rate.

Figure 5.2 shows the photoresponse of the a-Si:H films deposited at different pressures and temperatures. The values of photoresponse (σ_{ph}/σ_d) have been obtained from the dark and photoconductivity results presented in chapter 4. Photoresponse has been selected in this work as a general diagnostic property of the film quality, from the PV point of view, higher photoresponse leads to better collection efficiency due to lower recombination rate [107].

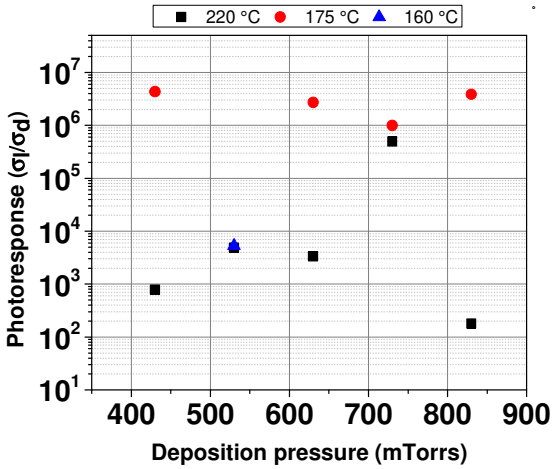

Figure 5.2. Photoresponse (σ_{ph}/σ_d) for a-Si:H films deposited by PECVD at different pressures at a) 220 °C, b) 175 °C.

In figure 5.2, the photoresponse of a-Si:H films deposited by PECVD in the pressure range from 430 to 830 mTorrs at T_d= 220°C are shown (black color). It is observed that a photoresponse of 10^5 is obtained

at a pressure of 730 mTorrs, while for a-Si:H films deposited at pressures of 430, 530, 630 and 830 mTorrs, the value is between the range of 10^2 and 10^3 mTorrs. On the other hand, the photoresponse of a-Si:H films deposited in the range of pressure from 430 to 830 mTorrs but at the deposited temperature of T_d= 175 °C is shown in figure 5.2 (red color). The photoresponse remains almost constant (~10^6). A lower value of photoresponse (10^3) is obtained at a pressure of 550 mTorrs and T_d= 160 °C (blue color). The photoresponse values of a-Si:H films deposited at T_d= 220 °C are reported to be between the range from 10^3 to 10^5 with a small decrease when the deposition pressure is increased [20-21]. This is because at high pressure, the gas-phase polymerization reactions increase in the glow discharge, which results in deterioration of the film quality. Also, it has been reported that the photoresponse decreases with the increase of deposition temperature [16-18]. This is because the total hydrogen content decreases with an increase of the deposition temperature, producing films with more defects. It is known that the typical range of the deposition temperature to obtain device quality a-Si:H films by PECVD technique is around 200 °C and 250 °C and it has been reported that the photoresponse of a-Si:H films need to reach values of at least 10^5 to be applied in quality devices [10]. Based on the photoresponse values obtained in this work and reported in the literature, the a-Si:H films deposited at a pressure of 730 mTorrs (T_d= 220 °C) and all a-Si:H films deposited at 175 °C are the most recommended for device applications. However, only the lower deposition temperatures (T_d < 200 °C) allow to fabricate photovoltaic devices on low-cost substrates (PEN or PET) and to achieve compatibility with organic semiconductors for fabrication of hybrid photovoltaic devices [108-109]. In section 5.2.2, the performance characteristics of hybrid devices using the deposited (i) a-Si:H layer are presented for discussion.

5.1.2 STUDY OF THE DEPOSITION AND SECONDARY DOPING OF THE PEDOT:PSS LAYER

In this section, the results on the PEDOT:PSS films presented in the section 4.1.2 are discussed. Figure 5.3 shows the results obtained of thickness as a function of the spin speed for PEDOT:PSS. The standard theory for the spin coating deposition presented in section 3.2 predicts that thickness is inversely proportional to spin speed. For the PEDOT:PSS film, the experimental data was fitted to the equation 3.2 (line red in figure 5.3), in which the correlation coefficient (CC) and the alpha (α) value are 0.97 and -0.60, respectively. It has been reported that values of α from -0.50 to -0.63 for polymer solutions correspond to viscosities between 15 and 90 mPas s [110], this is in good agreement with the viscosity of PEDOT:PSS films (~ 30 mPa s) provided by its distributor. Also, it is reported that PEDOT:PSS films deposited in the spin speed range from 1000 to 6000 RPM results in thickness values from 40 to 100 nm [111]. On the other hand, PEDOT:PSS films deposited in the range from 500 to 3500 RPM results in thicknesses between 40 and 174 nm [28, 112]. In comparison with literature, it is observed that the thickness values obtained in this work agree with those reported in the literature.

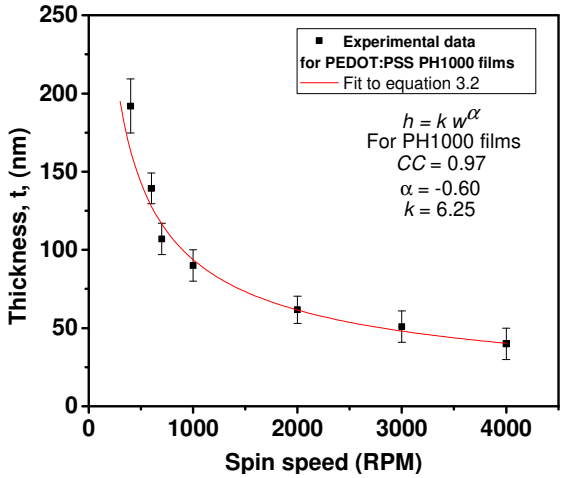

Figure 5.3. The fit of experimental data for the thickness characterization of PEDOT:PSS PH1000 films.

As it was mentioned in chapter 2, several methods have been proposed to enhance the electrical and morphological properties of PEDOT:PSS films to control and improve their characteristics for different applications. For example, different treatment techniques in PEDOT:PSS layers are used to enhance their conductivity to apply them in organic electronic devices such as OLEDs, OPV's, and OFET's [30, 33]. In [70], PEDOT:PSS (Clevois P) films have been mixed with IPA solvent previous deposition and it has been used as an electron transport layer (ETL) in organic solar cells [70]. In this work, we propose different post-treatment techniques to study and control the conductivity of PEDOT:PSS films (section 3.4.3). In the case of the dip technique (figure 3.15), the conductivity of IPA post-treated PEDOT:PSS films show an increase with the increase in the dipping time from 0.41 S/cm (pristine) to 48.5 S/cm (45 min) (figure 4.4). On the other hand, figure 4.5-a shows the conductivity of PEDOT:PSS films pristine and treated via vapor, drop and dip (45 min) techniques. An increase in the conductivity is observed according to the aggressivity of the treatment from the pristine film (σ=0.48 S/cm), vapor (σ=1.7 S/cm), drop (σ=20.7 S/cm), and dip (σ=48.5 S/cm) technique treatment. It is important to note that these changes in conductivity (two orders of magnitude) are similar to those obtained in the doping of inorganic semiconductors. It is well known that the conductivity of PEDOT:PSS films is enhanced via organic solvent doping due to a change in the PEDOT:PSS structure, mostly due to an increase in the interchains of PEDOT-rich domains and a structural change of PEDOT chains from coil conformation to linear/expanded-coil conformation [113]. It has been reported that the PSS distribution and PEDOT/PSS ratio have a direct impact on the charges transport for the conductive polymer [114-115]. Also, IPA treatment removes PSS and affects the Coulomb interaction between PEDOT and PSS chains, modifying the PEDOT and PSS distributions in the bulk and surface improving the average conductivity of the film. In this case of the dip technique, this allows deeper penetration of IPA (that increase with time) to modify PSS chains into the bulk compared to that in the vapor or drop technique treatments that mainly affect the surface [114-115].

Figure 4.5-b shows the work function values of PEDOT:PSS films pristine and treated. The work function values of the PEDOT:PSS films increase for all the post-treated films (~5.11 eV) in comparison to that (~5.0 eV) in the pristine film. In literature, work function values of PEDOT:PSS films pristine are reported to be between the values of 4.9 – 5.0 eV [61, 116]. It is understood that mechanisms that determine the PEDOT:PSS work function are usually complex, and these can be affected by PEDOT/PSS ratio, preparation and/or ambient exposure [55]. However, the results presented in this work suggest that the changes in work function in PEDOT:PSS films treated can be attributed to changes in the surface caused by segregation of PSS chains from the bulk. In table 5.1 a summary of the conductivity and work function of PEDOT:PSS films pristine and treated with different techniques is presented.

	PEDOT:PSS PH1000			
	Pristine	**Vapor**	**Drop**	**Dip**
Conductivity (S/cm)	0.48	1.7	20.7	48.5
Work function (eV)	4.97 – 5.02	5.08 – 5.14	5.01 – 5.11	5.11

Table 5.1. A summary of the electrical properties of PEDOT:PSS PH1000 films pristine and treated with different technique treatments.

It is observed that a change in the conductivity leads to a change in the work function. This can be explained by various factors; however, we assume that the same process responsible for changes in the bulk conductivity affects the surface changing the work function. To confirm this, morphological analysis of the surface of the PEDOT:PSS films pristine and treated with different techniques were performed (figure 5.4 and table 4.5).

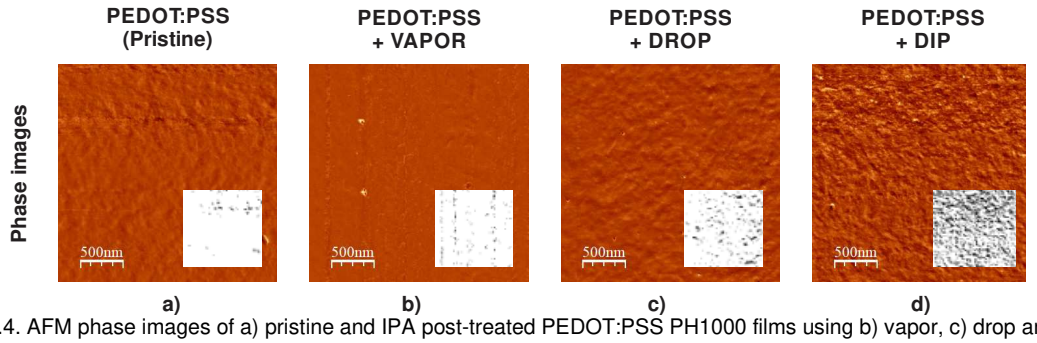

Figure 5.4. AFM phase images of a) pristine and IPA post-treated PEDOT:PSS PH1000 films using b) vapor, c) drop and d) dip techniques and high phase images (insert images).

The surface of PEDOT:PSS film pristine shows the lowest value of roughness of R_q = 1.57 nm, while in the treated film has a maximum value of R_q = 1.93 nm. The increase of surface roughness in the post-treated PEDOT:PSS films is attributed to the redistribution of the PSS and PEDOT chains [51, 117]. Figure 5.4 shows the AFM phase images and their high-contrast version for the different PEDOT:PSS films. A smooth image of the surface is obtained for the pristine sample and the degree of phase-contrast

increases with the increase of IPA post-treatment aggressivity from the vapor to the dip technique. Accumulation of PSS on the surface is clearly observed in the high-contrast images as the increase of negative/dark regions (PSS-rich domains), which explains the increase of the work function and the increase of conductivity in the PEDOT:PSS films treated, as a consequence of a self-organized nanostructure process [137]. The PSS-enrichment of the surface results in an accumulation of PEDOT chains in the bulk, improving channels of charge transport and increasing the conductivity. These results confirm our hypothesis that the same process responsible for the change in the conductivity lead changes in the work function of the films.

Additionally, the analysis of the surface through Kurtosis (K_u) and Skewness (S_k) parameters was carried out proving relevant information about morphology characteristics (see table 4.5). Kurtosis revels whether the morphology of the surface is dominated by sharp ($k_u > 3$) or bumpy ($k_u < 3$) shapes, while skewness describes whether the morphology is pore ($S_k < 0$) or peak ($S_k > 0$) shape [118]. Based on this, it is observed that the morphology for all samples is dominated by sharper peaks. However, sharpness and peak shapes are reduced by the post-deposition treatments, and surface morphology reaches more regularity ($S_k \sim 0$ and $K_u \sim 0$) from the drop and dip treatment techniques. Uniformity of the morphology of the surface of PEDOT:PSS films could play an important role in the formation of the frontal interface during the deposition of subsequent layers. Figure 4.6 presents the optical transmittance spectra of PEDOT:PSS films pristine and treated with different techniques. The glass/PEDOT:PSS pristine system shows a transmittance with an average value about of Tavg= 85% in the wavelength range from 300 to 750 nm. It is observed that does not exist a remarkable change in the transmittance between the pristine and the post-treated PEDOT:PSS films. This agrees with studies reported in literature where the addition of common solvents does not significantly affect the optical properties of the films [13].

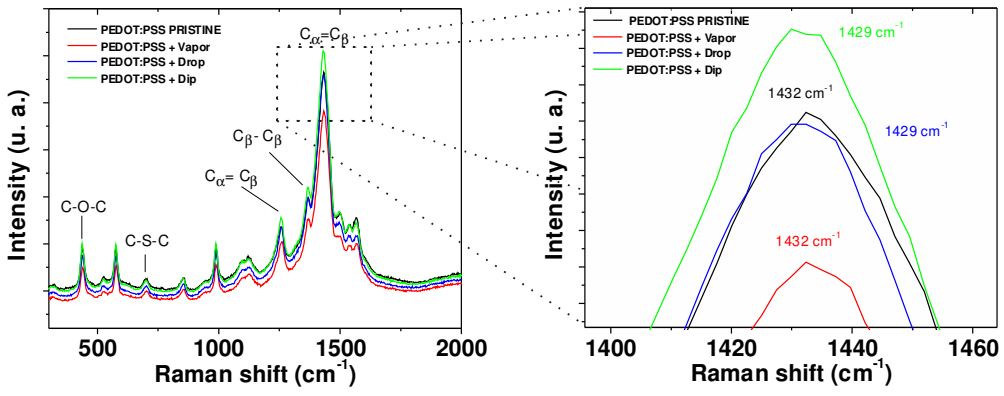

a) b)

Figure 5.5 a) Raman spectra of pristine and IPA post-treated PEDOT:PSS PH1000 films using vapor, drop, and dip techniques and b) Close view of Raman band associated to C=C symmetrical stretching intramolecular vibration of PEDOT between 1400 and 1460 cm^{-1}.

To better understand the changes in the post-treated PEDOT:PSS films, Raman and FTIR spectroscopies were performed and the results analyzed. In figure 5.5-a, the Raman spectroscopy of PEDOT:PSS films pristine and treated are shown.

The main peaks of the chain conformation bands for PEDOT were detected in the Raman spectra as follows: C-O-C deformation at 436 cm^{-1}, symmetric C-S-C deformation at 700 cm^{-1}, oxyethylene ring deformation at 990 cm^{-1}, and Cα-Cα inter-ring stretching at 1256 cm^{-1} [119-120]. The band near 1367 cm^{-1} represents the Cβ-Cβ stretching mode, the asymmetrical stretching vibrations are near 1537 cm^{-1}, Cα=Cβ symmetric stretching vibrations are near 1434 cm^{-1}, and finally, the Cα=Cβ symmetric stretching vibrations of the five-membered thiophene ring on PEDOT occur between 1400 and 1500 cm^{-1} [121-122]. PEDOT has two types of structures: a) the structures in base state (Benzoid) and b) the structure in a doped state (Quinod), which are shown in figure 5.6 and several Raman studies in PEDOT conclude that narrowing of the C=C stretching vibration peaks is evidence of a change of the resonance of the PEDOT chains from benzoid to a quinoid form [119-122]. Figure 5.5-b shows the close view of Raman shift between 1400 and 1460 cm^{-1} to analyze the position of the Cα=Cβ symmetric stretching band near 1434 cm^{-1} for the PEDOT:PSS films treated with different treatment techniques. As expected, the Cα=Cβ symmetric stretching vibration shows a small shift of its band position from 1432 cm^{-1} (pristine and vapor technique) to 1429 cm^{-1} (drop and dip techniques), meaning a change in the structure conformation from coil (benzoid) to expanded-coil/linear (quinoid) conformation [114]. The quinoid conformation for the PEDOT:PSS films treated enhance the conductivity increasing the charge carrier mobility as a result of a rearrangement of PEDOT and PSS chains; this rearrangement is also promoted by the enrichment of PSS on the surface.

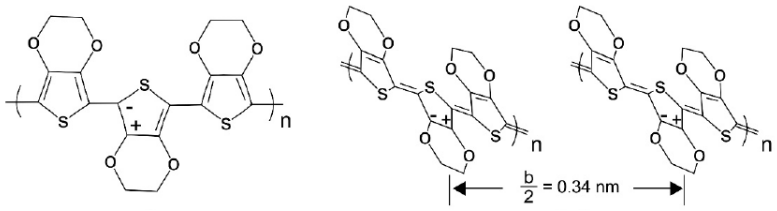

Figure 5.6 Chemical structures of the a) benzoid and b) quinoid forms of PEDOT.

In Figure 5.7 the chemical structure and the presence of the functional groups in the FTIR spectrum of PEDOT:PSS were identified. The bands near 1515 and 1292 cm^{-1} are assigned to the C=C asymmetric stretching mode and C–C inter-ring stretching mode, respectively. The C–O–C bending vibrations in the ethylenedioxy group occur at 1173, 1133, and 1051 cm^{-1}, while C–S–C stretching vibrations in the thiophene ring occur at 966, 920, 825, and 685 cm^{-1}. The 1190 and 1003 cm^{-1} bands are assigned to the S=O and O–S–O symmetric stretching modes in PSS, respectively.

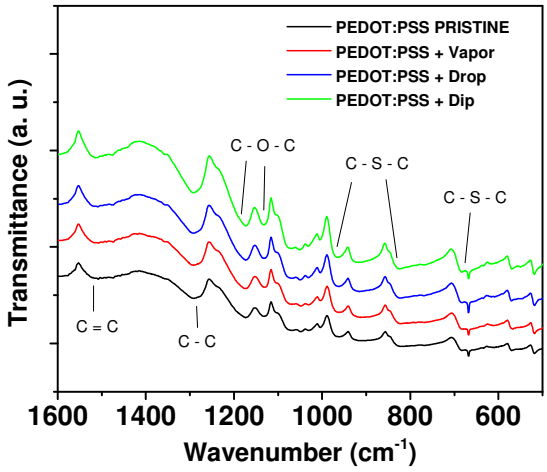

Figure 5.7 Fourier-transform infrared spectroscopy (FTIR) spectra of PEDOT:PSS PH1000 films pristine and treated with different technique treatments.

Finally, the C–H angular deformation of the aromatic ring in PSS gives a band at 803 cm^{-1} [119, 121, 123]. The clear presence of these bands means that the deposition and the post-deposition treatments with IPA were carried out without degradation of the polymer. Also, the bands in the spectra of the post-treated films show a minimum displacement in the pristine sample, which confirms the chemical stability of the films after the treatments. The polymerization degree of PEDOT can be evaluated from the ratio of integration of the IR bands at 852 and 685 cm^{-1}, a lower intensity ratio means a higher degree of polymerization [119]. There is not a clear trend related to the post-deposition treatments, it can be observed that the PEDOT:PSS film treated with drop technique presents the highest polymerization degree. However, we assume that the small changes of polymerization degree between the films pristine and treated can be related to the variability of the deposition process of the films rather than the treatment techniques with IPA.

5.2 STUDY OF THE HYBRID HETEROJUNCTION IN PHOTOVOLTAIC DEVICE FABRICATION

In the previous section, the PEDOT:PSS and the active a-Si:H layers were separately studied. In this section, the complete fabrication of a structure based on the hybrid PEDOT:PSS/a-SI:H heterojunction is discussed.

5.2.1 STUDY OF THE BACK INTERFACE FABRICATION IN THE HYBRID PHOTOVOLTAIC DEVICES

Back electrodes are also used as back reflectors to improve the haze and scatter properties promoting the light dispersion and enhancing the absorption of long-wavelength light in the absorber layer. However, some technological issues are presented, for example, metal atoms tend to diffuse to a-Si:H

films forming silicide, which limits the device performance [124]. In this work, two metals (Ti and Ag) were studied for the formation of the back-metal electrode in the hybrid photovoltaic structure (figure 3.1-a). Also, a study of an AZO/Ag system as the back electrode was performed. Figure 4.13 and Table 4.7 show the performance characteristics of the hybrid photovoltaic devices using Ti and Ag layers as back electrodes. It is expected that the Ag electrode presents a higher reflectance and therefore higher J_{sc} than that in structure with Ti electrode, however, both devices (sample H36 with a Ti film and sample H37 with an Ag film) present small difference in J_{sc} and V_{oc} (0.7 mA/cm^2 and 5 mV, respectively). This result can be attributed to different factors, for example, parasitic leakages, related to electrodes or the general structure, which can suppress current and hide the effects of higher reflectance in the Ag electrode. On the other hand, the H37-Ag device has a higher FF than that in the H36-Ti device. This is a result of an increase of R_{sh} by one order of magnitude in comparison to that in the H36-Ti device. The difference of R_{sh} between structures is difficult to interpret, since, it involves several factors as diffusion coefficient of the metals, defects in the a-Si:H layers [125], deposition temperature, and deposition technique of the metals. It is interesting to note that both, the H37-Ag and the H36-Ti structures, have similar R_s despite the differences in conductivities of the metals used as electrodes. This means that there is a dominant R_s caused by other elements in the structure that share both structures.

Figure 5.8 shows the J_{sc}, V_{oc} and FF values of hybrid photovoltaic devices with Ag and AZO/Ag interfaces as a back electrode. A small increase of V_{oc} and a small decrease of FF with the increase of the AZO layer (thickness) from 0 to 250 nm is observed.

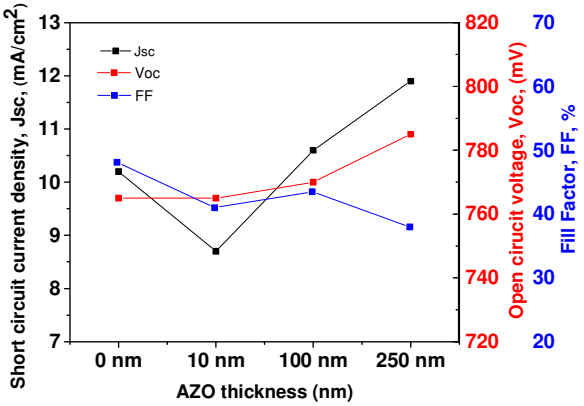

Figure 5.8. J_{sc}, V_{oc} and FF values of hybrid photovoltaic devices with an AZO/Ag interface as a back electrode.

These results can be attributed to a potential barrier caused by the difference of the WF between Ag (4.7 eV) and AZO (4.89 eV) [118]. The increase in the AZO layer increases the effectivity of this barrier increasing the Voc. However, the increase of the AZO layer also results in an increase of Rs caused by the resistance of the TCO and this reduces the FF. In contrast, the J_{sc} decreases with the addition of

the non-optimized 10-nm layer and then increases with the increases of the layer thickness. In literature [126-127] is mentioned that reflectivity due to the difference between the refractive index of the AZO layer and a metal electrode improves absorption in the long-wavelength region 600 – 800 nm. However, the results show that the use of an AZO/metal electrode system requires a compromise between the thickness of the TCO and its resistivity.

5.2.2 GLOW DISCHARGE DEPOSITION OF A-SI:H FILMS COMPATIBLE WITH POLYMERS

One of the main issues of hybrid technologies is to achieve compatibility between fabrication processes. In the case of the hybrid polymer – (a-SI:H) PECVD technology, it is widely believed that exposure of the polymer to the glow discharge causes degradation of the polymers manly generated by deposition temperature and ion bombardment [55]. However, this belief is only based on the low-performance characteristics of non-optimized hybrid structures and it has not been systematically studied or proved. In contrast, our hypothesis based in previous results [5], is that compatibility of polymers with PECVD processes can be achieved via optimization of the deposition parameters of the glow discharge and optimization of the polymers / inorganic interface. In section 5.1.1, it was discussed the a-Si:H deposition in the function of pressure at different temperatures. In figures 4.15 - 4.16 and tables 4.12 and 4.14, the J-V curves and performance characteristics of the hybrid photovoltaic devices with the intrinsic a-Si:H films deposited in that study are shown. To facilitate the comparison and discussion of the results obtained, the performance characteristics were plotted as a function of the deposition pressure in Figure 5.9.

In the case of the a-Si:H films deposited at 175 °C, figures 5.9-a-b shows a decrease of J_{sc} and V_{oc} in hybrid devices with active films deposited at higher deposition pressure but do not present notable changes in the FF and PCE. In the case of the a-Si:H films deposited at 220 °C, J_{sc} and V_{oc} increase with the increase of pressure, while the FF and PCE values do not present a trend as a function of deposition pressure, however, the maximum values are obtained at a pressure of 600 mTorrs. In general, the better performance characteristics are obtained in the devices deposited at 175 °C, except for V_{oc} values. This can be attributed to two reasons: 1) The a-Si:H intrinsic films deposited at 175 °C have a better photoresponse (see figure 5.2) and 2) the deposition temperature of 220 °C is very close to the temperature limit in which the organic film used begins to reduce [13, 28].

it should be noted that the maximum values of performance characteristics were obtained in the pressure range from 500 - 600 mTorrs and the best characteristics were presented in the device fabricated at 500 mTorrs and T_d =160 °C. The discussion in section 5.1.1 suggests that deposition processes at this pressure range present less ion bombardment in comparison to that at high-pressure regimes.

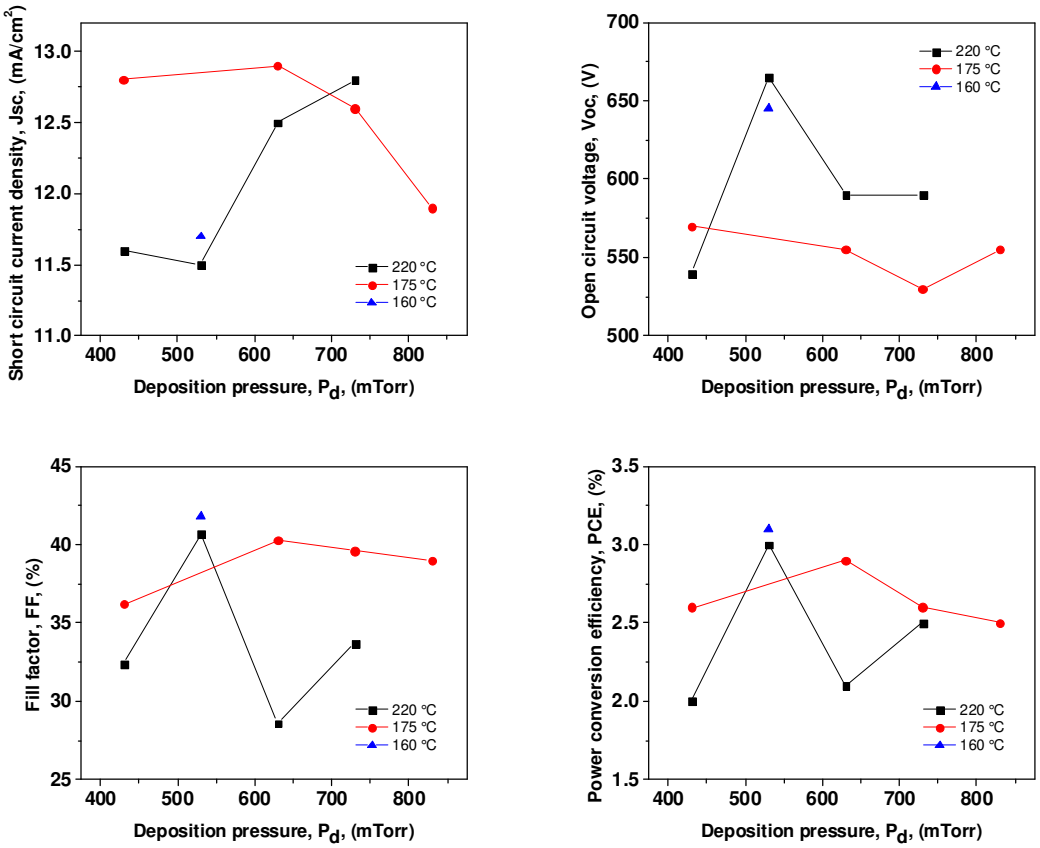

Figure 5.9. a) J_{sc}, b) V_{oc}, c) FF and, d) PCE of hybrid photovoltaic devices as a function of the deposition pressure at T_d =160, 175 and, 220 °C.

The results obtained in this section support our hypothesis that the PECVD process can be adjusted to be used under conditions compatible with polymer with two main characteristics: 1) regimens of low temperature (T_d < 200°C) and 2) low ion bombardment.

5.2.3 STUDY OF HYBRID POLYMER/A-SI:H HETEROJUNCTION IN THE FRONTAL INTERFACE

In this section is discussed the fabrication polymer/a-Si:H heterojunction in the hybrid structure shown in figure 3.1-a. Figure 4.17 and table 4.16 present the comparison between the J-V curves for hybrid photovoltaic structures with different p-type layers: P3HT polymer semiconductor, PEDOT:PSS Al4083 and PH1000 pristine layers. It can be observed that the devices with PEDOT:PSS Al4083 and P3HT layers show current suppression. This can be attributed to the low conductivity of the P3HT layer (10^{-6} S/cm) and PEDOT:PSS Al4083 pristine film (10^{-3} S/cm), which affects the optimal transport of the charge carriers to the frontal electrode [55-128]. In the case of the device with the P3HT layer, the J_{sc} is too low and this may be caused by the degradation of the P3HT layer that is exposed to the glow discharge during the deposition of the a-Si film [129]. However, it is interesting to note that this structure presents

the highest V_{oc} between the compared structures. This can be a consequence of the larger bandgap of P3HT (1.9 eV) in comparison to that of PEDOT:PSS (1.6 eV) [128]. This result shows a potential application of P3HT as p-type layer in hybrid structures, however, further studies need to be realized to optimize the interface and prove that it is possible to increase J_{sc}.

In contrast, hybrid structures using the frontal PEDOT:PSS/a-SI:H heterojunction show better performance (PCE = 1 - 2 %) in comparison to that in the structure with the P3HT/a-Si:H heterojunction (PCE= 0.001 %). The main difference between the structures using PEDOT:PSS is the shape of the curve. It is observed that the structure using the PEDOT:PSS PH1000 has better FF and there is not current suppression. On the other hand, the structure with PEDOT:PSS Al4083 layer has high R_s and R_{sh} values. The absence of current suppression in the structure with the PEDOT:PSS PH1000 layer is associated with the correct alignment of energy levels of the materials and their junctions. The higher conductivity (10^{-1}-10^{0} S/cm) and work function (4.9-5.0 eV) of the PEDOT:PSS PH1000 layer in comparison to that in the PEDOT:PSS Al4083 layer, improve the alignment of the bands increasing the collection of the charge carriers in the frontal electrode. These results show that the control of properties as work function and conductivity in PEDOT:PSS layer can be a key factor to optimize the PEDOT:PSS/a-SI:H heterojunction. For this, we have selected the PEDOT:PSS PH1000 layer to be used in the following structures and we have performed the study of secondary doping of the PEDOT:PSS PH1000 layer to enhance the performance characteristic in hybrid photovoltaic devices.

As was proved in section 5.1.2, secondary doping is a suitable technique to modify conductivity and work function of the PEDOT:PSS layers. Figure 4.19 and table 4.19 shows the result in performance characteristics of the structure with IPA post-treated PEDOT:PSS layer in the PEDOT:PSS/a-Si:H heterojunction configuration. For this study, the dip treatment technique has been used and the principal result is a consistent increase of J_{sc} from 9.5 mA/cm^2 to 15 mA/cm^2 with an increase of dipping time from 0 to 45 min resulting in the highest PCE (3.4 %) for the longest dipping time. This demonstrates that secondary doping in PEDOT:PSS layers can be used to optimize the hybrid PEDOT:PSS/a-Si:H heterojunction in photovoltaic devices. To reach this goal, further studies have been realized and presented in the following sections.

5.2.4 STUDY OF PEDOT:PSS/BUFFER/A-SI:H HETEROJUNCTION IN THE FRONTAL INTERFACE

The approach of using buffer layers to improve transition in the interfaces of solar cells has been poorly reported in the literature [130]. However, this concept is widely used to solve some technical issues in devices. Previous works at INAOE report the development of an a-SiC:H/a-Si:H buffer layer to be used in the frontal interface of inorganic p-i-n configurations improving the performance characteristics [101].

Other works report the use of C:H layers as anti-diffusion (AD) layer improving the spectral response of devices in short wavelength region (< 400 nm) [101]. Also, SiO:H(B) layers have been used in order to reduce the barrier for holes and create a barrier for electrons to minimize back diffused electrons at the frontal interface, improving both V_{oc} and J_{sc} [109]. In this section, we discuss the fabrication and performance characteristics of a different configuration of hybrid structures using buffer layers. The objective of this study is to analyzes some technological issues in the follow frontal interface configurations: i) TCO / PEDOT:PSS / a-Si:H, ii) TCO / C:H / PEDOT:PSS/a-SI:H, iii) TCO / $SI_{0.3}C_{0.7}$:H(B) / PEDOT:PSS/a-SI:H and iv) TCO / PEDOT:PSS / $(Si_{1-X}C_X:H)_{graded}$ /a-SI:H. Figure 4.18 and table 4.17 show the J-V curves and the performance characteristics of these structures, respectively. It is noted that when a carbon film, ii) configuration, or a doped carbon film, iii) configuration, is added between the TCO and the PEDOT:PSS layer, the devices present a small reduction in performance characteristics in comparison to that in the reference sample (i). These reductions can be attributed to a potential barrier for holes in the interface between carbon-based layers and the conductive polymer. Carbon layers in conventional inorganic a-Si:H-based solar cells have the function to prevent diffusion of oxygen and impurities from the TCO to the a-Si:H layers. However, in the case of the proposed hybrid configuration in this thesis work, the PEDOT:PSS layer also acts as antidifusión layer between the ITO and active a-Si:H layer, then the use of the C:H layer is not required and its use is not an optimal approach as the result shown.

On the other hand, It is important to note the improvement in the performance characteristics of the iv) configuration using a $(Si_{1-X}C_X:H)_{graded}$ layer. It is observed that the addition of a $(Si_{1-X}C_X:H)_{graded}$ layer results in an increase of V_{oc} from 640 mV to 860 mV and J_{sc} from 15.43 mA/cm^2 to 19.8 mA/cm^2 compared to that in the i) configuration without the buffer layer. The hypothetical energetic diagram for electrons in the thermal equilibrium of the iv) configuration is presented in figure 5.10 as a guide for discussion. The values of work functions, optical gaps, electron affinities and detailed information used for the construction of this diagram are discussed in the work [5]**.**

In pure a-Si:H cells, it is well known that a-SiC:H:B buffer layers are used as a p-type layer in the frontal interface to increase the "built-in" electric field and transparency of the p-type layer [131]. In the case of the hybrid configurations, it is observed to have the same effect. The similarity between the optical gaps of amorphous silicon (E_g ~ 1.7 eV) and PEDOT:PSS (E_g ~ 1.6 eV) results in lower V_{oc} ~ 640 mV, in contrast with that in the i) configuration with the $(Si_{1-X}C_X:H)_{graded}$ layer. It is important to note that the use of an intrinsic $(Si_{1-X}C_X:H)_{graded}$ layer in the frontal interface of a hybrid configuration improves the open-circuit voltage to 840 mV, which is very close to that in pure a-Si:H configuration with V_{oc} = 895 mV.

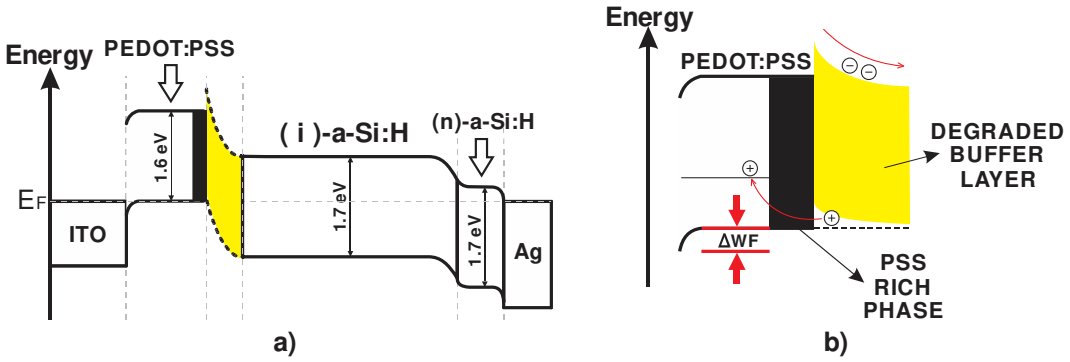

Figure 5.10 (a) Energy level band diagram in thermal equilibrium for a hybrid structure and (b) schematic representation of the electron-blocking mechanism with the buffer layer (a-SiC:H/a-Si:H) by interfacial wide energy gap.

Thus, the improvement in V_{oc} can be explained as consequence of the creation of a potential barrier in the conduction band at the PEDOT: PSS/ $Si_{1-x}C_x$: H)$_{graded}$ /a-Si:H interface improving the built-in potential and a reduction of the electron diffusion into the PEDOT:PSS film (see figure 5.10).

Effect of secondary doping of PEDOT:PSS in the hybrid PEDOT:PSS/buffer/a-Si:H heterojunction

In the sections 5.1.2 and 5.3.2 have been discussed the effect of secondary doping in PEDOT:PSS layer and the prelaminar results in hybrid structures (PEDOT:PSS/a-SI:H heterojunction), respectively. In this section, we focus on applying the methods developed of secondary doping (vapor, drop and dip techniques) for optimization of hybrid structures with frontal PEDOT:PSS/buffer ($Si_{1-x}C_x$:H)$_{graded}$)/a-Si:H heterojunction. For this, hybrid p-i-n structures with PEDOT:PSS films pristine and post-treated were fabricated. Figure 4.20 and table 4.21 show the J(V) characteristics of the p-i-n structures labeled as H256-PRISTINE, H257-VAPOR, H258-DROP, and H259-DIP structures. The H256-PRISTINE reference structure exhibits J-V characteristics as V_{oc} = 780 mV, J_{sc} = 16 mA/cm^2, FF = 36.9 % and a PCE = 4.6 %. The lowest open-circuit voltage of V_{oc} = 695 mV was obtained in the H257-VAPOR structure; characterization of the vapor-treated PEDOT:PSS film (section 5.1.2) demonstrated that the effect of the vapor technique on the electronic and morphological characteristics is weak and limited to the surface. Moreover, the nature of the vapor treatment technique may produce nonuniform changes in the surface. This can be confirmed by the variability in work function values (5.08 to 5.14 eV) obtained for the vapor post-treated film characterization (figure 4.5-b) and can explain the low V_{oc} in the H257-VAPOR structure. In contrast, the H258-DROP and H259-DIP structures present higher open-circuit voltages than that in the H256-PRISTINE structure.

In the previous section, it was demonstrated that drop and dip post-treated PEDOT:PSS films were modified by IPA forming an enriched-PEDOT bulk with preferential quinoid conformation and an

enriched-PSS surface (Figure 5.10-b). This arrangement in the internal nanostructure of PEDOT:PSS films can improve the electron-blocking process and hole collection. This characteristic can also be enhanced by the increase of work function in the post-treated PEDOT:PSS layer due to IPA treatments, explaining the improvement of V_{oc} and J_{sc} in the H258-DROP and H259-DIP structures. It is also observed that the changes of conformation from benzoid to quinoid in PEDOT improve charge transport and conductivity reducing serial resistance in the hybrid structures. This effect is enhanced by the aggressivity of the dipping technique and is clearly observed in the H259-DIP structure that presents the lowest serial resistance. Also, all fabricated hybrid structures using PEDOT:PSS layer showed higher J_{sc} (> 15 mA/cm^2) than that in the H256-PRISTINE structure. These results demonstrate that the different treatment techniques of secondary doping can be used to systematically control the properties of PEDOT:PSS layer and to optimize the hybrid PEDOT:PSS/buffer $(Si_{1-x}C_x:H)_{graded}$/a-Si:H heterojunction. The final discussion related to this structure and their potential advantages over conventional amorphous silicon solar cells is presented in section 5.4

5.3 PRELIMINARY RESULTS IN COMPLEX HYBRID PHOTOVOLTAIC DEVICES

Amorphous silicon solar cells have been extensively studied and some approaches have been developed in order to improve or applied this technology. Two examples of this are 1) fabrication of flexible solar cells and 2) optical schemes to improve absorption of light. In this section, the preliminary results obtained in hybrid solar cells fabricated on flexible substrates (Section 5.3.1) and hybrid structures with textured TCO contacts are discussed, this with the aim to demonstrate that the same approaches can be applied in hybrid solar cells.

5.3.1 HYBRID PHOTOVOLTAIC DEVICES ON FLEXIBLE SUBSTRATES

Figure 4.22 and table 4.22 show the J-V curves and the performance characteristics of different hybrid photovoltaic structures fabricated on PEN and Kapton flexible substrates. Two different thickness of AZO layer is proved and the structures are labeled as: a) Glass Reference, b) PEN/AZO (255 nm), c) PEN/AZO (510 nm), c) KAPTON/AZO (255 nm) and d) KAPTON/AZO (510 nm). The comparison between the two samples deposited on the PEN substrate shows a difference of J_{sc} from 3.21 mA/cm^2 (255 nm-AZO) to 9.79 mA/cm^2 (510 nm-AZO). Unlike glass, polymer substrates cannot be polished, and the surface morphology can affect significantly the electronic properties and photovoltaic characteristics. Films deposited on plastic substrate tend to reproduce defects of the substrates also creating discontinuities that are decreased by the increase of thickness of the films. The reason for this relies on the fact that the process of film growth, and, as a consequence, the film morphology in thin-film-based photovoltaic devices is sensitive to the morphology of the surface of the preceding layer where the film growth starts, affecting in this way both, an individual film properties as well as junction properties. On

the other hand, the performance characteristics between the samples fabricated with a different AZO thickness on "Kapton" substrates show very similar values (PCE ≈ 0.25 %). This because Kapton substrates are special flexible substrate fabricated for electronic applications with very low defects [118], then it is expected that films deposited on Kapton substrates are continuous even for very thin films. However, the J_{sc} values in the samples fabricated on "Kapton" substrates are significantly less which is expected due to its poor transmission T(λ) in the short wavelength region (Figure 5.11-a).

Since we are interested in finding out the contribution of the frontal interface to the electrical properties of the junction, the spectral dependencies of short circuit current J_{sc} (λ) in fabricated flexible photovoltaic structures were measured and analyzed. Spectral characteristics J_{sc} (hν) in the range of λ from 354 to 1200 nm for three hybrid structures (H43-2, H44-2, and H45-2) are presented in figure 5.11-b.

In J_{sc} (hν) dependence three regions can be distinguished: (1) low photon energy region (from hν = 1.8–2.2 eV) related to sub-gap absorption, determined mainly by properties of the intrinsic layer, (2) intermediate region (from hν= 1.8 to 3.0 eV) where the current is a result of contributions from entire PV structure and (3) high photon energy region (hν= 3.0 to 3.5 eV) where J_{sc} signal is mainly controlled by frontal interface properties. This last region and part of the region 2 are significantly shifted to low photon energy direction in the structure on "Kapton", because of its spectral transmission (Figure 5.11-a).

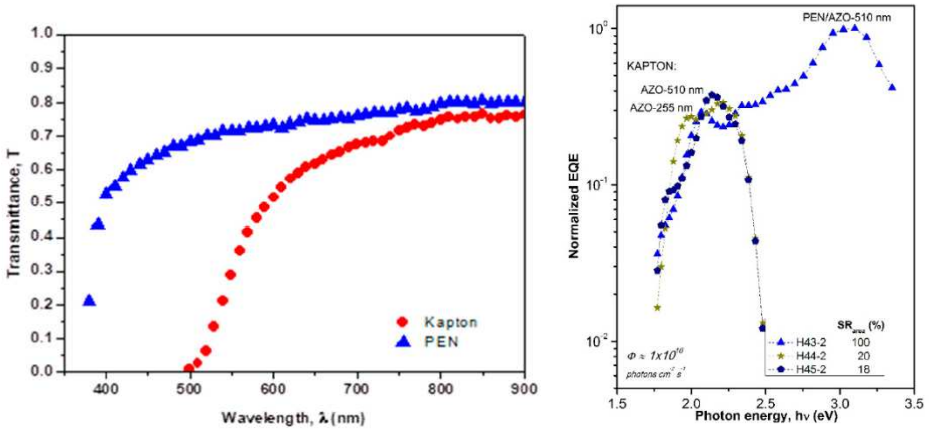

a) b)

Figure 5.11. a) Transmission spectra of the flexible substrates (PEN and "Kapton") used for fabrication of photovoltaic structures and b) Spectral response of short circuit current density J_{sc} (hν) for hybrid photovoltaic structures (1) H43-2; (2) H44-2; and (3) H45-2. Area under the curve (SR_{area}) is indicated for the samples taking H43-2 SR_{area} as reference.

The loss of the short circuit current due to suboptimal light harvesting in the structure on "Kapton" substrate can be estimated, comparing the areas under the corresponding curves of J_{sc} (λ) dependence (SR_{area}): it is 20% in the KAPTON/AZO (255 nm) structure and 18% in the KAPTON/AZO (255nm) structure, where 100% corresponds to the PEN/AZO (510 nm) device. However, it is interesting to note that short circuit current value J_{sc} (hν) in region 1 and part of the region 2 is higher (nearly by the factor

of 2) in the hybrid structure fabricated on "Kapton" substrate, even though the PEN substrate provides better optical transmission in the same range of wavelength. We tried to compare the junctions themselves fabricated on PEN and "Kapton" substrates employing recalculation of performance J-V characteristics for the structures on "Kapton" reducing them to those on PEN substrates. The factor for this recalculation is obtained from spectral characteristics of the real devices illuminated by AM 1.5 light. This analysis reveals differences in the junctions, mostly in the short circuit current density (about 15% less for the junction on "Kapton" substrate) while open circuit voltage shows practically the same value. We believe that worse junction properties of "Kapton"-the based device could arise from the morphological features of AZO surface deposited on "Kapton", characterized by the presence of sharp peaks of AZO, as shown by our AFM data [118]. Such peaks can produce additional stress on the film grown on top of it and in this way contribute to the deterioration of electronic properties of the junction. In addition, these peaks could be responsible for the creation of parasitic shunts across the junction deteriorating device performance.

About the open-circuit voltage, all the structures have close values V_{oc}= 550 – 565 mV, except for the sample PEN/AZO (255 nm) with V_{oc}= 405 mV. Low fill factor (FF) values (from 23 to 26%) are observed in all the structures resulting from losses of current in these not optimized structures. Low FF often arises from the parasitic shunt and series resistances and might be a signal of leakage through the organic layer or/and other semiconductor layers. Only a few works have reported thin-film solar cells based on PEDOT:PSS/a-Si:H on glass or flexible substrate. In Ref. [132] a hybrid p-i-n structure using pristine PEDOT:PSS on a glass substrate has been reported reaching a PCE= 2.1%. On the other hand, a flexible n-i-p type structure based on PEDOT:PSS/a-Si:H interface has been reported in Ref. [55] with a maximum efficiency of 6.52%. It is important to note that the structure reported in Ref. [55] was deposited on a non-transparent Ag-coated polyimide substrate and fabricated as a substrate configuration. The advantage of use-transparent substrates, such as PEN and a p-i-n-type structure, as reported in this work, is that the substrate can be simultaneously used as a supporting structure as well as a window for the capture of light (superstrate configuration).

5.3.2 HYBRID PHOTOVOLTAIC DEVICES ON TEXTURED AZO AS TCO

In figure 4.24, the SEM images of AZO films texturized with different HCl concentrations in an etchant solution are presented. It can be observed that the thickness reduction and the increase of the sheet resistance are proportional to the HCl concentration in the etchant solution. Also, the size of the craters formed for the texturized increases when the HCl concentration is increased. The AZO film texturized with 0, 0.2, 0.5 and 1 % HCl concentrations were chosen to fabricated a-Si: H-based and hybrid photovoltaic devices. In figure 4.25 the J-V curves of the a-Si: H-based and hybrid photovoltaic devices

are presented. Figure 5.12 presents the J_{sc} and V_{oc} for all samples as a function of the HCl concentration in pure inorganic and hybrid structures.

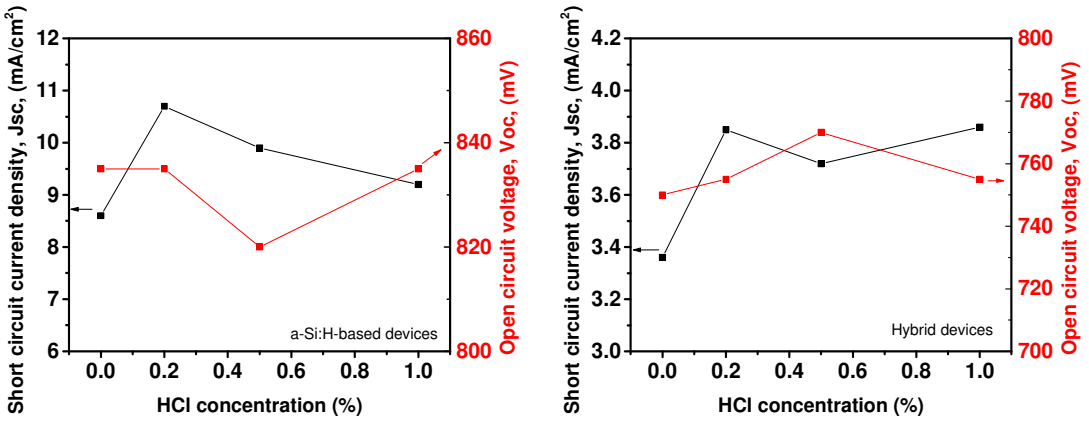

Figure 5.12. J_{sc} and V_{oc} values of a) a-Si:H-based and b) hybrid photovoltaic devices with AZO film texturized with an etchant solution with different HCl concentrations.

In the case of pure inorganic structure, it is observed that the maximum J_{sc}= 10.7 mA/cm^2 is obtained with the AZO film texturized with 0.2 % HCl concentration, which is equivalent to a gain in J_{sc} in 25 %. On the other hand, the V_{oc} values obtained are practically the same. This because the electronic properties of AZO films were not radically changed. However, a reduction of the FF is observed in all samples with a texturized AZO film and this can may be attributed to the roughness surface of the AZO films texturized, introducing parasitic resistances. Despite this, the device with the AZO film texturized with 0.2 % HCl concentration have the best PCE, which increased from PCE= 4.1 % (sample reference) to PCE= 4.7 %. These results can be used as reference and guide in the discussion of the application of textured AZO films in a hybrid structure.

In the case of the hybrid photovoltaic devices, all the samples have lower performance characteristics than that in the inorganic structure and although an increase in J_{sc} is observed in structures with textured AZO layers, the maximum gain is bare of the 15 %. This can be attributed to two factors: 1) the no optimized AZO/PEDOT:PSS interface and b) the organic layer prepares a smooth and planar surface for the deposition of an intrinsic a-Si:H layer (figure 4.23) avoiding the transfer of texturization shape of the TCO to the a-Si:H layers. These results show that the textured TCO approach in hybrid p-i-n structures needs to be reconsidered in future works.

5.4 HYBRID PEDOT:PSS/A-SI:H FRONTAL INTERFACE VERSUS INORGANIC FRONTAL INTERFACES

Organic materials for photovoltaic (PV) applications have been in focus during the last decade. One important advantage of these materials is their solution-type processing that allows deposition at room temperature and atmospheric pressures. Recently, these materials have also attracted attention as an alternative to common n-type and p-type inorganic materials to simplify the formation of p-/i-/n- junctions in solar cells [133-135]. However, inorganic materials are still the most widely used as an alternative to form these heterojunctions in the frontal interface. For example, doped nc-SiO_x:H layers were proposed by Fang et. al. (2018) [136] to improve performance characteristics in amorphous silicon solar cells, but these configurations still involve complex optimizations at the n/i or i/p interfaces similar to those in the interfaces based on doped-SiC:H layers.

Figure 5.13-a and table 5.2 show the comparison between the final device using the hybrid heterojunction developed in this thesis work, the initial hybrid structure developed in [5] (2015) and the inorganic structure in [101] (2018) used as a reference.

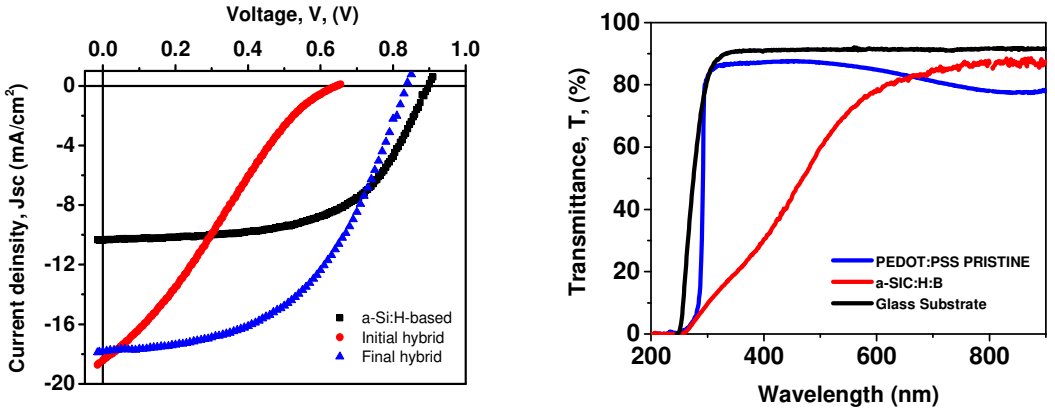

Figure 5.13. a) Comparison of J-V curves of the initial and final hybrid structure developed in this thesis work and inorganic structure. b) Optical transmittance spectra of an amorphous silicon carbine film doped with boron (a-SiC:H:B), PEDOT:PSS PH1000 pristine film, and glass substrate.

Type	Structure	Temperature deposition	J_{sc} (mA/cm^2)	V_{oc} (mV)	FF (%)	PCE (%)
p-i-n	a-Si:H-based	**160 °C**	10.7	895	57.0	5.6
p-i-n	Initial hybrid	**160 °C**	18.4	640	25.6	3.0
p-i-n	**Final hybrid**	**160 °C**	**17.8**	**840**	**50.4**	**7.5**

Table 5.2. Performance characteristics for initial and final hybrid photovoltaic devices studied in this work and inorganic structure.

It is interesting to note from the comparison that the hybrid configurations have higher values of J_{sc} than that obtained in the a-Si:H reference structure. The higher J_{sc} in the structures using hybrid heterojunctions in the frontal interface can be related to different factors. The first may relate to the

relatively high optical transmission of PEDOT:PSS in comparison to that of a p-type a-SiC:H:B layer used in the inorganic solar device. Figure 5.13-b shows the optical transmittance spectra $T(\lambda)$ of the PEDOT:PSS and the a-SiC:H:B layers deposited on a glass substrate. Glass/PEDOT:PSS system shows a remarkable transmittance with an average value of T_{avg}= 85 % in the wavelength range from 300 to 750 nm. This contrasts with the transmittance of the Glass/a-SiC:H:B system, in which the average value is T_{avg}= 59 %. This represents an increase of ~25 % of the light reaching the absorber layer in the hybrid configurations. The comparison between the hybrid structures shows that the hybrid structure developed in this work has higher V_{oc} and FF in contrast to those in the initial structure. Open circuit voltage and fill factor are very complex parameters involved in the solar cell performance, and these can be affected by several aspects and mechanisms in inorganic and organic configurations. However, the improvement of these parameters in our hybrid structure can be attributed to a better hole collection at the frontal interface improved by the buffer layer and a good alignment between valence band conduction of silicon and PEDOT:PSS work function (see section 5.2.3).

Figure 5.14 shows the normalized external quantum efficiency (EQE) measured for the best hybrid structure and the a-Si:H reference. There are small differences between the trends of the hybrid and reference structures over the visible–IR range wavelength (420 - 700 nm) related to photon absorption and charge carrier collection at the bulk. The main difference between spectra in this region is that the reference structure shows an EQE maximum at a wavelength of 550 nm, in contrast to hybrid structures that show a maximum at 370 nm.

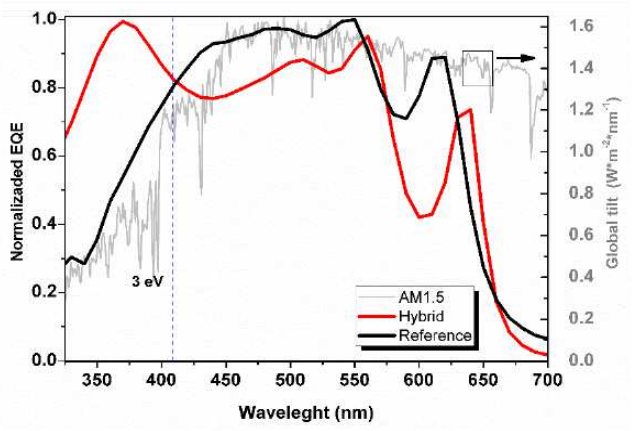

Figure 5.14. (a) External quantum efficiency (EQE) spectra of a photovoltaic structures based on amorphous silicon (a-Si:H) (REFERENCE) and a hybrid photovoltaic structure with a buffer layer and a PEDOT:PSS PH1000 film treated with DIP in IPA (H259-DIP). (b) Comparison of EQE spectra in the range from 300 to 450 nm obtained using both LED and GLOBAL source.

This behavior has also been observed in similar structures reported by Lee et. al. [55] and seems to be characteristic of PEDOT:PSS/a-Si:H structures. The hybrid structure shows an exceptional response at wavelengths below 420 nm compares to that in the reference structure. A clear improvement in the

charge carrier collection due to the implementation of the hybrid heterojunction in the frontal interface was found. This improvement is related to the properties of the post-treated PEDOT:PSS PH1000 and the hybrid heterojunction in the frontal interface as we discussed before: (i) low PEDOT:PSS light absorption (figure 5.13-b), (ii) reduction of electron diffusion by the electron-blocking PSS-enriched layer (figure 5.10), and (iii) enhancement of the internal electric field due to the buffer layer. Also, it is important to note that the deposition of the PEDOT:PSS layer creates an abrupt interface with a-Si:H layer and there is not dopant diffusion improving the quality of the heterojuction.

Finally, Table 5.3 compares the performance characteristics of the developed hybrid structure with structures based on a PEDOT:PSS/a-Si:H interface reported in the literature [55] and a high-performance amorphous silicon structure fabricated at low temperature (< 200 °C) [108-109]. It is worth mentioning that the hybrid structures reported to date, reach the highest short-circuit current values J_{sc} ~20 mA/cm^2 without using a complex texture process to enhance optical absorption. In contrast, FF values in these structures are lower than those for pure amorphous silicon solar cells.

Type	Structure	T_d	Texturing	Jsc (mA/cm^2)	Voc (mV)	FF (%)	PCE (%)	REF.
p-i-n	PEDOT:PSS/a-Si:H(i)/µc-Si(i)/ µc-Si(n)	200 °C	No	4.55	883	51	2.1	[54]
p-i-n	PEDOT:PSS+Au-NPs/WO_3/ a-Si:H(i)	---	Yes	14.60	560	67	5.49	[87]
p-i-n	PEDOT:PSS/a-Si:H(i)	---	No	14.08	680	50	4.78	[88]
n-i-p	a-Si:H(n)/ a-Si:H(i)/PEDOT:PSS	---	No	19.1	800	48	7.40	[55]
p-i-n	**PEDOT:PSS/a-Si:CH/a-Si:H(i)**	**160 °C**	**No**	**17.8**	**840**	**50.4**	**7.5**	**[This work]**
a-Si:H-based	Buffer/p-a-SiO_x:H/a-SI:H	175 -200 °C	Yes	13.3	840	75	8.4	[109]

Table 5.3. Comparison of performance parameters of hybrid photovoltaic structure fabricated in this work and similar structures reported in literature.

To address this issue, further investigation should be accomplished to optimize the TCO/PEDOT:PSS interface. However, PCE's of the hybrid structures are comparable to those in a well-optimized amorphous silicon structure fabricated at low deposition temperature. This demonstrates the potential of the PEDOT:PSS to substitute complex frontal interface schemes (p-SiC:H, µm-Si, SiO_x:H, etc.) that use inorganic materials. From the technological point of view, hybrid devices have advantages, for example, the reduction of vacuum and high-temperature stages providing simplification of processes.

CHAPTER VI

6. CONCLUSIONS

In this thesis the development of a hybrid PEDOT:PSS/ a-Si:H heterojunction for photovoltaic devices application has been studied. The first part of this work had an emphasis on the study of deposition and treatment processes of the a-Si:H and PEDOT:PSS layers, respectively, to reach compatibility between technologies. Then, the construction of the hybrid heterojunction as a frontal interface of thin film solar cells was investigated. The results have shown that the PEDOT:PSS had a better characteristic for the formation of the hybrid PEDOT:PSS /a-SiH heterojunction. Then, the use of buffer layers was proposed to improve the hybrid interfaces. Finally, the developed hybrid technology was compared with amorphous silicon and other hybrid devices reported in literature and it was demonstrated its high potential for photovoltaic applications. From the main research axis investigated in this work, the main findings are presented:

Deposition process of a-Si:H layer for hybrid technology

The major issues of the construction of complex hybrid structures using organic semiconductors and inorganic materials are the compatibility between their deposition processes. Devices based on organic semiconductors require process under specific conditions to avoid the degradation of the polymers during the fabrication. Following this, in the PECVD process, two conditions should be considered: 1) deposition temperature and 2) ion bombardment. The PECVD process of a-Si:H films was studied under fixed conditions in the range of pressure between 430 to 830 mTorrs at different deposition temperature (T_d = 160, 175 and 220 °C). The deposition rate of the obtained a-Si:H films increased from r_d= 0.51 to 0.65 Å/s and r_d= 0.73 to 0.79 Å/s with an increase of pressure at deposition temperatures T_d= 220 and 175 °C, respectively, indicating that the experiments were carried out at low-pressure regimen. It is expected that at lower pressures, the energetic species are less than that at higher pressures and this reduces ion bombardment on the surface of the films; key factor to avoid degradation of polymer layers exposed to the plasma. These results also demonstrated that is possible to obtain quality device a-Si:H films with photoresponse above 10^5 at deposition temperatures T_d < 200 °C. On the other hand, the result on hybrid solar cells devices using the PEDOT:PSS/a-Si:H heterojunction shown that better performance characteristic were obtained at the low-pressure range from 500-600 mTorrs and at low deposition temperature of Td= 160 °C supporting our hypothesis that the parameters of PECVD can be adjusted to improve the quality of the PEDOT:PSS/a-Si:H heterojunction.

Secondary doping of PEDOT:PSS layer

Different methods have been proposed to enhance the electrical and morphological properties of PEDOT:PSS films to control and improve their characteristics for different organic device applications. This work proposed applied different post-deposition treatment of IPA in the PEDOT:PSS layer in order to improve its conductivity for application in the construction of the studied hybrid heterojunction. An increase in the conductivity was observed in post-treated PEDOT:PSS films according to the aggressivity of the treatment from the pristine layer(σ=0.48 S/cm), vapor (σ=1.7 S/cm), drop (σ=20.7 S/cm), and dip (σ=48.5 S/cm) technique treatment. It is important to note that these changes in conductivity (two orders of magnitude) are similar to those obtained in the doping processes of inorganic semiconductors but with the advantage of organic technology (safe, room temperature and atmospheric pressure processes). The mechanisms of the change of conductivity in the PEDOT:PSS films were investigated, the AFM, Raman and FTIR spectroscopies shown that the post-deposition treatment results in a self-assembling process of the nanostructure of the PEDOT:PSS layer, forming a PSS-enriched surface and a PEDOT-enriched bulk without degradation at the molecular level. Finally, these post-treated PEDOT:PSS films were used in hybrid structures, and the performance characteristics were improved in comparison to those in the reference structure.

PEDOT:PSS / $(Si_{1-x}C_x:H)_{graded}$ /a-SI:H heterojunction

By tailoring the surface of PEDOT:PSS layer by secondary doping and using a PEDOT:PSS/$(Si_{1-x}C_x:H)_{graded}$/a-Si:H heterojunction, the optical transparency of the frontal interface and “built-in” electrical field in an amorphous solar cell were improved. The best performance characteristics (J_{sc}= 17.8 mA/cm^2, V_{oc}= 840 mV, FF= 50.4 % and PCE= 7.5 %) were obtained using a PEDOT:PSS/buffer/a-Si:H heterojunction in the hybrid structure fabricated with a PEDOT:PSS layer treated with the dip technique. The increase of J_{sc} was explained by a remarkable improvement in charge carrier collection due to the nanostructural arrangement of the PEDOT:PSS layer, the alignment of bands and high transmittance of the hybrid frontal interface. The normalized external quantum efficiency (EQE) measurement shown small differences between the trends of the hybrid and reference inorganic structure over the visible–IR range wavelength (420–800 nm) related to photon absorption and charge carrier collection at the bulk. However, the hybrid structures showed a higher charge collection at the wavelength of 524 nm in comparison to that in the inorganic reference structure. This was demonstrated to be attributable to several factors as (i) low PEDOT:PSS light absorption, (ii) reduction of electron diffusion by the electron-blocking PSS-enriched layer, (iii) enhancement of the internal electric field due to the buffer layer, and iv) an abrupt interface PEDOT:PSS / a-Si:H layer. Finally, the hybrid devices were fabricated on flexible substrates and textured TCO to explore new applications of the technology.

Major contributions to the research field.

The development of a hybrid organic-inorganic heterojunction for photovoltaic devices applications has been studied and applied in PV applications. The best performance characteristics of the fabricated hybrid devices obtained in this work are the highest reported to date for similar hybrid solar cells and comparable to those in textured well-optimized amorphous silicon solar cells fabricated at low deposition temperature (T_d < 200 °C). It is important to note that the structure was a planar substrate-type configuration and the PEDOT:PSS layer was exposed to glow discharge during the fabrication of the heterojunction. Then, contrary to the general belief, it has been demonstrated that PEDOT:PSS layers are compatible with the PECVD process at low deposition temperatures (Td< 200°C). On the other hand, the mechanisms of secondary doping in PEDOT:PSS films were investigated. It has been demonstrated a self-assembling process of the nanostructure of the PEDOT:PSS layer and control of the conductivity by two orders of magnitude depending on the treatment technique. This approach demonstrates to be a key factor in the construction of the hybrid heterojunction.

This work concludes that PEDOT:PSS is an ideal material to substitute p-type inorganic materials with the possibility to simplify the complex process of doping and improve the charge collection in the frontal interface. The application of the hybrid heterojunction can be extended to other silicon-based technologies opening a landscape of application of the polymer in other devices, for example HIT solar cells, flexible devices, etc.

BIBLIOGRAFIA

[1] REN21 2019, Report, Renewables 2019 Global Status, January 2019. [Online]. Available: http://www.ren21.net. [Last access: December 2019].

[2] Ho-Baillie, Martin A. Green Yoshihiro Hishikawa Ewan D. Dunlop Dean H. Levi Jochen Hohl-Ebinger Anita W.Y., Solar cell efficiency tables (version 51), Progress in photovoltaics, vol. 26, nº 1, pp. 3-12, January 2018.

[3] Matthew Wright, Ashraf Uddin, Organic—inorganic hybrid solar cells: A comparative review, Solar Energy Materials and Solar Cells, vol. 107, pp. 87-111, 2012.

[4] T. T. Chow, G. N. Tiwari, and C. Menezo, Hybrid Solar: A Review on Photovoltaic and Thermal Power Integration, International Journal of Photoenergy, vol. 2012, p. 17, 2012.

[5] Cosme, I; Kosarev, A; Mansurova, S; Olivares, A.J.; Martinez, H.E.; Itzmoyotl, A. Hybrid photovoltaic structures based on amorphous silicon and P3HT:PCBM/PEDOT:PSS polymer semiconductors. Org. Electron. 2016, 38, 271-277.

[6] Schmidt, J; Titova, V; and Zielke, D. Organic-silicon heterojunction solar cells: open-circuit voltage potential and stability. Appl. Phys. Lett. 2013, 103 183901.

[7] H.F. Sterling, R.C.G. Swann, Chemical vapour deposition promoted by r.f. discharge, Solid-State Electronics, Volume 8, Issue 8, 1965, Pages 653-654.

[8] R. C. Chittick, J. H. Alexander, and H. F. Sterling, J. Electrochem. Soc. 116, 77 (1969).

[9] W. E. Spear & P. G. Le Comber (1976) Electronic properties of substitutionally doped amorphous Si and Ge, The Philosophical Magazine: A Journal of Theoretical Experimental and Applied Physics, 33:6, 935-949.

[10] J. Poortmans and V. Arkhipov, (2006). Thin film solar cells: Fabrication, Characterization and applications, IMEC, Leuven, Belgium, John Wiley & Sons, Ltd.

[11] Street, R. (1991). Growth and structure of amorphous silicon. In Hydrogenated Amorphous Silicon (Cambridge Solid State Science Series). Cambridge: Cambridge University Press.

[12] Werner Luft and Y. Simon Tsuo, (1993). Hydrogenated amorphous silicon alloy deposition processes, NREL, Golden, Colorado, Marcel Dekker Inc.

[13] J.C. Knights, G. Lucovsky, R.J. Nemanich, Defects in plasma-deposited a-Si: H, Journal of Non-Crystalline Solids, Volume 32, Issues 1–3, 1979, Pages 393-403.

[14] Tatsuo Shimizu, Kenji Nakazawa, Minoru Kumeda, Shoichi Ueda, Incorporation scheme of H reducing defects in a-Si studied by NMR and ESR, Physica B+C, Volumes 117–118, Part 2, 1983, Pages 926-928.

[15] Bhat, P.K., Marshall, C., Sandwisch, J., Chatham, H., Schropp, R.E.I., and Madan, A., Preparation and properties of high deposition rate a-Si:H films and solar cells using disilane, Proc. of 20th IEEE Photovoltaic Specialist Conference (IEEE, Las Vegas, 1988), p. 91.

[16] Ueda, M., T. Imura, and Y. Osaka. “Effect of substrate temperature on properties of a-Si:H prepared at high deposition rate,” Proc. 10th Symp, onIonSources and Ion-Assisted Technology, 1986.

[17] Satoshi Nishikawa et al 1985 Jpn. J. Appl. Phys. 24 639

[18] J. C. Knights and R. A. Lujan, Microstructure of plasma deposited aSi:H films, Applied Physics Letters 35, 244 (1979).

[19] M. H. Brodsky, On the deposition of amorphous silicon films from glow discharge plasmas of silane, Thin Solid Films, 40 (1977) L23- L25 L23.

[20] S. J. Hudgens, A.G. Johncock, and S.R. Ovishinsky, Low pressure microwave glow discharge process for high deposition rate amorphous silicon alloy, Journal of Non-C[ystalline Solids 77 & 78 (1985) 809-812.

[21] Michitoshi Ohnishi et al 1988 Jpn. J. Appl. Phys. 27 40.

[22] H. Shirakawa, E. J. Lois, A; G. MacDiarmind, C. K. Chiang and A. J. Heeger, Synthesis of electrically conducting organic polymers: halogen derivatives of polyacetylene, (CH)x, J. Chem. Soc., Chem. Commun., 1977, 578-580.

[23] Yen-Ju Cheng, Sheng-Hsiung Yang and Chain-Shu Hsu, Synthesis of Conjugated Polymers for Organic Solar Cell Applications Chem. Rev. 2009, 109, 11, 5868-5923.

[24] Xiaodong Wang and Zhiming M. Wang, (2014). High-efficiency solar cells: Physics, Materials, and Devices, Beijing, China, Springer.

[25] Zhou, Y., Geng, J., Li, G., Zhou, E., Chen, L., Zhang, W.; Crystal structure and morphology of phenyl-capped tetraaniline in the leucoemeraldine oxidation state, J. Polym. Sci. B Polym. Phys. 44, 764–769 (2006)

[26] F. Jonas and W. Krafft. EP 440957 (Bayer AG), Prior: December 20, 1990.

[27] F. Jonas, W. Krafft, and B. Muys. 1995. Poly(3,4-ethylenedioxythiophene): Conductive coatings, technical applications and properties. Macromol Symp 100:169–173.

[28] A. Elschner, S. Kirchmeyer, W. Lövenich, U. Merker and, K. Reuter, (2011). PEDOT: Principles and applications of an intrinsically conductive polymer, Boca Raton FL, USA, CRC Press, Taylor & Francis Group.

[29] G. Zotti, S. Zecchin, G. Schiavon, F. Louwet, L. Groenendaal, X. Crispin, W. Osikowicz, W. Salaneck, and M. Fahlman. 2003. Electrochemical and XPS studies towards the role of monomeric and polymeric sulfonate counterions in the synthesis, composition and properties of poly(3,4-ethylenedioxythiophene). Macromolecules 36: 3337–3344.

[30] Shi H, Liu C, Jiang Q, Xu J (2015) Effective approaches to improve the electrical conductivity of PEDOT:PSS: a review. Adv Electron Mater 1(4):1500017.

[31] M. Döbbelin, R. Marcilla, C. Tollan, J. A. Pomposo, J.-R. Sarasua, D. Mecerreyes, A new approach to hydrophobic and wáter-resistant poly(3,4-ethylenedioxythiophene):poly(styrenesulfonate) films using ionic liquids, J. Mater. Chem. 2008, 18, 5354.

[32] A. Benor, S.-y. Takizawa, C. Pérez-Bolívar, P. Anzenbacher, Efficiency improvement of fluorescent OLEDs by tuning the working function of PEDOT:PSS using UV-ozone exposure, Org.Electron. 2010, 11, 938.

[33] Nardes, A. M., Kemerink, M., Kok, de, M. M., Vinken, E., Maturova, K., & Janssen, R. A. J. (2008). Conductivity, work function, and environmental stability of PEDOT:PSS thin films treated with sorbitol. Organic Electronics, 9(5), 727-734.

[34] G. Wang, S.-I. Na, T.-W. Kim, Y. Kim, S. Park, T. Lee, effect of PEDOT:PSS-molecule interface on the charge transport characteristics of the large-area molecular electronic junctions, Org. Electron. 2012, 13, 771.

[35] S. I. Na, G. Wang, S. S. Kim, T. W. Kim, S. H. Oh, B. K. Yu, T. Lee, D. Y. Kim, Evolution of nanomorphology and anisotropic conductivity in solvent-modified PEDOT:PSS films for polymeric anodes of polymer solar cells, J. Mater. Chem. 2009, 19, 9045.

[36] S. I. Na, S. S. Kim, J. Jo, D. Y. Kim, Efficient and flexible ITO-free organic solar cells using highly conductive polymer anodes, Adv. Mater. 2008, 20.

[37] K. Lim, S. Jung, S. Lee, J. Heo, J. Park, J.-W. Kang, Y.-C. Kang, D.-G. Kim, Org. Electron. 2014, 15, 1849.

[38] H. Shi, C. Liu, J. Xu, H. Song, B. Lu, F. Jiang, W. Zhou, G. Zhang, Q. Jiang, ACS Appl. Mater. Interfaces 2013, 5, 12811.

[39] J. P. Thomas, L. Zhao, D. McGillivray, K. T. Leung, J. Mater. Chem. A 2014, 2, 2383.

[40] Q. Wei, M. Mukaida, Y. Naitoh, T. Ishida, Adv. Mater. 2013, 25, 2831.

[41] J. P. Thomas, K. T. Leung, Adv. Funct. Mater. 2014, 24, 4978.

[42] L. A. A. Pettersson, S. Ghosh, O. Ingan€ as, Optical anisotropy in thin films of poly (3,4-ethylenedioxythiophene)–poly(4-styrenesulfonate), Org. Electron. 3 (2002) 143–148.

[43] S. Garreau, G. Louarn, S. Lefrant, J. P. Buisson, and G. Froyer. 1999. Optical study and vibrational analysis of the poly(3,4-ethylenedioxythiophene) (PEDOT). Synth Met 101(1–3):312–313.

[44] S. Garreau, G. Louarn, J. P. Buisson, G. Froyer, and S. Lefrant. 1999. In situ spectroelectrochemical Raman studies of poly(3,4-ethylendioxythiophene) (PEDT). Macromol 32(20):6807–6812.

[45] C. Kvarnstrom, H. Neugebauer, N. S. Sariciftci, S. Blomquist, A. Ivaska, H. J. Ahonen, and J. Kankare. 1999. In situ FTIR spectroelectrochemical characterization of poly(3,4-ethylenedioxythiophene) films. Synth Met 101(1):66.

[46] C. Kvarnstrom, H. Neugebauer, S. Blomquist, H. J. Ahonen, J. Kankare, and A. Ivaska. 1999. In situ spectroelectrochemical characterization of poly(3,4-ethylenedioxythiophene). Electrochim Acta 44(16):2739–2750.

[47] K. E. Aasmundtveit, E. J. Samuelsen, L. A. A. Pettersson, O. Inganas, T. Johansson, and R. Feidenhans l. 1999. Structure of thin films of poly(3,4-ethylene dioxythiophene). Synth Met 101(1–3):561–564.

[48] K. Su, N. Nuraje, L. Zhang, I.-W. Chu, R. M. Peetz, H. Matsui, and N.-L. Yang. 2007. Fast conductance switching in single-crystal organic nanoneedles prepared from an interfacial polymerization-crystallization of 3,4-ethylenedioxythiophene. Adv Mater 19(5):669–672.

[49] G. Greczynski, T. Kugler, and W. R. Salaneck. 1999. Characterization of the PEDOT-PSS system by means of X-ray and ultraviolet photoelectron spectroscopy. Thin Solid Films 354(1,2):129–135.

[50] Manufacturer: H. C. Starck Clevios GmbH, Leverkusen, Germany, www.clevios.com.

[51] Al-Hashimi, M., Kadem, B., Rahaq, Y. et al. The effects of solvent treated PEDOT:PSS buffer layer in organic solar cells. J Mater Sci: Mater Electron 29, 13889–13896 (2018).

[52] Kim, Y. H., Sachse, C., Machala, M. L., May, C., Müller-Meskamp, L. and Leo, K. (2011), Highly Conductive PEDOT:PSS Electrode with Optimized Solvent and Thermal Post-Treatment for ITO-Free Organic Solar Cells. Adv. Funct. Mater., 21: 1076-1081.

[53] Matthew Wright, Ashraf Uddin, Organic—inorganic hybrid solar cells: A comparative review, Solar Energy Materials and Solar Cells, Volume 107, 2012, Pages 87-111.

[54] Evan L. Williams, Ghassan E. Jabbour, Qi Wang, Sean E. Shaheen, David S. Ginley, and Eric A. Schiff, Conducting polymer and hydrogenated amorphous silicon hybrid solar cells, Applied Physics Letters 87, 223504 (2005).

[55] Yoo Jeong Lee, Changbong Yeon, Jung Wook Lim, Sun Jin Yun, Flexible p-type PEDOT:PSS/a-Si:H hybrid thin film solar cells with boron-doped interlayer, Solar Energy, Volume 163, 2018, Pages 398-404.

[56] F. Jonas, W. Krafft, B. Muys, Poly(3,4-ethylenedioxythiophene): Conductive coatings, technical applications and properties, Macromol. Symp. 1995, 100, 169.

[57] Jianyong Ouyang, “Secondary doping” methods to significantly enhance the conductivity of PEDOT:PSS for its application as transparent electrode of optoelectronic devices, Displays, Volume 34, Issue 5, 2013, Pages 423-436.

[58] J. Huang, P. F. Miller, J. C. de Mello, A. J. de Mello, D. D. C. Bradley, Influence of thermal on the conductivity and morphology of PEDOT/PSS films, Synth. Met. 2003, 139, 569.

[59] A. Moujoud, S. H. Oh, H. S. Shin, H. J. Kim, On the mechanism of conductivity enhancement and work function control in PEDOT:PSS film through UV-light treatment, Phys. Status solidi A 2010, 207, 1704.

[60] Yow-Jon Lin, Fu-Ming Yang and Chi-Yen Huang, Increasing the work function of poly(3,4-ethylenedioxythiophene) doped with poly(4-styrenesulfonate) by ultraviolet irradiation, Appl. Phys. Lett. 91, 092127 (2007).

[61] Joseph P. Thomas, L. Zhao, D. McGillivray and Kam T. Leung, High-efficiency hybrid solar cells by nanostructural modification in PEDOT:PSS with co-solvent addition, J. Mater. Chem. A, 2014,2, 2383-2389.

[62] Kyounga Lim, Sunghoon Jung, Seunghun Lee, Jinhee Heo, Juyun Park, Jae-Wook Kang, Yong-Cheol Kang, Do-Geun Kim, The enhancement of electrical and optical properties of PEDOT:PSS using one-step dynamic etching for flexible application, Organic Electronics, Volume 15, Issue 8, 2014, Pages 1849-1855.

[63] J. Y. Kim, J. H. Jung, D. E. Lee, J. Joo, Enhancement of electrical conductivity of poly(3,4-ethylenedioxythiophene)/poly(4-styrenesulfonate) by a change of solvents, Synth. Met. 2002, 126, 311.

[64] A. J. Mäkinen, I. G. Hil , R. Shashidhar , N. Nikolov , Z. H. Kafafi, Hole injection barriers at polymer anode/small molecule interfaces, Appl. Phys. Lett. 2001, 79, 557.

[65] S. L. Lai, M.Y. Chan, M.K. Fung, C.S. Lee, S.T. Lee, Concentration effect of glycerol on the conductivity of PEDOT film and the device performance, Materials Science and Engineering: B, Volume 104, Issues 1–2, 2003, Pages 26-30.

[66] Rwei, S.-P.; Lee, Y.-H.; Shiu, J.-W.; Sasikumar, R.; Shyr, U.-T. Characterization of Solvent-Treated PEDOT:PSS Thin Films with Enhanced Conductivities. Polymers 2019, 11, 134.

[67] C. Badre, L. Marquant, A. M. Alsayed, L. A. Hough, Highly conductive Poly(3,4-ethylenedioxythiophene):Poly(styrenesulfonate) Films Using 1-Ethyl-3-methylimidazolium Tetracyanoborate Ionic Liquid, Adv. Funct. Mater. 2012, 22, 2723.

[68] Jianyong Ouyang, Qianfei Xu, Chi-Wei Chu, Yang Yang, Gang Li, Joseph Shinar, On the mechanism of conductivity enhancement in poly(3,4-ethylenedioxythiophene):poly(styrene sulfonate) film through solvent treatment, Polymer, Volume 45, Issue 25, 2004, Pages 8443-8450.

[69] Y. Xia, H. Zhang, J. Ouyang, J., Highly conductive PEDOT:PSS films prepared through a treatment with zwitterions and their application in polymer photovoltaic cells, Mater. Chem. 2010, 20, 9740.

[70] Wenfeng Zhang, Xianghong Bi, Xuemei Zhao, Zhiqiang Zhao, Jun Zhu, Songyuan Dai, Yalin Lu, Shangfeng Yang, Isopropanol-treated PEDOT:PSS as electron transport layer in polymer solar cells, Organic Electronics, Volume 15, Issue 12, 2014, Pages 3445-3451.

[71] Isidro Cruz-Cruz, Marisol Reyes-Reyes, Román López-Sandoval, Formation of polystyrene sulfonic acid surface structures on poly(3,4-ethylenedioxythiophene): Poly(styrenesulfonate) thin films and the enhancement of its conductivity by using sulfuric acid, Thin Solid Films, Volume 531, 2013, Pages 385-390.

[72] Y. Xia, K. Sun, J. Ouyang, Solution-processed metallic conducting polymer films as transparent electrode of optoelectronic devices, Adv. Mater. 2012, 24, 2436.

[73] Yinhua Zhou, Canek Fuentes-Hernandez, Jaewon Shim, Jens Meyer, Anthony J. Giordano, Hong Li, Paul Winget, Theodoros Papadopoulos, Hyeunseok Cheun, Jungbae Kim, Mathieu Fenoll, Amir Dindar, Wojciech Haske, Ehsan Najafabadi, Talha M. Khan, Hossein Sojoudi, Stephen Barlow, Samuel Graham, Jean-Luc Brédas, Seth R. Marder, Antoine Kahn and, Bernard Kippelen, A Universal Method to Produce Low–Work Function Electrodes for Organic Electronics, 2012, Science, Vol. 336, Issue 6079, pp. 327-332.

[74] J. Tong, S. Xiong, Y. Zhou, L. Mao, X. Min, Z. Li, F. Jiang, W. Meng, F. Qin, T. Liu, R. Ge, C. Fuentes Hernandez, B. Kippelen and Y. Zhou, Flexible all-solution-procesed all-plastic multijunction solar cells for powering electronic devices, Mater. Horiz., 2016,3, 452-459.

[75] X. Wang, X. Zhang, L. Sun, D. Lee, S. Lee, M. Wang, J. Zheo, Y. Shao-Horn, M. Dinca, T. Palacios and K. K. Gleason, High electrical conductivity and carrier mobility in oCVD PEDOT thin films by engineered crystallization and acid treatment Sciences Adv. 2018.

[76] B. J. Skromme, Semiconductor Heterojunctions, Editor(s): K.H. Jürgen Buschow, Robert W. Cahn, Merton C. Flemings, Bernhard Ilschner, Edward J. Kramer, Subhash Mahajan, Patrick Veyssière, Encyclopedia of Materials: Science and Technology, Elsevier, 2006, Pages 1-11.

[77] Capasso F, Margaritondo G (eds.), 1987, Heterojunction Band Discontinuities: Physics and Device Applications, Amsterdam, Elsevier.

[78] D. M. Chapin, C. S. Fuller, and G. L. Pearson, A New Silicon p-n Junction Photocell for Converting Solar Radiation into Electrical Power, Journal of Applied Physics 25:5, 676-677, (1954).

[79] Matthew Wright, Ashraf Uddin, ≪Organic—inorganic hybrid solar cells: A comparative review,≫ Solar Energy Materials and Solar Cells, vol. 107, pp. 87-111, 2012.

[80] T. T. Chow, G. N. Tiwari, and C. Menezo, Hybrid Solar: A Review on Photovoltaic and Thermal Power Integration, International Journal of Photoenergy, vol. 2012, p. 17, 2012.

[81] Mariani G., Wang Y., Kaner R.B., Huffaker D.L. (2014) Hybrid Solar Cells: Materials, Interfaces, and Devices. In: Wang X., Wang Z. (eds) High-Efficiency Solar Cells. Springer Series in Materials Science, vol 190. Springer, Cham

[82] S. Avasthi, S. Lee, Y.-L. Loo, J.C. Sturm, Role of majority and minority carrier barriers silicon/organic hybrid heterojunction solar cells, Adv. Mater., 23 (2011), pp. 5762-5766.

[83] K. A. Nagamatsu, S. Avasthi, J. Jhaveri, J.C. Sturm, A 12% efficient silicon/PEDOT:PSS heterojunction solar cell fabricated at < 100 °C, IEEE J. Photovoltaics, 4 (2014), pp. 260-264.

[84] Jäckle, S., Liebhaber, M., Gersmann, C. et al. Potential of PEDOT:PSS as a hole selective front contact for silicon heterojunction solar cells. Sci Rep 7, 2170 (2017).

[85] Dimitri Zielke, Claudia Niehaves, Wilfried Lövenich, Andreas Elschner, Matthias Hörteis, Jan Schmidt, Organic-silicon Solar Cells Exceeding 20% Efficiency, Energy Procedia, Volume 77, 2015, Pages 331-339.

[86] P.-J. Alet, S. Palacin, P. Roca I Cabarrocas, B. Kalache, M. Firon and R. de Bettignies, Hybrid solar cells based on thin-film silicon and P3HT - A first step towards nano-structured devices, Eur. Phys. J. Appl. Phys., 36 3 (2006) 231-234

[87] Hyung Hwan Jung, Dong Ho Kim, Chang Su Kim, Tae-Sung Bae, Kwun Bum Chung, and Seung Yoon Ryu, Organic-inorganic hybrid thin film solar cells using conducting polymer and gold nanoparticles, Applied Physics Letters 102:18, (2013).

[88] Ying Peng, Zhiqun He, Adel Diyaf, Aruna Ivaturi, Zhi Zhang, Chunjun Liang, and John I. B. Wilson, Manipulating hybrid structures of polymer/a-Si for thin film solar cells, Applied Physics Letters 104:10, (2014).

[89] Ivan P. Parkin and Robert G. Palgravea, Self-cleaning coatings, J. Mater. Chem., 2005, 15, 1689-1695.

[90] Chern G. C. and Lauks I., (1982), “Spin-coated amorphous chalcogenide films”, J. Appl. Phys., 53, 6979-6982.

[91] Mitzi D. B., (2009), “Solution processing of inorganic materials”, Hoboken, NJ, John Wiley.

[92] Bekir Sami Yilbas, Abdullah Al-Sharafi, Haider Ali, Chapter 3 - Surfaces for Self-Cleaning, Self-Cleaning of Surfaces and Water Droplet Mobility, Elsevier, 2019, Pages 45-98,

[93] A. G. Emslie, F. T. Boner, and L. G. Peck. “Flow of a viscous liquid on a rotating disk”. J. Appl. Phys., 29:858:862. (1958).

[94] M. Dietrich. “Characteristics of resist films produced by spinning”. J. Appl. Phys. 49, 3993. (1978).

[95] C. J. Lawrence. “The mechanics of spin coating of polymer films”. Phys. Fluids 31, 2786. (1988).

[96] F. C. Krebs. “Fabrication and processing of polymer solar cells: A review of printing and coating techniques” Solar Energy Materials and Solar Cells, Volume 93, Issue 4, p 364-412. (2009).

[97] H. Topsøe, Geometric Factors in Four Point Resistivity Measurement, (1966).

[98] F. M. Smits, Measurement of Sheet Resistivities with the Four-Point Probe, Bell Syst. Tech. J., 711 (1958).

[99] E. S. Gadelmawla, M.M. Koura, T.M.A. Maksoud, I.M. Elewa, H.H. Soliman, Roughness parameters, Journal of Materials Processing Technology, Volume 123, Issue 1, 2002, Pages 133-145.

[100] G. Ferguson. An outdoor assesment of organic solar cell performance. Bachelor thesis, Pomona College, Claremont, California, Junio 2013.

[101] H. E. Martinez, “Study of optoelectronic characteristics of photovoltaic devices based on Si and related films deposited by RF glow discharge at low temperature in a multichamber system”, INAOE 2018.

[102] L. Martinu, O. Zabeida, J.E. Klemberg-Sapieha, Chapter 9 - Plasma-Enhanced Chemical Vapor Deposition of Functional Coatings, Editor(s): Peter M. Martin, Handbook of Deposition Technologies for Films and Coatings (Third Edition), William Andrew Publishing, 2010, Pages 392-465.

[103] Yan Ying Ong, Bang Tao Chen, Francis E H Tay and Ciprian Iliescu, “Process Analysis and Optimization on PECVD Amorphous Silicon on Glass Substrate”, (2006), J. Phys.: Conf. Ser. 34 812

[104] Ross, R. C. & Jaklik, J. Plasma polymerization and deposition of amorphous hydrogenated silicon from rf and dc silane plasmas. J. Appl. Phys. 55, 3785 (1984).

[105] Shin-ichiro Ishihara, Masatoshi Kitagawa, and Takashi Hirao, “Anomalous deposition rate dependence of hydrogenated amorphous silicon on substrate temperature”, Journal of Applied Physics 62, 3060 (1987).

[106] Jianmin Qiao, Zhonghua Jiang, Zishang Ding, “Effect of some process parameters on the deposition mechanism of a-Si:H film”, Journal of Non-Crystalline Solids, Volumes 77–78, Part 2, 1985, Pages 829-832.

[107] J. P. Kleider, M. Gauthier, C. Longeaud, D. Roy, O. Saadane, R. Brüggemann, Spectral photoresponses and transport properties of polymorphous silicon thin films, Thin Solid Films. 403–404 (2002) 188–192. doi:10.1016/S0040-6090(01)01659-5.

[108] Söderström, T.; Haug, F.-J.; Terrazzoni-Daudrix, V.; Ballif, C. Optimization of amorphous silicon thin film solar cells for flexible photovoltaics. J. Appl. Phys. 2008, 103, 114509.

[109] Yoon, K.; Shin, C.; Lee, Y.-J.; Kim, Y.; Park, H.; Baek, S.; Yi, J. The role of buffer layer between TCO and p-layer in improving series resistance and carrier recombination of a-Si:H solar cells.Mater. Res. Bull. 2012, 47, 3023–3026.

[110] Lai, J.H. (1979), An investigation of spin coating of electron resists. Polym Eng Sci, 19: 1117-1121.

[111] Francesco Greco, Alessandra Zucca, Silvia Taccola, Arianna Menciassi, Toshinori Fujie, Hiroki Haniuda, Shinji Takeoka, Paolo Darioab and Virgilio Mattoli, “Ultra-thin conductive free-standing PEDOT/PSS nanofilms”, Soft Matter, 2011,7, 10642-10650.

[112] Eunhee Lim (2013) Enhanced Photovoltaic Performance of P3HT:PCBM Cells by Modification of PEDOT:PSS Layer, Molecular Crystals and Liquid Crystals, 585:1, 53-59,

[113] Fan, X., Nie, W., Tsai, H., Wang, N., Huang, H., Cheng, Y., Wen, R., Ma, L., Yan, F., Xia, Y., PEDOT:PSS for Flexible and Stretchable Electronics: Modifications, Strategies, and Applications. Adv. Sci. 2019, 6, 1900813.

[114] Chou, T.-R.; Chen, S.-H.; Chiang, Y.-T.; Lin, Y.-T.; Chao,C.-Y. Highly conductive PEDOT:PSS films by post-treatment with dimethyl sulfoxide for ITO-free liquid crystal display. J.Mater. Chem. C 2015, 3, 3760–3766.

[115] Licheng Tan, Huanyu Zhou, Ting Ji, Liqiang Huang, Yiwang Chen, High conductive PEDOT via post-treatment by halobenzoic for high-efficiency ITO-free and transporting layer-free organic solar cells, Organic Electronics, Volume 33, 2016, Pages 316-323.

[116] Hang Ken Lee, Jai-Kyeong Kim, O. Ok Park, Effects of UV light-irradiated buffer layer on the performance of polymer solar cells, Organic Electronics, Volume 10, Issue 8, 2009, Pages 1641-1644.

[117] Hu, Z.; Zhang, J.; Zhu, Y. Effects of solvent-treated PEDOT:PSS on organic photovoltaic devices. Renew. Energy 2014, 62, 100–105.

[118] Mansurova, S.; Cosme, I.; Kosarev, A.; J. Olivares, A.; Ospina, C.; E. Martinez, H. AZO/PEDOT:PSS Polymer Frontal Interface Deposited on Flexible Substrates for a-Si:H Photovoltaic Applications. Polymers 2018, 10, 1068.

[119] Zhao, Q.; Jamal, R.; Zhang, L.;Wang, M.; Abdiryim, T. The structure and properties of PEDOT synthesized by template-free solution method. Nanoscale Res. Lett. 2014, 9, 557.

[120] Yeon, C.; Kim, G.; Lim, J.W.; Yun, S.J. Highly conductive PEDOT:PSS treated by sodium dodecyl sulfate for stretchable fabric heaters. RSC Adv. 2017, 7, 5888–5897.

[121] Ouyang, J.; Chu, C.-W.; Chen, F.-C.; Xu, Q.; Yang, Y. High-Conductivity Poly(3,4-ethylenedioxythiophene):Poly(styrene sulfonate) Film and Its Application in Polymer Optoelectronic Devices. Adv. Funct. Mater. 2005, 15, 203–208.

[122] Han, Y.-K.; Chang, M.-Y.; Huang, W.-Y.; Pan, H.-Y.; Ho, K.-S.; Hsieh, T.-H.; Pan, S.-Y. Improved Performance of Polymer Solar Cells Featuring One-Dimensional PEDOT Nanorods in a Modified Buffer Layer. J. Electrochem. Soc. 2011, 158, K88.

[123] Kim, S. H.; Kim, J.H.; Choi, H.J.; Park, J. Pickering emulsion polymerizedpoly(3,4-ethylenedioxythiophene):poly(styrenesulfonate)/polystyrene composite particles and their electric stimuli-response. RSC Adv. 2015, 5, 72387–72393.

[124] A. Banerjee, S. Guha, "Study of back reflectors for amorphous silicon alloy solar cell application," J. Appl. Phys. 69, 1030–1035 (1991).

[125] S. Coffa, J.M. Poate, D.C. Jacobson, W. Frank, W. Gustin, Determination of diffusion mechanisms in amorphous silicon, Phys. Rev. B. 45 (1992) 8355–8358.

[126] F. Behrouznejad, S. Shahbazi, N. Taghavinia, Hui-Ping Wu and Eric Wei-Guang Diau, "A study on utilizing different metals as the back contact of CH3NH3PbI3 perovskite solar cells", J. Mater. Chem. A, 2016,4, 13488-13498.

[127] You, Dong Joo, Sun Ho Kim, Hyun Lee, Jin-Won Chung, sun-tae hwang, Youn Ho Heo, Sungeun Lee and Heon-min Lee. "Recent progress of high efficiency Si thin-film solar cells in large area." (2015).

[128] Felipe A. Larrain, Canek Fuentes-Hernandez, Wen-Fang Chou, Victor A. Rodriguez-Toro, Tzu-Yen Huang, Michael F. Toney, and Bernard Kippelen, "Stable solvent for solution-based electrical doping of semiconducting polymer films and its application to organic solar cells", Energy Environ. Sci., 2018,11, 2216-2224

[129] Matthieu Manceau, Agnès Rivaton, Jean-Luc Gardette, Stéphane Guillerez, Noëlla Lemaître, Light-induced degradation of the P3HT-based solar cells active layer, Solar Energy Materials and Solar Cells, Volume 95, Issue 5, 2011, Pages 1315-1325.

[130] Baek, S., Lee, J.C., Lee, Y. et al. Interface modification effect between p-type a-SiC:H and ZnO:Al in p-i-n amorphous silicon solar cells. Nanoscale Res Lett 7, 81 (2012) doi:10.1186/1556-276X-7-81

[131] W. Du, X. Liao, X. Yang, H. Povolny, X. Xiang, X. Deng, K. Sun, Hydrogenated nanocrystalline silicon p-layer in amorphous silicon n–i–p solar cells, Sol. Energy Mater. Sol. Cells. 90 (2006) 1098–1104.

[132] H. Hwan Jung, D. Ho Kim, C. Su Kim, T.-S. Bae, K. Bum Chung, S. Yoon Ryu, Organic-inorganic hybrid thin film solar cells using conducting polymer and gold nanoparticles, Appl. Phys. Lett. 102 (2013) 183902.

[133] S. Y. Ryu, J. hoon Seo, H. Hafeez, M. Song, J.Y. Shin, D.H. Kim, Y.C. Jung, C.-S. Kim, Improved hydrogenated amorphous silicon thin-film solar cells realized by replacing n-type Si layer with PFN interfacial layer, Synth. Met. 228 (2017) 91–98.

[134] X. Jiang, P. Zhang, J. Zhang, J. Wang, G. Li, X. Fang, L. Yang, X. Chen, High Performance of PEDOT:PSS/n-Si Solar Cells Based on Textured Surface with AgNWs Electrodes, Nanoscale Res. Lett. 13 (2018) 53.

[135] Y. Peng, Z. He, A. Diyaf, A. Ivaturi, Z. Zhang, C. Liang, J.I.B. Wilson, Manipulating hybrid structures of polymer/ a -Si for thin film solar cells, Appl. Phys. Lett. 104 (2014) 103903.

[136] J. Fang, B. Yan, T. Li, C. Wei, Q. Huang, X. Chen, G. Wang, G. Hou, Y. Zhao, X. Zhang, Improvement in ultra-thin hydrogenated amorphous silicon solar cells with nanocrystalline silicon oxide, Sol. Energy Mater. Sol. Cells. 176 (2018) 167–173.

[137] Jun-Seok Yeo, Jin-Mun Yun, Dong-Yu Kim, Sungjun Park, Seok-Soon Kim, Myung-Han Yoon, Tae-Wook Kim and Seok-In Na; “Significant Vertical Phase Separation in Solvent-Vapor-Annealed Poly(3,4-ethylenedioxythiophene):Poly(styrene sulfonate) Composite Films Leading to Better Conductivity and Work Function for High-Performance Indium Tin Oxide-Free Optoelectronics” ACS Appl. Mater. Interfaces 2012, 4, 5, 2551-2560.

Future work

This work was focused on the study of hybrid heterojunctions with applications in photovoltaic devices. Due to the results and conclusions obtained, future work is proposed to continue with the research and development of hybrid photovoltaic devices. These topics are mentioned in the following:

Study of hybrid solar cells with n-i-p configuration. The organic material P3HT as a p-type layer in hybrid devices presented a high V_{oc} due to its WF. However, the J_{sc} was too low due mainly to the degraded to the film by the plasma PECVD. Therefore, the development of the fabrication process for n-i-p structures is necessary to use other organic materials, which can contribute to the improvement of hybrid devices according to their properties. On the other hand, the concept of light trapping on hybrid devices through the frontal TCO texturized was not completed due to the organic layer prepare a smooth and planar surface, avoiding that posterior layer keep the texturized form, therefore the n-i-p configuration fabrication may be important for this application.

Application of the PEDOT:PSS/buffer/a-Si:H heterojunction in Heterojunction with Intrinsic Thin layer (HIT) structure. Our hybrid photovoltaic devices showed an excellent charge collection using the PEDOT:PSS/buffer/a-Si:H heterojunction. This heterojunction is suitable to use in HIT structures to efficiently extract the charge generated in c-Si, largely because the a-Si:H passivates the border bonds of c-Si.

Study of secondary doping for PEDOT:PSS films with application in hybrid photovoltaic devices. Although there are many techniques and materials with which the PEDOT:PSS films have been doped looking for better performance in solar cells, all desired properties have not been achieved. Therefore, it is suggested to continue in the research of the doped of PEDOT:PSS films to modify its properties and help improve the performance of hybrid solar cells.

Study of hybrid solar cells with two or more organic thin films. This thesis work contributed with the exploration and development of hybrid solar cells, demonstrating the functionality of these devices. Therefore, it is suggested the exploration of replacement of n-type layer by an organic material, obtaining hybrid devices with two layers of different organic material. Further simplifying the fabrication process of hybrid photovoltaic devices.

Study of the deposition process of the TCO films. “Quality-device” TCO deposited at low temperature, with high transmittance and low sheet resistance is necessary to complete the transference of the technology developed in this work to flexible plastics substrates.

Scientific and technological production

Projects:

Member of **SENER-CONACyT No.152244** project “Celdas Solares Fotovoltaicas Basados En películas Ge(X)Si(1-X): Depositadas Por Plasma Sobre Sustratos De Plástico”

Patents:

MX/a/2016/008619 (In progress)
Kosarev, S. Mansurova, I. Cosme, H.E. Martínez, A. Abramov, A. Kukin, D. Andronikov, E. Tereukov, **A. Olivares**, “Dispositivo fotoeléctrico híbrido de heterounión”.

Book chapters:

A. Kosarev, I. Cosme, S. Mansurova, **A. Olivares**, H. E. Martinez, “Organic Heterojunction Structures for Photovoltaic Applications”, Optoelectronics-Advanced Device structures, InTech, July 2017, DOI: 10.5772/67565.

Journal papers:

I. Cosme, A. Kosarev, S. Svetlana, **A. J. Olivares**, H. E. Martinez, and A. Itzmoyotl, “Hybrid photovoltaic structures based on amorphous silicon and P3HT:PCBM/PEDOT:PSS polymer semiconductors”, Organic Electronics, Elsevier 2016.

Mansurova, S.; Cosme, I.; Kosarev, **A.; J. Olivares**, A.; Ospina, C.; E. Martinez, H. AZO/PEDOT:PSS Polymer Frontal Interface Deposited on Flexible Substrates for a-Si:H Photovoltaic Applications. Polymers 2018, 10, 1068.

Olivares, A.J.; Cosme, I.; Sanchez-Vergara, M.E.; Mansurova, S.; Carrillo, J.C.; Martinez, H.E.; Itzmoyotl, A. Nanostructural Modification of PEDOT:PSS for High Charge Carrier Collection in Hybrid Frontal Interface of Solar Cells. *Polymers* 2019, *11*, 1034.

International proceedings:

A. Olivares, I. Cosme, S. Mansurova, A. Kosarev, H. E. Martinez, "Study of Electrical Conductivity of PEDOT:PSS at Temperatures >300 K for Hybrid Photovoltaic Applications", 12th International Conference on Electrical Engineering, Computing Science and Automatic Control (CCE 2015)", Mexico DF. Oct 2015, pp.547-549. ISBN: 978-1-4673-7838-3. DOI: 10.1109/ICEEE.2015.7357906.

A. Olivares, H.E. Martinez, I. Cosme, S. Mansurova, A. Kosarev, "Effect of Frontal Interface Configuration on Electronic Properties of Organic-Inorganic Hybrid Solar
Cells", 12th International Conference on Electrical Engineering, Computing Science and Automatic Control (CCE 2015)", Mexico DF. Oct 2015, pp. 550-553. ISBN: 978-1-4673-7838-3. DOI: 10.1109/ICEEE.2015.7357949

J. Olivares, I. Cosme, S. Mansurova, A. Kosarev and H. Martínez, "Effect of Hole Transport Organic Layer on Characteristics of Hybrid Photovoltaic Structure," in Frontiers in Optics 2015, OSA Technical Digest (online) (Optical Society of America, 2015), paper JW2A.26.

S. Vazquez, **A. Olivares**, I. Cosme, S. Mansurova, A. Kosarev, A. Itzmoyotl, “Study of optoelectronics properties of indium tin oxide films fabricated by sputtering in oxygen atmosphere”, 13th International Conference on Electrical Engineering, Computing Science and Automatic Control (CCE 2016)", Mexico DF. Sep 2016. DOI: 10.1109/ICEEE.2016.7751218

A. J. Olivares Vargas, S. Mansurova, I. Cosme, A. Kosarev, C. A. Ospina Ocampo, H. E. Martinez Mateo, "Hybrid solar cell based on a-Si/polymer flat heterojunction on flexible substrates", Proc. SPIE 10363, Organic, Hybrid, and Perovskite Photovoltaics XVIII, 103632W (2017); doi:10.1117/12.2274164.

A. J. Olivares Vargas, I. Cosme, S. Mansurova, A. Kosarev, A. Itzmoyotl, "Effect of immerse an organic layer in isopropyl alcohol on characteristics of hybrid photovoltaic structures", Proc. SPIE 10363, Organic, Hybrid, and Perovskite Photovoltaics XVIII, 103633G (2017);doi.org/10.1117/12.2276228

Conference presentations:

S. Mansurova, I. Cosme, C. Ospina, **A. Olivares Vargas**, H. E. Martinez, A. Kosarev, A. Itzmoyotl, “Study of Frontal Interface AZO/PEDOT:PSS on Flexible Substrates for Hybrid Solar Cell Applications”, The 27th International Conference on Amorphous and Nanocrystalline Semiconductors (ICANS27), Seoul, South Korea, August 2017.

I. Cosme, **A. Olivares Vargas**, S. Mansurova, H. E. Martinez, A. Kosarev. A. Itzmoyotl, “Study of solvent treatment on PEDOT:PSS films for organic-inorganic solar cells based on a-Si:H”, The 27th International Conference on Amorphous and Nanocrystalline Semiconductors (ICANS27), Seoul, South Korea, August 2017.

A. Kosarev, I. Cosme, S. Mansurova, H. E. Martinez, A. Abramov, A. Kukin, D. Andronikov, E. Terukov, **A. Olivares Vargas**, The 27th International Conference on Amorphous and Nanocrystalline Semiconductors (ICANS27), Seoul, South Korea, August 2017.

A. Olivares Vargas, I. Cosme, S. Mansurova, J. C. Carrillo and A. Itzmoyotl, The 28th International Conference on Amorphous and Nanocrystalline Semiconductors (ICANS28), Palaiseau, France, August 2019.